NO_2 Limb Retrieval in the Upper Troposphere/ Lower Stratosphere Region

Ralf Bauer

Universität Bremen 2012

NO_2 Limb Retrieval in the Upper Troposphere/ Lower Stratosphere Region

Vom Fachbereich für Physik und Elektrotechnik
der Universität Bremen

zur Erlangung des akademischen Grades eines

Doktor der Naturwissenschaften (Dr. rer. nat.)

genehmigte Dissertation

von

Dipl. Phys. Ralf Bauer

wohnhaft in Bremen

1. Gutachter: John P. Burrows
2. Gutachter: Otto Schrems

Eingereicht am: 13. März 2012
Tag des Promotionskolloquiums: 31. Mai 2012

Abstract

As reactive nitrogen amounts in the stratosphere increase, accurate measurements of these trace gases is of high importance. The SCIAMACHY (SCanning Imaging Absorption spectroMeter for Atmospheric CHartographY) instrument on ENVISAT (European Environmental Satellite) performs measurements in limb geometry since 2002, providing global coverage of NO_2 retrieval results every six days.

In this study, a novel approach to improve the sensitivity of SCIAMACHY NO_2 limb retrieval results at the UTLS (Upper Troposphere/ Lower Stratosphere) altitude layer is described. Additionally, the current NO_2 limb retrieval product is validated in detail and both methods are used for case studies at the North Atlantic region.

In the new approach, two spectral regions (420 nm to 470 nm and 520 to 560 nm) are analyzed instead of one (420 nm to 470 nm) in the current NO_2 limb retrieval product V3.1. This is done, as the atmosphere gradually becomes optically thick for short wavelengths at lower altitudes. However, as the V3.1 product version is considered optimal at the 20 to 40 km altitude range, it is used as a priori profile in the new version with strong constraints at these altitudes.

For this reason, both NO_2 limb retrieval versions need to be validated thoroughly. Airborne instruments on airplanes and balloons provide data for a localized analysis, while a global validation study is performed with three satellite-based solar occultation instruments (SAGE II, HALOE and ACE-FTS). The strong diurnal cycle of NO_2, however, necessitates model-based photochemical corrections to allow the comparison of different instruments at different times and different solar zenith angles.

While lightning events are discussed, the North Atlantic region is studied in more detail. Due to the variability of NO_2, each season is analyzed individually, using averaged NO_2 amounts from up to 7 years. At an altitude of 12 km, an enhanced NO_2 pattern is seen and discussed at the location of the North Atlantic flight corridor.

List of Publications

As first author

Bauer, R., Rozanov, A., McLinden, C. A., Gordley, L. L., Lotz, W., Russell III, J. M., Walker, K. A., Zawodny, J. M., Ladstätter-Weißenmayer, A., Bovensmann, H., and Burrows, J. P., "Validation of SCIAMACHY limb NO_2 profiles using solar occultation measurements", Atmospheric Measurement Techniques Discussions, 4, 4753–4800, DOI: 10.5194/amtd-4-4753-2011

International conference contributions

Ralf Bauer, Alexei Rozanov, Heinrich Bovensmann, Astrid Bracher, Kai-Uwe Eichmann and John P. Burrows, "Sensitivity of NO_2 Limb Retrieval in the Lower Stratosphere and Upper Troposphere Region", 2007 ESA ENVISAT Symposium, Montreux, Switzerland

Ralf Bauer, Alexei Rozanov, Leonard Amekudzi, Peter Hoor, Carl Brenninkmeijer, Heinrich Bovensmann, John P. Burrows, "Improving sensitivity of NO_2 limb retrieval in the lower stratosphere and upper troposphere region", 37th COSPAR Scientific Assembly Montreal, Canada, 13-20 July 2008

Ralf Bauer, Alexei Rozanov, Heinrich Bovensmann, Peter Hoor, Patrick Jöckel, Carl Brenninkmeijer and John P. Burrows, "NO_2 in the lower stratosphere and upper troposphere region retrieved from SCIAMACHY limb measurements", 38th COSPAR Scientific Assembly Bremen, Germany, 18-25 July 2010

Contents

1

Introduction

The Earth atmosphere makes this planet unique in the solar system, as it provides an environment in which mankind can live and survive. Its constituents are very important for nature and an investigation even of the lesser abundant trace gases is important.

Nitrogen dioxide (NO_2), a very reactive trace gas in the atmosphere, is mostly known for its influence on ozone concentrations. It is usually discussed together with nitrogen monoxide (NO) as the family NO_x with $NO_x = NO + NO_2$, while NO_y is the sum of all reactive nitrogen oxides, which includes species such as NO, NO_2, NO_3, N_2O_3, N_2O_5, and HNO_3. The family NO_x is linked by several reactions and converted into each other during the day depending on sunlight. It is the major source of ozone depletion in the stratosphere (Crutzen, 1970), but ironically the same gases lead to ozone formation in the troposphere if specific conditions are present (Crutzen, 1979). Tropospheric ozone is rather problematic than useful, as it is a toxic gas.

Depletion of ozone is a problem at higher altitudes. However, the ozone (O_3) hole over the Antarctic region is largely caused by chlorofluorocarbons (CFCs). CFCs in the atmosphere are of anthropogenic origin, and were widely used as refrigerants, propellants (in aerosol applications) and solvents.

The ozone layer is important as it shields us from UV-B radiation, which can lead to skin cancer and other related illnesses. Wildlife is also affected by this. With the Montreal protocol, CFCs were banned from industrial production, which highlights the importance of an investigation of the atmosphere. Without measurements and careful analyses of the atmosphere such problems would not be discovered. As mentioned before, the influence of NO_x on the ozone concentrations is quite significant, it is responsible for 70% of the ozone loss in the stratosphere (Portmann *et al.*, 1999).

Most stratospheric NO_x originates from N_2O, as the N_2O lifetime (about 125 years) is long enough to be transported to high altitude levels in significant amounts. As it is stated in Fahey & Hegglin (2011), while the ozone depleting substances (ODS) controlled by the Montreal Protocol still dominate ozone depletion, current N_2O emissions result in more ozone depletion than the current emissions of any ODS. With the ban of ODS, N_2O emissions (of which two thirds are anthropogenic) have become the most important emissions of an ozone depleting compound. Contrary to the ODS, the N_2O amount in the atmosphere is increasing with 0.8 ppb per year, and has reached a level of 320 ppb compared with 270 ppb from preindustrial times, see WMO (World Meteorological Organization) (2011). Although this leads to increased stratospheric NO_x levels, the reduction of ODSs as a result of the Montreal protocol dominates the change of ozone levels. N_2O is also an important greenhouse gas. For CO_2, one of the most important greenhouse gas, emissions from anthropogenic activities between 1750 and 2050 have resulted in an additional radiative forcing of 8 W per m^2. In the same timeframe, anthropogenic emissions of N_2O have led to additional radiative forcing of about 1 W per m^2, which cannot be ignored, see Fahey & Hegglin (2011).

However, N_2O is not the only source of NO_x. Since the atmosphere consists mainly of nitrogen (N_2) and oxygen (O_2), the formation of NO_x takes place naturally. High temperatures are all that is needed and therefore combustion engines as well as lightning can easily produce NO_x. With the introduction of three-way-catalytic converters for internal combustion engines this production is somewhat lowered. However, NO_x is still found in vast amounts over regions with high industrial activity (Richter *et al.*, 2005). According to Reis *et al.* (2009), a steady decrease of NO_x emissions over Europe and the USA in the timeframe from 1990 to 2005 is offset by an increase of emissions from China.

It is therefore of high importance to know the NO_2 amounts in the atmosphere as precisely as possible. Balloon measurements are available, but these can only produce a limited number of profiles (Butz *et al.*, 2006). Satellite instruments, such as SCIAMACHY (SCanning Imaging Absorption spectroMeter for Atmospheric CHartographY) (see section 2.2, and Bovensmann *et al.*, 1999; Burrows *et al.*, 1995) on the European environmental satellite ENVISAT, provide a high number of measurements over several years. In contrast to solar occultation instruments (e.g. SAGE II, ACE-FTS, HALOE), SCIAMACHY can be operated in limb mode, which uses solar straylight and combines a high vertical resolution of 3.3 km with a very good global coverage. Other satellite instruments, that can retrieve NO_2 concentrations in limb mode are OSIRIS on Odin and MIPAS on Envisat.

A retrieval method which generates NO_2 data sets from the largest possible altitude region in a reliable way is the key in making usage of SCIAMACHY's large data set to analyze and monitor the NO_2 concentrations in the atmosphere.

While the stratosphere and the troposphere are well explored regarding NO_2, the altitude region at the border of these two atmospheric layers at around 10 to 15 km is more difficult to investigate. This area around the tropopause is known as the Upper Troposphere/Lower Stratosphere region (UTLS). In this work, both an accurate investigation of the performance of the current SCIAMACHY NO_2 limb retrieval processor (Version 3.1) mainly in the 20 to 40 km range is performed, and in addition, improvements in the retrieval for an enhanced sensitivity in the UTLS range are implemented and investigated.

In order to validate NO_2 retrieval results and to perform meaningful comparisons, the strong diurnal variation of this species must be considered. Therefore, a model to calculate the NO_2 change between two collocated measurements is used and its performance is investigated. The influence of several error sources on retrieved NO_2 profiles is discussed, applying a synthetic retrieval to several error scenarios, including clouds, pointing errors and aerosols. This includes the simulation of clouds outside the field of view, which in a real measurement cannot be avoided by applying simple cloud-masking methods.

Although the approach discussed here is not the first attempt to investigate the NO_2 amounts in the UTLS altitude region (Sioris *et al.*, 2007), this study shows several new key features in this research field. To improve the NO_2 retrieval process for the UTLS altitude region, among other changes the inclusion of a second spectral region at 520 to 560 nm besides the original window from 420 to 470 nm is implemented. This novel approach deals with the wavelength-dependent atmospheric scattering, which is the most important problem for the NO_2 retrieval at the UTLS altitude region.

Using the thoroughly investigated data sets, case studies are performed. The main focus region of these is the North Atlantic, and an enhanced NO_2 amount is seen in the UTLS altitude region. Both the current retrieval processor and the version adapted for the UTLS region are applied. The influence of cloud masking, which is included in the V3.1 SCIAMACHY NO_2 limb retrieval results, is also investigated.

This work is divided into five chapters. Following this introduction (Chapter 1), the chemistry of NO_2, as well as currently used methods for NO_2 retrieval, is described in Chapter 2. The methods and data sources needed for this work are explained there, as well. In Chapter 3, sensitivity studies are described to estimate the influence of several error sources on the NO_2 retrieval results, as well as to evaluate improvements for the NO_2 retrieval. A modification for the NO_2 retrieval process is introduced, which improves the sensitivity for the UTLS altitude region. A program to compute different NO_2 concentrations caused by the diurnal variation of NO_2 is presented. In Chapter 4, the validation of NO_2 retrieval results is performed using the data sources described in Chapter 2. Different case studies of enhanced NO_2 concentrations in the UTLS region are studied, including overviews of the NO_2 amounts for the whole North Atlantic region. Finally, Chapter 5 summarizes the main results of this work.

2

Background

2.1 Chemistry of NO_2

Nitrogen dioxide (NO_2) is a highly reactive trace gas in the atmosphere. Although its main constituents nitrogen and oxygen are the most common gases in the air, anthropogenic sources play an important role for the abundance of NO_2. In this section, the reactions of NO_2 and NO are investigated in detail. Since NO_2 and NO are linked through several reactions, in which both species form a reservoir for each other, it is common to discuss NO_x, which is $NO_2 + NO$. NO_x plays a very important role in the depletion of ozone in the stratosphere, but can also lead to increased amounts of ozone at lower altitudes. Additionally, with NO_y the sum of all reactive nitrogen oxides is described, which includes the species NO, NO_2, N_2O, NO_3, N_2O_3, N_2O_5, and HNO_3.

In the stratosphere, NO_x is responsible for up to 70% of the ozone loss, see Crutzen (1970); Portmann *et al.* (1999) The NO_x reactions dominating the catalytic ozone destruction between about 25 and 40 km are:

$$\mathrm{NO} + O_3 \rightarrow \mathrm{NO_2} + \mathrm{O_2} \tag{2.1}$$

$$\mathrm{NO_2} + h\nu \rightarrow \mathrm{NO} + \mathrm{O} \tag{2.2}$$

$$\mathrm{NO_2} + O \rightarrow \mathrm{NO} + \mathrm{O_2} \tag{2.3}$$

It can be concluded, that knowledge about NO_x and also NO_2 alone is important because of its large effect on the ozone concentration. Also, NO_x is responsible for the *formation* of ozone in the tropospheric altitude regions. The reason for this is the presence of peroxy radicals (HO_2 and its homologues RO_2) in the troposphere, which take part in the following reaction:

$$RO_2 + NO \rightarrow RO + NO_2 \tag{2.4}$$

Thus, at a certain altitude (the turnover point) NO_x switches its role from ozone depletion to ozone formation. To understand this, the process will be described step by step. In the troposphere, ground state (^{3}P) oxygen atoms react with oxygen molecules:

$$O(^3P) + O_2 + M \rightarrow O_3 \tag{2.5}$$

M in this equation is a highly energetic third body needed for the reaction. So each photolysed NO_2 molecule (see reaction 2.2) can lead to the formation of an ozone molecule, at least in the troposphere. On the other hand reaction 2.1 depletes ozone by oxidization of NO to NO_2. The reactions 2.1, 2.2 and 2.5 provide a 'photo-stationary' state between NO and NO_2 with the ratio [NO]/ [NO_2], called the *Leighton ratio*. In a stationary state the rate of NO_2 production $P(NO_2)$ and NO_2 destruction $D(NO_2)$ must be equal:

$$P(NO_2) = \frac{d}{dt}[NO_2] = k_3 \cdot [O_3] \cdot [NO] \tag{2.6}$$

$$D(NO_2) = -\frac{d}{dt}[NO_2] = -j_1 \cdot [NO_2] \tag{2.7}$$

In these equations, k_3 and j_1 are the reaction rate constants. This leads to:

$$P(NO_2) = k_3 \cdot [O_3] \cdot [NO] = -D(NO_2) = j_1 \cdot [NO_2] \tag{2.8}$$

and finally:

$$L_0 = \frac{[NO]}{[NO_2]} = \frac{j_1}{k_3 \cdot [O_3]} \tag{2.9}$$

During daytime, NO and NO_2 are rapidly converted into each other and it is thus straightforward to discuss the sum of these two species as NO_x. In this work, only NO_2 will be investigated, since there are no spectral features of NO in the spectral range of SCIAMACHY.

Another important point is that reaction 2.2 depends on the presence of photons, i.e. during the day the ratio between NO and NO_2 changes. As discussed by Brohede *et al.* (2007b), in the absence of sun light at nighttime, the remaining NO is converted to NO_2, until NO is practically depleted. Additional chemistry during the night leads to a slow decrease in NO_2, converting NO_2 to several reservoir species:

$$NO_2 + O_3 \rightarrow NO_3 + O_2 \tag{2.10}$$

$$NO_2 + NO_3 + M \leftrightarrow N_2O_5 + M \tag{2.11}$$

$$NO_2 + OH + M \rightarrow HNO_3 + M \tag{2.12}$$

At daytime, NO_x is regenerated from these species via photolysis.

$$NO_3 + h\nu \rightarrow NO + O_2 \rightarrow NO_2 + O \tag{2.13}$$

$$N_2O_5 + h\nu \rightarrow NO_3 + NO_2 \tag{2.14}$$

$$HNO_3 + h\nu \rightarrow HO + NO_2 \tag{2.15}$$

While the conversion of NO_3 after sunrise is fast and the NO_3 is rapidly depleted, the conversion of N_2O_5 is slower.

The third reservoir species is nitric acid (HNO_3). In the lower stratosphere, when polar stratospheric cloud (PSC) particles are formed with HNO_3, depletion of NO_y (called denitrification) occurs, when these particles are deposited. This also includes the depletion of NO_x.

It is important to discuss the variation of NO_2 in the stratosphere, which not only changes during the day, but also shows a seasonal cycle. For example, stratospheric NO_2 levels in the Northern Hemisphere in winter are lower than in summer, as already seen by Noxon (1975). Furthermore, the NO_2 columns increase with increasing latitude in Northern Hemisphere summer (i.e. June, July, August), while they decrease with increasing latitude during Northern Hemisphere winter (December, January, February). Additionally, in Noxon (1979) it was found that during winter this decrease is especially steep at latitudes around 40° to 45°, which is known as the Noxon-cliff.

In order to demonstrate such a (Northern Hemisphere) winter gradient, Figure 2.1 shows the integrated NO_2 values from limb measurements from 20 to 40 km in 1 km steps for a longitude range from 120° W to 80° W and December 2005. As discussed before, stratospheric NO_2 values decrease from South to North. A steep edge close to 40° N is seen, which can be identified as the Noxon-cliff, although its location is shifted south when compared to the results in Noxon (1979). Additionally, a plot showing the

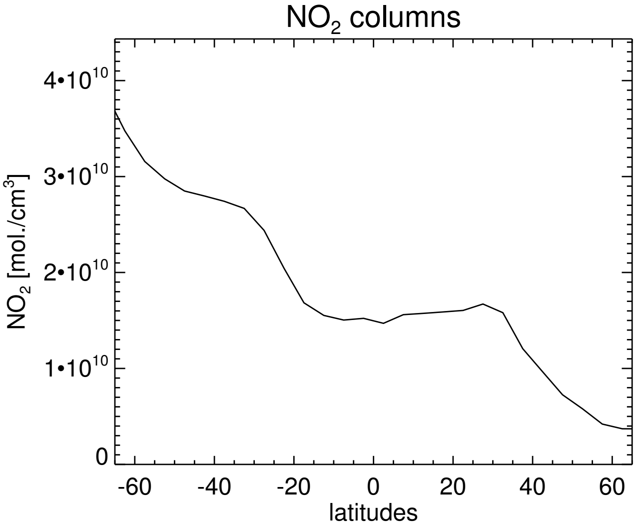

Figure 2.1: For a longitudinal range from 120° W to 80° W, all SCIAMACHY NO$_2$ limb profiles are averaged into 5° latitude bins for December 2005 and summarized over the altitudes between 20 and 40 km. Cloud-contaminated profiles are not included.

averaged NO$_2$ profiles before summation is seen in Figure 2.2. It becomes clear, that most NO$_2$ is accumulated in the stratosphere, mostly close to 30 km.

The combined NO$_x$ is long-lived in the lower stratosphere and accumulates in northern latitudes due to poleward transport of air from equatorial regions. This explains the summer gradient of stratospheric NO$_x$ (and hence, NO$_2$). In winter, the situation is reversed, and two reasons can be identified for that. First of all, nights are longer and days shorter, so there is more time for Reaction 2.11 and less time for Reaction 2.14 on each day. Secondly, the temperature dependence of Reaction 2.14 also slows down the formation of NO$_2$. Thus, in winter times at northern latitudes NO$_x$ is basically trapped in the reservoir species. If this air is transported southwards, with higher temperatures and shorter N$_2$O$_5$ lifetimes, the accumulated N$_2$O$_5$ is converted to NO$_x$, which leads to the formation of the Noxon-cliff as mentioned before.

It is worth to note, that the Noxon-cliff was discovered in the 70s, years before the ozone hole. As Solomon (1999) states, the chemistry of the Noxon-cliff was not understood at that time, and its existence and the lack of stratospheric NO$_2$ at southern high latitudes during southern winter are linked to the ozone hole, which was not discovered until almost 10 years later (Farman *et al.*, 1985). Solomon (1999) concludes,

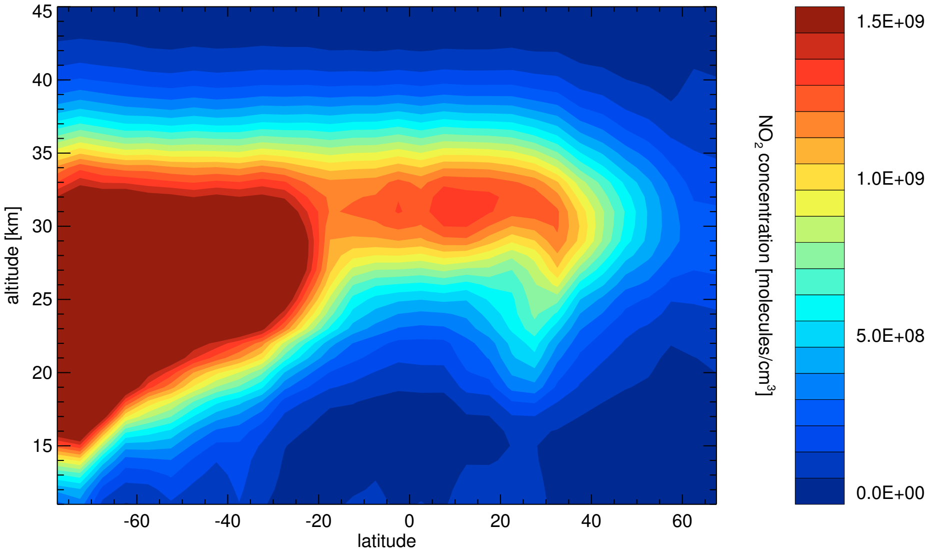

Figure 2.2: The averaged NO_2 profiles from Figure 2.1 before summation

had the chemistry of stratospheric NO_x been understood earlier, the existence of the ozone hole could have been predicted before measurements revealed it.

Although the presence of NO_2 in the stratosphere leads to the destruction of ozone, the catalytic reactions involving Cl and ClO (key species in the ozone hole formation) are far more effective for O_3 depletion and with a reaction involving NO_2, ClO is converted to a reservoir species:

$$\mathrm{ClO} + \mathrm{NO_2} + M \rightarrow \mathrm{ClONO_2} + \mathrm{M} \tag{2.16}$$

The ozone hole is more pronounced above the Southern Hemisphere, but dangerously low ozone concentrations are also observed above the Northern Hemisphere, depending on the conditions.

For the investigation of NO_2, the diurnal variation outlined in this chapter causes an additional challenge, as measurements need to be validated and two measurements are usually not performed at the same time and geolocation. This proves to be a problem for validation, see sections 3.2 and 4.1. Based on a two dimensional chemical transport model, an example of the diurnal variation is given in Fig. 2.3 for an altitude of 30 km. The NO_2 concentration (black) is very sensitive to the local time. The solar

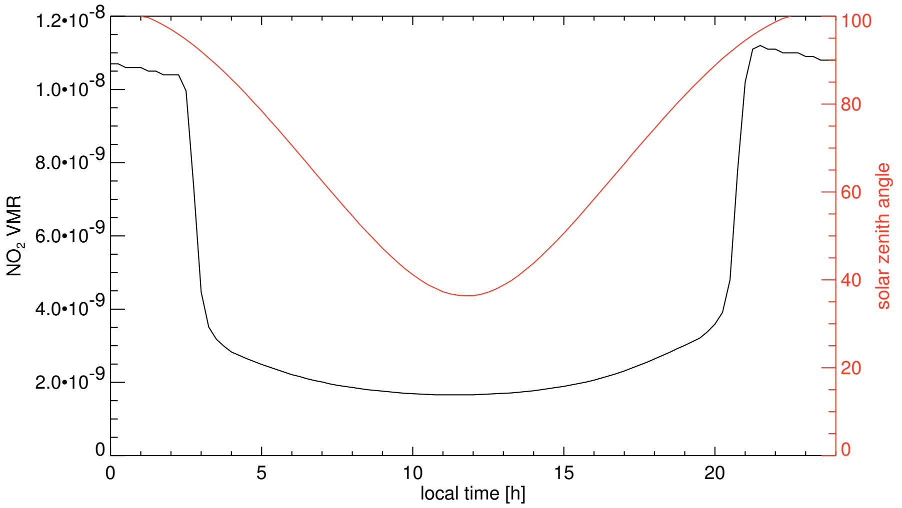

Figure 2.3: This figure shows the change of NO_2 over the course of one day, simulated for an altitude of 30 km, 66° N in May.

zenith angle (SZA) is shown as a red curve in the same graph. The SZA is the angle between the local zenith and the line of sight to the sun. Depending on the position of the observer, at a value of about 90° the changeover between night and day occurs, which is the reason for the significant variation in NO_2 values. Figure 2.4 shows the same scenario for an altitude of 16 km. NO_2 values change noticeably, but the relative change is lower than in the 30 km example. The difference in the NO_2 behaviour is most likely related to a different temperature and a different concentration of reservoir species (N_2O_5, HNO_3) at the two example altitudes. Depending on the conditions, the shape of this diurnal cycle can look quite different, as seen in (Brohede *et al.*, 2007b, ,page 1256), where the NO_2 variation at 15 km is the most symmetrical.

As already mentioned, at lower altitudes reaction 2.4 will lead to the formation of ozone, since NO is oxidised to NO_2 instead of favouring reaction 2.1, which depletes ozone. This is the reason, why the NO and indirectly NO_2 produced by the current subsonic aircraft fleet by combustion increases the ozone concentration. In cruising altitudes this increase is estimated to be around 6% compared to an atmosphere without aircraft emissions (Houghton *et al.*, 2001).

If airplanes flew higher, ozone depletion would be dominating. This would be the case for a potential airplane fleet with a larger percentage of supersonic airplanes, as

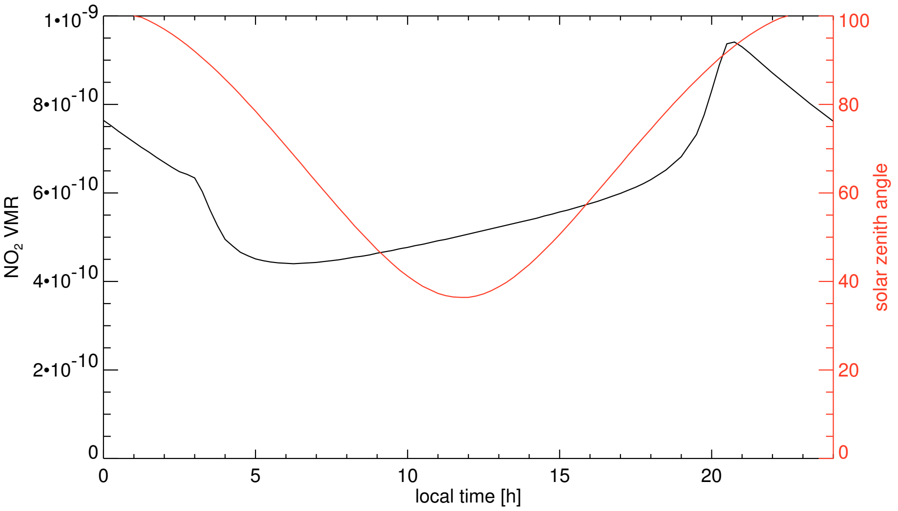

Figure 2.4: Using the same scenario as for Fig. 2.3, the diurnal variation of NO_2 is plotted for an altitude of 16 km.

in that case higher flight altitudes are more economic, see Søvde *et al.* (2007).

Acid rain and smog are also related to nitric oxides (NO_x), but since this work concentrates on the upper troposphere/ lower stratosphere (UTLS) altitude region, these two effects are not discussed here in detail.

The role of NO_x as a greenhouse gas

For the discussion of greenhouse gases, the concept of radiative forcing is important. Its definition is given in Myhre *et al.* (1998) as: 'The radiative forcing of the surface-troposphere system due to the perturbation in or the introduction of an agent (say, a change in greenhouse gas concentrations) is the change in net (down minus up) irradiance (solar plus long-wave; in Wm^{-2}) at the tropopause after allowing for stratospheric temperatures to readjust to radiative equilibrium, but with surface and tropospheric temperatures and state held fixed at the unperturbed values.'

If one wants to investigate the role of NO_x as a greenhouse gas, the indirect radiative forcing is more important than the direct radiative forcing by NO_x itself, since the concentrations of ozone and methane are changed by the presence of NO_x. Figure 2.5 shows how a change in ozone affects the surface temperature, depending on the altitude. At tropopause altitudes, an enhanced ozone concentration would lead to the

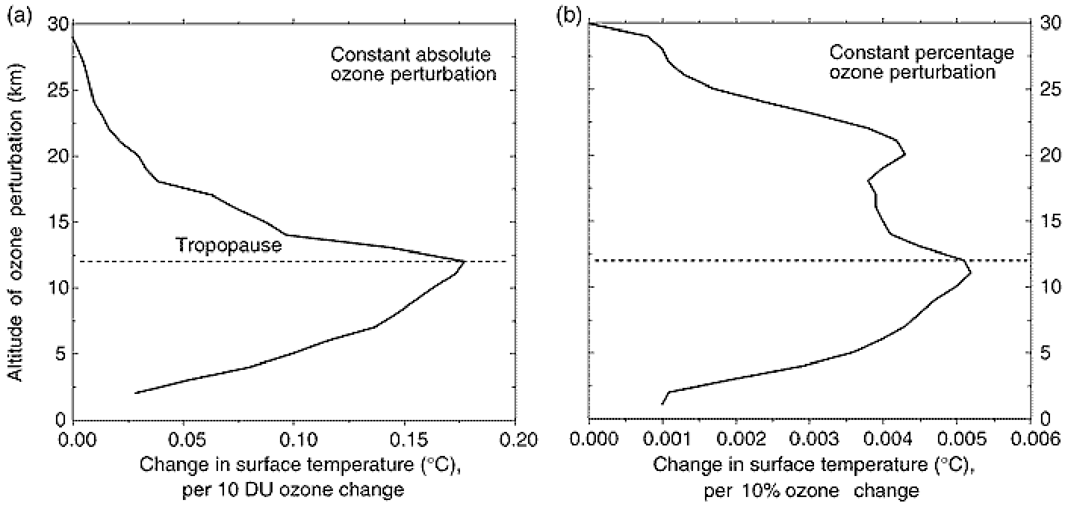

Figure 2.5: This figure shows how a change in ozone concentration will affect the surface temperature. The ozone perturbations are shown in absolute (panel a) and relative (panel b) values. Source: Houghton *et al.* (2001)

strongest increase in surface temperature. For aircraft emissions, the radiative forcing has been investigated by Penner (1999), and the results are shown in Fig. 2.6. For the reasons given before, the radiative forcing of NO_x in this figure is given as indirect radiative forcing.

Sources of NO_2 in the atmosphere

The main sources of NO_2 in the UTLS region are lightning events, biomass burning and anthropogenic sources mostly in the form of internal combustion engines, see Manahan (1991). Very high temperatures lead to the following reaction:

$$N_2 + O_2 \rightarrow 2NO \tag{2.17}$$

The reactants in this equation are the major components of the air and thus always present. Dry air within several kilometres from ground level consists mostly of nitrogen (78.08% by volume) and oxygen (20.95%). The NO produced in Reaction 2.17 is partly converted to NO_2, resulting in a photo-stable-equilibrium of both species, see page 6.

With respect to the UTLS altitude region, aircraft emissions are considered as the most important anthropogenic NO_x source. Although more NO_x is produced by ships

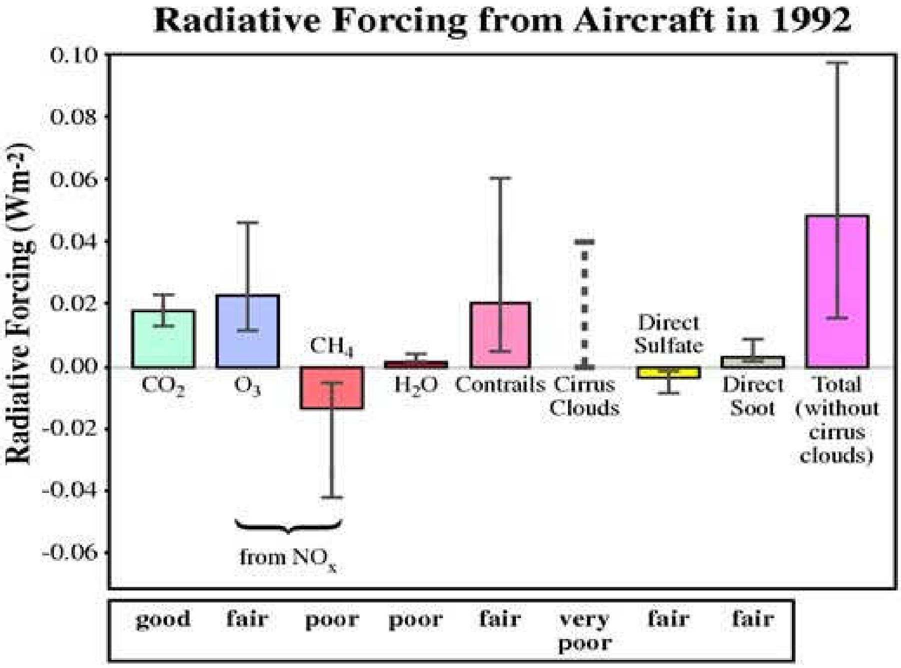

Figure 2.6: The radiative forcing from aircraft emissions is shown here. Note that NO_x emissions contribute indirectly to radiative forcing, as those emissions change the concentrations of ozone (O_3) and methane (CH_4). Source: Penner (1999)

and car engines, those emissions usually don't reach the UTLS region, but are for example washed out as acid rain. This is not always true, since there are weather phenomena, where anthropogenic ground NO_x emissions may reach the UTLS. One such event is the so-called 'meteorological bomb' (Stohl *et al.*, 2003)), in which significant amounts of emissions from the North American East coast reach the stratosphere (which is otherwise unlikely) and are transported rapidly to Europe. The enhanced NO_x mixing ratios over Europe due to this phenomenon are expected to be around 2–3 pptv in winter.

Another possibility for NO_x to reach the lower stratosphere are biomass burning events. An example for this is described by Fromm *et al.* (2005), when in 1998 smoke from such an event reached the stratosphere, presumably along with NO_x. There are also newer events of this kind in the measurement time of SCIAMACHY, which was not yet active in 1998. Similarly, strong volcanic eruptions are capable of injecting smoke and NO_x into the stratosphere.

There is another source of NO_x (however with direct production) close to or in the UTLS region, which are the lightning events. During this natural phenomenon, NO_x is produced locally in significant amounts (Sioris *et al.*, 2007).

For the sensitivity studies in section 3.3.1 estimates for the NO_x sources are needed to determine the ability of the retrieval to detect the enhanced NO_2 generated by these sources. In Gauss *et al.* (2006), model calculations are performed estimating the impact of emissions from subsonic aviation on the chemical composition of the atmosphere. Figure 2.7 shows, that airplane emissions in the North Atlantic flight corridor are high compared to other flight corridors, because a huge amount of traffic (between North America and Europe) is concentrated there. For this reason, the focus in section 4.3 is on the North Atlantic region. Also quantitative estimates on aircraft emissions are gathered from these model calculations, which provide the necessary information (estimated NO_2 perturbation) for sensitivity studies in section 3.3.1.

In most NO_2 vertical profiles the maximum of NO_2 is at about 20 to 30 km as seen for example in Fig. 2.2, i.e. in stratopsheric regions. The major source of stratospheric NO_2 is the reaction of photochemically-produced excited oxygen atoms with nitrous oxide (N_2O), also known as laughing gas, see Manahan (1991).

$$N_2O + O \rightarrow 2NO \tag{2.18}$$

N_2O is the major source of stratospheric NO_2, as the atmospheric lifetime of tropospheric NO_2 is too short to reach the stratosphere at significant levels under normal conditions. As discussed in Montzka *et al.* (2011), N_2O is not only an important greenhouse gas, it is also the most important ozone depleting gas, that is not covered by the Montreal Protocol, see Ravishankara *et al.* (2009). However, reduction of N_2O is part of the Kyoto protocol, and anthropogenic sources of N_2O are mostly of agricultural origin. It should be noted, that the additional N_2O emissions from bio-fuel production most likely negate the desired advantages with respect to emissions from fossile fuel burning, see Crutzen *et al.* (2007).

At even higher altitudes (upper stratosphere and mesosphere), ions and ionizing radiation are important as a source of NO (and hence, NO_2). As this altitude region is not investigated in this work, this is only mentioned for completeness.

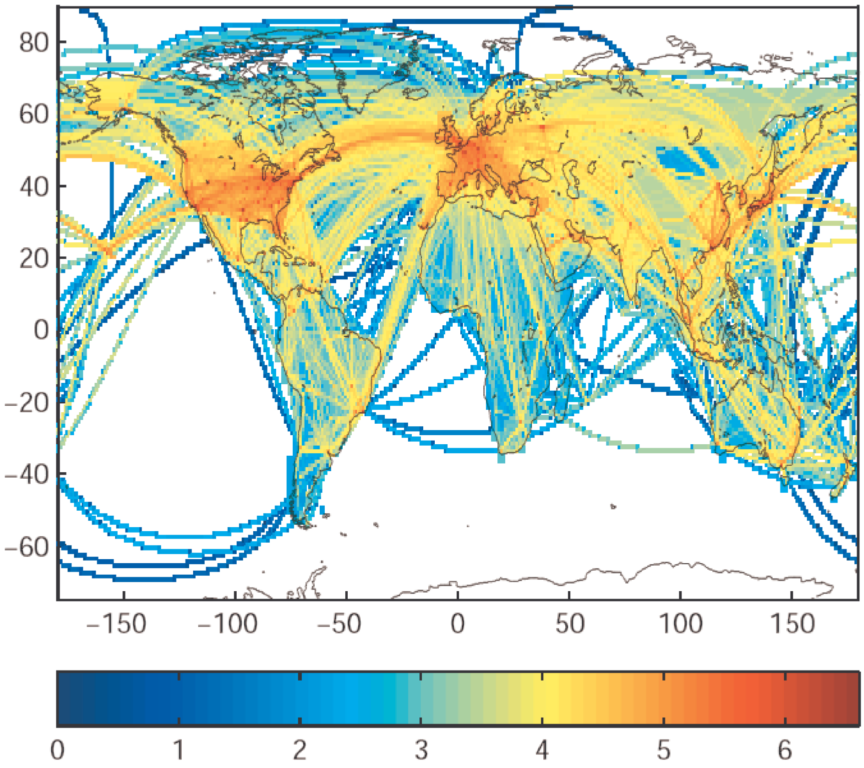

Figure 2.7: Geographical distribution of aviation fuel burned in the TRADEOFF reference case (year 2000), vertically integrated for each 1° × 1° column. Unit: $\log_{10}$ [kg(fuel)/(day $\times 1^\circ \times 1^\circ$ column)]. TRADEOFF was an EU-project, and a 3D-chemical transport model was applied to generate this figure. From Gauss *et al.* (2006).

2.2 The SCIAMACHY instrument on ENVISAT

Launched in March 2002, the Earth-observing satellite ENVISAT provides a platform for several instruments including the spectrometer SCIAMACHY (Bovensmann *et al.*, 1999; Burrows *et al.*, 1995). ENVISAT orbits the Earth in about 101 minutes in a Sun synchronous near-polar orbit, repeating its cycle in 35 days. The satellite has been planned as a five year mission, but exceeded its lifetime and is still operational at present (Oct. 2011).

As the retrieval of SCIAMACHY results is the main focus of this work, a more detailed description is given for this particular instrument. SCIAMACHY is the acronym for 'SCanning Imaging Absorption spectroMeter for Atmospheric CHartographY' and is also a Greek expression (σκιάμαχιά), which means chasing or hunting shadows

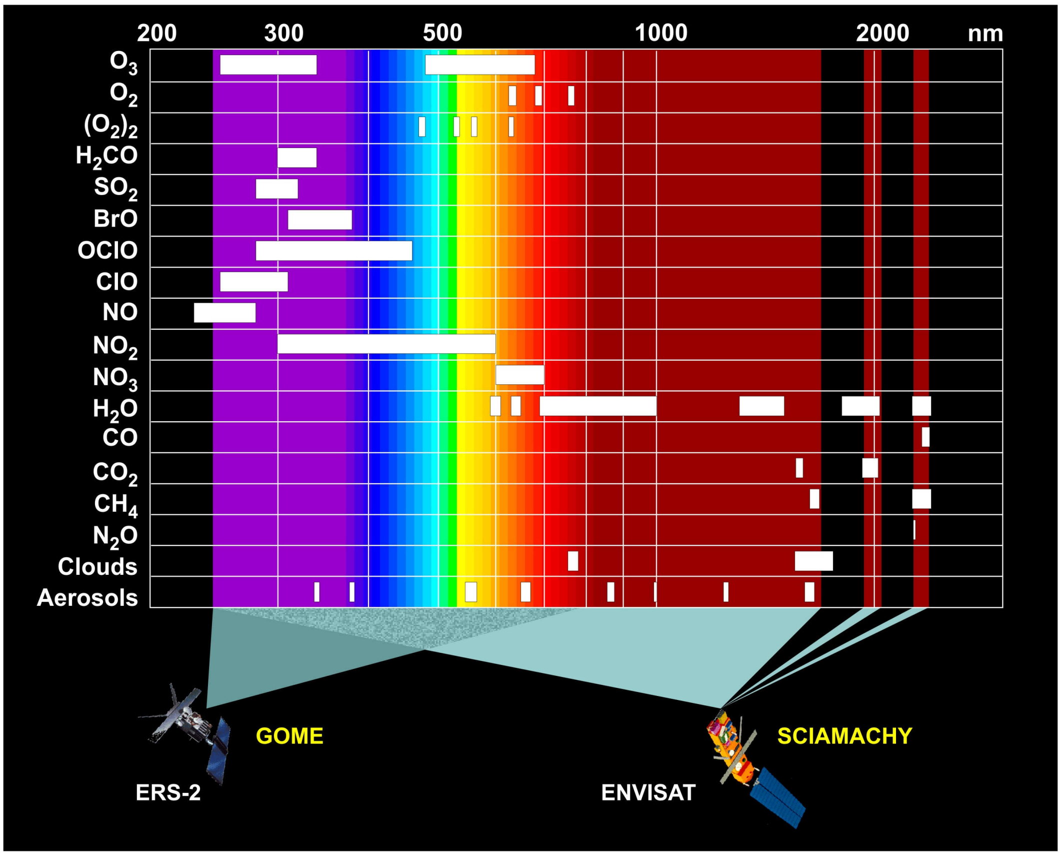

Figure 2.8: Due to high resolution and a wide wavelength range many different trace gases can be detected with SCIAMACHY. The spectral range of its predecessor GOME is displayed for comparison. Figure provided by Stefan Noël.

(Gottwald *et al.* (2006)). It is a spectrometer aimed at the detection of a wide range of atmospheric trace gases, as shown in Fig. 2.8.

In six overlapping channels SCIAMACHY covers the spectral range from 214 nm to 1773 nm, see Table 2.1. There are two additional non overlapping channels in the short-wavelength infrared region covering 1934 to 2044 nm and 2259 to 2386 nm.

SCIAMACHY is operated in three different viewing geometries, in nadir, limb and occultation which are shown in Fig. 2.9. The instrument is operating in one of these modes at a time. During one orbit, it alternately switches between nadir and limb geometry.

- *Nadir:* If operated in nadir, SCIAMACHY measures stray light directly from below the instrument in a 960 km wide swath (orthogonal to the flight direction

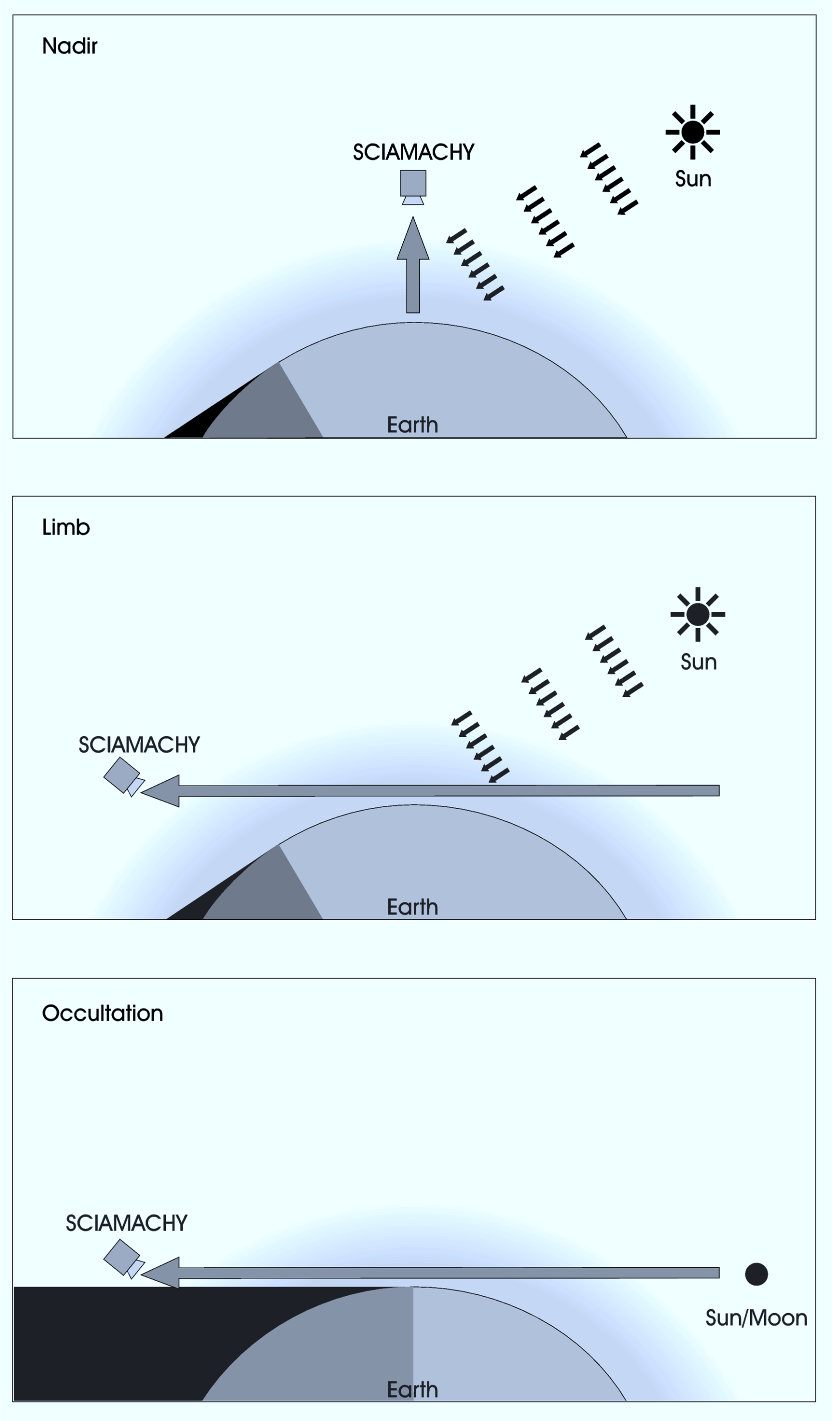

Figure 2.9: This figure shows the three different viewing geometries, that are possible with SCIAMACHY: nadir, limb and occultation. Figure provided by Stefan Noël.

Channel	Spectral range (nm)	Resolution (nm)	Stability (nm)	Temperature Range (K)
1	214 - 334	0.24	0.003	204.5 - 210.5
2	300 - 412	0.26	0.003	204.0 - 210.0
3	383 - 628	0.44	0.004	221.8 - 227.8
4	595 - 812	0.48	0.005	222.9 - 224.3
5	773 - 1063	0.54	0.005	221.4 - 222.4
6	971 - 1773	1.48	0.015	197.0 - 203.8
7	1934 - 2044	0.22	0.003	145.9 - 155.9
8	2259 - 2386	0.26	0.003	143.5 - 150.0

Table 2.1: Properties of all available SCIAMACHY science channels. For SCIATRAN NO_2 retrieval only the channels 3 and 4 are used. Table source: Gottwald *et al.* (2006)

of ENVISAT). The horizontal resolution is 30 km in flight direction and 60 km orthogonal to flight direction. (Fig. 2.9, upper plot)

- *Occultation:* In this mode the SCIAMACHY instrument points at the sun or the moon directly through the atmosphere. With a horizontal resolution of 30 km and a vertical resolution of about 2.5 km this viewing mode provides the highest spatial resolution. However, occultation measurements are only possible at sun/moon rises (seen from the instrument), so the spatial coverage is lower compared to limb mode. (Fig. 2.9, lower panel)

- *Limb:* In this viewing geometry, the instrument is pointed tangential to the Earth, but the sun as the light source is not positioned in viewing direction, i.e., stray light is used for detection of trace gases. A mirror system projects the spectrometer slit parallel to the horizon. The limb mirror scans the atmosphere in horizontal (azimuth) direction over 1.5 seconds. After each scan, the elevation mirror makes a step of 3 km in tangent height. A typical limb measurement consists of 34 horizontal scans, which start approximately pointed 3 km below the horizon. Each scan covers a 960 km wide range in horizontal direction. Determined by integration time, these scans have a resolution of 240 km. The vertical resolution is about 3 km. Resolution and coverage refer to the tangent point. (Fig. 2.9, middle panel)

For this thesis the limb viewing geometry is used, as it combines a relatively good vertical resolution (about 3 km) with a good spatial coverage. This is advantageous if the vertical structure of atmospheric NO_2 amounts is studied, which is more difficult to investigate in nadir geometry. Nadir measurements are well suited for the detection of tropospheric vertical columns of NO_2 and have been used with great success to show the increasing NO_2 over China, see Richter *et al.* (2005). Tropospheric NO_2 proves to be more difficult to detect in limb mode due to physical reasons (see Fig. 3.12 and section 3.3).

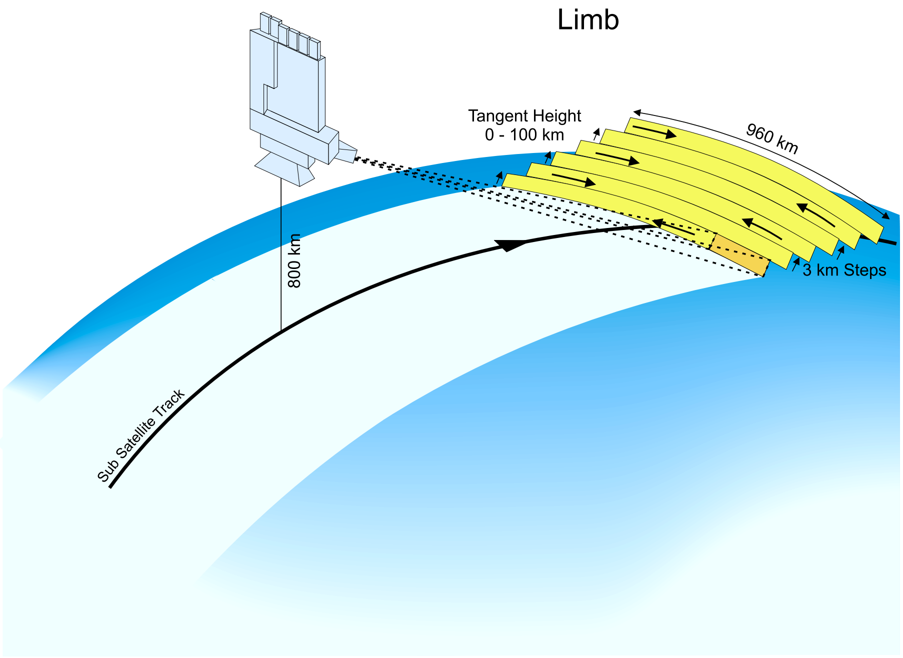

Figure 2.10: The limb viewing geometry used in this work is illustrated in more detail here. The sketch shows the 960 km wide field of view at the tangent point. The 3 km wide scans do not overlap. Figure provided by Stefan Noël.

2.3 Cloud detection: SCODA

Results from SCODA (SCIAMACHY Cloud Detection Algorithm) are already included in the current Bremen NO_2 product version. This cloud retrieval is performed using the same the same instrument in the same viewing geometry as the NO_2 retrieval. This cancels out a number of possible uncertainties, as the measurements used for cloud and NO_2 retrieval are perfectly matched geometrically. Therefore, SCODA is expected to be the best available cloud detection product for cloud masking of SCIAMACHY NO_2 limb retrieval results. SCODA can also be applied for the detection of noctilucent clouds (NLC), the highest clouds in the Earth's atmosphere, as mentioned by Eichmann *et al.* (2009), along with a wide range of cloud types. In the following, a description of the algorithm is given.

The core of the algorithm is the use of the different light scattering properties of cloud particles compared to scattering by gaseous species like oxygen or nitrogen. Neglecting clouds (and aerosols with large particle sizes), scattering in the atmosphere can be described by Rayleigh scattering (page 39, Houghton, 2002).

Similar to solar radiation modified by absorption, scattering can be described by

$$I = I_0 \exp(-\int \sigma\rho \, dz) \tag{2.19}$$

with ρ as the number density of the absorber, dz as the path length through the atmosphere, I_0 as the light intensity before scattering, and I as the intensity after scattering. The scattering coefficient σ is of main interest here. In the case of Rayleigh scattering, σ can be described by

$$\sigma_R = \frac{32\pi^2}{3N_0\lambda^4\rho_0}(n-1)^2. \tag{2.20}$$

In this equation N_0 is the number of molecules per unit volume, ρ_0 the density of air and n the refractive index. Notice the strong wavelength dependence with λ^{-4}. Blue light is scattered about 9 times stronger than red light, which is also the reason why the sky is blue.

If the size of the particle is of the same order of magnitude or larger than the wavelength of the scattered light, Rayleigh scattering does not describe the results correctly. For spherical particles, the Mie scattering theory (Mie, 1908) can be applied, which results in a wavelength dependence of $\lambda^{-\alpha}$ with α between 0 and 4. This is also the case for clouds (typical cloud droplet sizes are about 20 μm), which thus show a weaker wavelength dependence than Rayleigh scattering particles. This dependence of the spectral features on the particle sizes information on the cloud contamination of air parcels can be retrieved.

The spectral regions used for this need to avoid strong absorber lines and should not include shorter wavelengths (i.e. UV), as the atmosphere becomes optically thick for these wavelengths and low tangent heights. For general cloud detection, the wavelength pair 1090 nm (λ_1) and 750 nm (λ_2) is commonly used. Additionally, the wavelength pair 1550 nm and 1630 nm is chosen for the detection of ice clouds. The measured radiation is integrated over small spectral windows (2 - 4 nm) around these wavelengths to improve the signal-to-noise-ratio. Fig. 2.11 shows the application of the 1090 nm/750 nm wavelength pair for the detection of polar stratospheric clouds (PSCs). However, larger spectral windows (around 10 nm) are applied in that case.

To detect clouds, the color index R_c is calculated from the intensities, depending on tangent height (TH) with the intensity I and the wavelengths λ_1 and λ_2:

$$R_c(TH) = \frac{I(\lambda_1, TH)}{I(\lambda_2, TH)} \tag{2.21}$$

Using the color indexes of two neighbouring tangent heights the color index ratio $\Theta(TH)$ is calculated:

$$\Theta(TH) = \frac{R_c(TH)}{R_c(TH + \Delta TH)}. \tag{2.22}$$

A cloud is detected if $\Theta(TH)$ is above a pre-selected threshold. An application for the detection of polar stratospheric clouds (PSCs) can be seen in Fig. 2.12.

The SCODA cloud retrieval algorithm is capable of cloud detection in a most convenient way for our NO_2 retrievals. Using these results one can discard all cloud contaminated scenes. It is also possible to receive information about the cloud type (e.g. water or ice) and to some degree the cloud coverage in the investigated area. As cloud contamination is a valid concern for the quality of NO_2 retrieval results, a reliable method to detect clouds is important.

2.4 NO_2 retrieval with SCIATRAN

The SCIATRAN software package (Rozanov, 2012) is both a radiative transfer model and a retrieval algorithm, that can be adjusted for a wide selection of scientific tasks. Although only the NO_2 retrieval for limb mode is described in this section, certain other features are also used in this work. The possibility to simulate spectra starting with a given vertical NO_2 profile is used for sensitivity studies (see section 3.3.1), and the cloud simulation capabilities are adapted for cloud sensitivity studies (see section 3.1.1). The SCIATRAN NO_2 retrieval described here is Version 3.1 and represents the

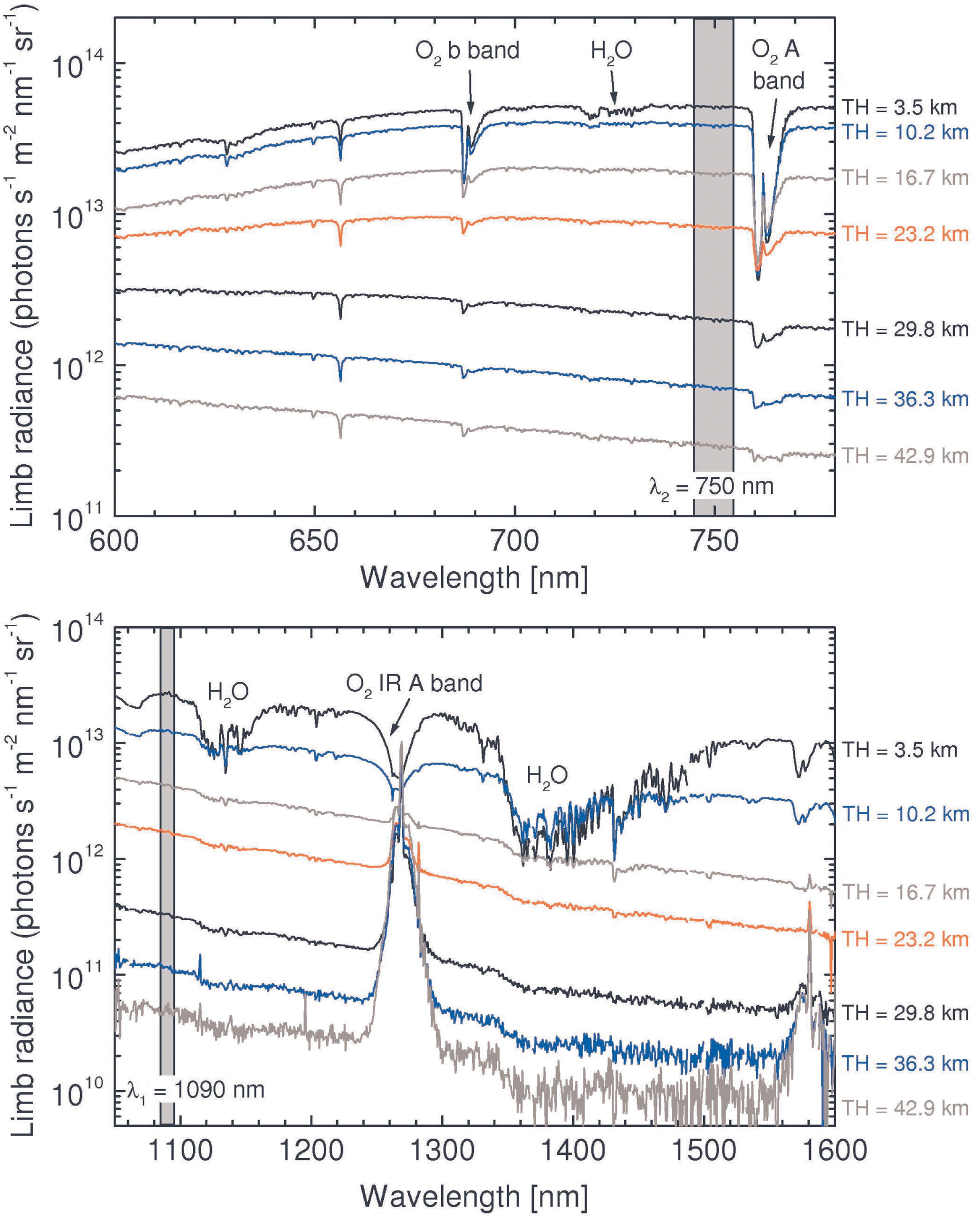

Figure 2.11: Calibrated limb spectra for SCIAMACHY channel 4 (top) and 6 (bottom) for an example measurement. Source: von Savigny *et al.* (2005)

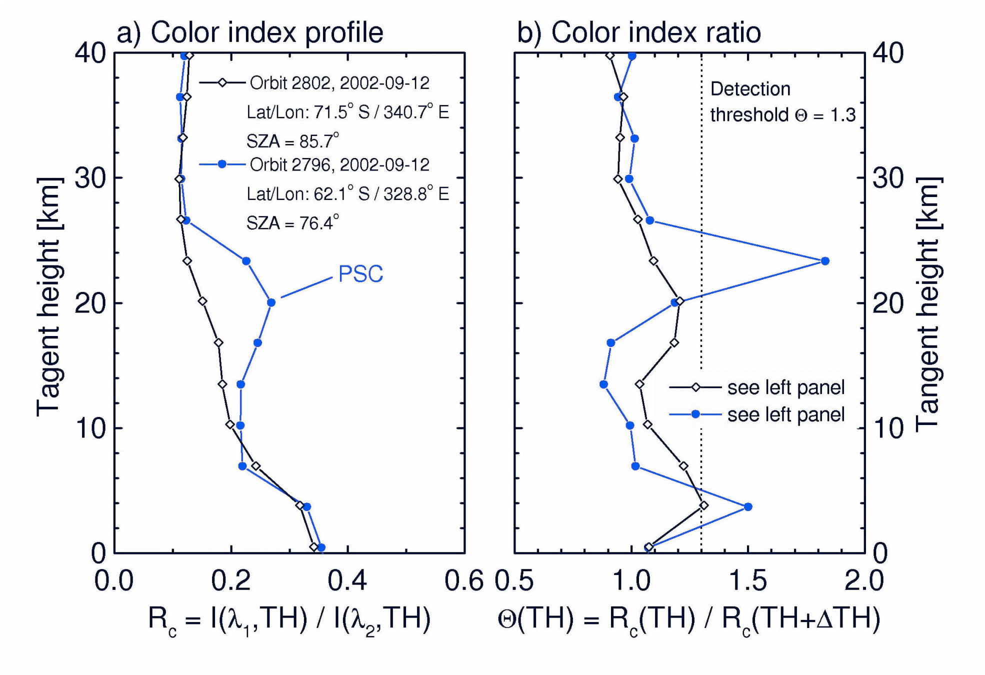

Figure 2.12: Sample color index profiles (left panel, $\lambda_1 = 1090$ nm and $\lambda_2 = 750$ nm) and color index ratio profiles (right panel) in case of PSC contaminated measurements (blue) and a background profile (black). Source: von Savigny *et al.* (2005)

standard before improvements regarding UTLS sensitivity were implemented. The version number must not be confused with the version number of the SCIATRAN package. SCIATRAN V2.2 is used for the NO$_2$ limb data product Version 3.1. In the context of this work, the improved NO$_2$ product version (see section 3.3.2) is designated as Version 3.2.

The aim of the retrieval process is to solve the inverse problem. It is far more difficult to compute the trace gas amounts from a set of measured spectra than generating spectra given a known set of trace gases and their absorption features. The radiative transfer equation, which provides the relation between radiance measured by the instrument and atmospheric parameters, needs to be inverted. Several algorithms and solution methods are known, and two of them are used in this work, the information operator approach (Doicu *et al.*, 2007; Hoogen *et al.*, 1999; Kozlov, 1983; Rozanov, 2001) in Version 3.1 and the optimal estimation (Rodgers (2000), see also Figure 2.13) method in Version 3.2. The focus in this chapter is on the information operator approach, but both methods are discussed as they are essential for further discussion.

A representation of the data model can be given as

$$\boldsymbol{y} = \boldsymbol{F}(\boldsymbol{x}), \tag{2.23}$$

where $\boldsymbol{F}$ is the radiative transfer operator, $\boldsymbol{y}$ the data vector and $\boldsymbol{x}$ the state vector. $\boldsymbol{x}$ contains the atmospheric parameters to be retrieved, e.g. aerosol characteristics or molecular density profiles, like NO_2 vertical profiles. Instruments can only perform measurements with a finite accuracy, therefore only a noise-contaminated data vector $\boldsymbol{y}_\varepsilon$ is available:

$$\boldsymbol{y}_\varepsilon = \boldsymbol{F}(\boldsymbol{x}) + \varepsilon. \tag{2.24}$$

The retrieval process is divided into two major steps. The first is the pre- processing step, which is performed to eliminate spectral features, which are not linked to the retrieval parameters.

The main features of pre-processing can be described in an equation system as follows:

$$\begin{aligned}
\{\boldsymbol{y}_\varepsilon\}_{\mathtt{N_L(k-1)+L}} &= \ln\left[\frac{I^{\mathrm{meas}}(\lambda_\mathrm{L}, h_\mathrm{k})}{I^{\mathrm{meas}}(\lambda_\mathrm{L}, h_\mathrm{ref})}\right] - P_n^{\mathrm{meas}} - \sum_{i=1}^{N_i} s_{k,j} W_i(\lambda_\mathrm{L}), && (2.25)\\
\{\boldsymbol{F}(\boldsymbol{x}_\mathrm{a})\}_{\mathtt{N_L(k-1)+L}} &= \ln\left[\frac{I^{\mathrm{sim}}(\lambda_\mathrm{L}, h_\mathrm{k})}{I^{\mathrm{sim}}(\lambda_\mathrm{L}, h_\mathrm{ref})}\right] - P_n^{\mathrm{sim}}, && (2.26)\\
\{\mathbf{K}\}_{\mathtt{N_L(k-1)+L,j}} &= \left.\frac{\delta\,\{\boldsymbol{F}(\boldsymbol{x})\}_{\mathtt{N_L(k-1)+L}}}{\delta\,\{\boldsymbol{x}\}_\mathtt{j}}\right|_{\boldsymbol{x}=\boldsymbol{x}_\mathrm{a}} - P_n^{\mathrm{wf}}, && (2.27)\\
\mathtt{L} = \mathtt{1},\ldots,\mathtt{N_L}, \quad & \mathtt{k} = \mathtt{1},\ldots,\mathtt{N_k}, \quad \mathtt{j} = \mathtt{1},\ldots,\mathtt{N_j},
\end{aligned}$$

This equations contain the spectral information for all spectral points λ_L for all used tangent heights h_k. As in the DOAS (Differential Optical Absorption Spectroscopy, Platt, 1994) technique the uppermost tangent height h_ref is used as a 'background', i.e. the limb radiances are normalized with respect to the radiance at this tangent height. By this approach, the solar Fraunhofer structures are eliminated as a problem and the influence of the instrument response function is reduced. No absolute calibration is needed. This also reduces the problem of instrument degradation over the years of operation in space. With the exception of the reference tangent height h_ref, the pre-processing is performed independently for each tangent height.

Smoothly varying functions of wavelength (e.g. Rayleigh and Mie scattering) are taken into account by polynomial subtraction, with a polynomial P_n of order n. In the data model also a total number of N_i correction spectra are subtracted as $W_i(\lambda_\mathrm{L})$ to deal with features, which are not yet described in the model. Several instrument effects (tilt, undersampling, spectral misalignment and others) are described this way and also some natural phenomena, e.g., the Ring effect. Correction spectra are also known as pseudo- absorbers, for more information on this topic see Haley *et al.* (2004); Sioris *et al.* (2003). In the pre-processing step, the coefficients for the polynomials and also the scaling factors for the spectral corrections are obtained by fitting the logarithms of the normalized limb radiance in the wavelength domain for each tangent height separately. Also, shift and squeeze corrections are applied.

NO$_2$ is not the only important line absorber in the investigated spectral region of 420 to 470 nm. Another relevant absorber is ozone, which has to be retrieved in the process, as well. The state vector $\boldsymbol{x}$ contains information about both species. In the forward model, O$_4$ is also considered. However, this species is not retrieved in the inverse approach.

After the preprocessing step, several retrieval methods are possible. The optimal estimation (Rodgers, 2000) is discussed at the end of this section as it is used in the Version 3.2 retrieval. First, the information operator approach used in SCIATRAN V3.1 NO$_2$ is described. To meet the requirements of statistical inversion methods (e.g. optimal estimation, information operator approach), the measurement error ε has to be stochastic, normally distributed and needs to have a mean value of zero. Another requirement is that the problem has to be linear. Introducing an initial guess $\boldsymbol{x}_0$ the problem can be linearized:

$$\boldsymbol{y}_\varepsilon = \boldsymbol{F}(\boldsymbol{x}_0) + \left.\frac{\delta \boldsymbol{F}(\boldsymbol{x})}{\delta \boldsymbol{x}}\right|_{\boldsymbol{x}=\boldsymbol{x}_a} \times (\boldsymbol{x} - \boldsymbol{x}_0) + \cdots + \varepsilon \tag{2.28}$$

This initial guess $\boldsymbol{x}_0$ is referred to as the a priori state vector, which represents the best available estimation of the true solution before retrieval. A linear relation is obtained from equation 2.28 by neglecting higher order terms, leading to:

$$\boldsymbol{y}_\varepsilon \approx \boldsymbol{F}(\boldsymbol{x}_0) + \left.\frac{\delta \boldsymbol{F}(\boldsymbol{x})}{\delta \boldsymbol{x}}\right|_{\boldsymbol{x}=\boldsymbol{x}_0} \times (\boldsymbol{x} - \boldsymbol{x}_a) + \varepsilon = \boldsymbol{F}(\boldsymbol{x}_0) + \mathbf{K}_0(\boldsymbol{x} - \boldsymbol{x}_0) + \varepsilon \tag{2.29}$$

In this equation, $\mathbf{K}_0$ is a linear forward model operator. Thus, the retrieval problem (Eq. 2.24) can be written as:

$$\boldsymbol{y}_\varepsilon = \boldsymbol{F}(\boldsymbol{x}_0) + \mathbf{K}_0(\boldsymbol{x} - \boldsymbol{x}_0) + \epsilon \tag{2.30}$$

Since also linearization errors are included, ϵ represents measurement errors, as well as the linearization error. To find a solution for the inverse problem the following quadratic form needs to be minimized:

$$\boldsymbol{F}(\boldsymbol{x}) = \left\| \boldsymbol{F}(\boldsymbol{x}_0) + \mathbf{K}(\boldsymbol{x} - \boldsymbol{x}_0) - \boldsymbol{y}_\epsilon \right\|^2_{\mathbf{S}_\epsilon^{-1}} + \left\| (\boldsymbol{x} - \boldsymbol{x}_0) \right\|^2_{\mathbf{R}} \tag{2.31}$$

In this equation, $\mathbf{S}_\epsilon$ is the noise covariance matrix. The diagonal elements of $\mathbf{S}_\epsilon$ are determined in accordance with noise level estimates from the fit residuals obtained in the pre-processing step. Assuming spectrally uncorrelated noise, off-diagonal elements are set to zero. In the above equation, $\mathbf{R}$ is the regularization matrix, which is defined as:

$$\mathbf{R} = \mathbf{S}_0^{-1} + \mathbf{T} \tag{2.32}$$

The a priori covariance matrix $\mathbf{S}_0$ is based on selected a priori uncertainties. Additionally, the smoothness constraint matrix $\mathbf{T}$ is applied, based on the retrieval, see Table 2.2 for Version 3.1. Smoothing helps to suppress oscillations in the retrieval results, while overconstraining is avoided for the retrieval on a fine altitude grid. Note that the retrieval is performed on a 1 km grid, while the SCIAMACHY limb mode has a vertical step size of 3.3 km.

As it is explained for the retrieval of BrO (bromine oxide) in Rozanov *et al.* (2011), the a priori covariance matrix $\mathbf{S}_0$ for a particular species to be retrieved is set as follows:

$$\{\mathbf{S}_0\}_{i,j} = \sigma_i \sigma_j \exp\left(-\frac{|z_i - z_j|}{I_c} \right). \tag{2.33}$$

In this equation, I_c is the correlation length. σ_i and σ_j are the a priori uncertainties at the altitude levels z_i and z_j, which are set to 100% for NO_2 and 1000% for O_3. In the case of O_3, this results in almost no regularization caused by a priori uncertainty. The full a priori matrix is defined as

$$\mathbf{S}_0 = \begin{bmatrix} \mathbf{S}_0^{O_3} & \mathbf{0} \\ \mathbf{0} & \mathbf{S}_0^{NO_2} \end{bmatrix}, \tag{2.34}$$

where $\mathbf{0}$ represents submatrices with all entries equal to zero.

The non-zero elements of the smoothing constraint matrix **T** are defined for each species k as

$$\{T_k\}_{i,i-1} = \frac{t_{k,i}}{\sigma_{k,i}(z_{i-1} - z_i)} \tag{2.35}$$

$$\{T_k\}_{i,i} = -\{T_k\}_{i,i-1} \tag{2.36}$$

Here, $\sigma_{k,i}$ is the standard deviation of species k at altitude i, and i runs through all altitude levels with the exception of the first one. $t_{k,i}$ is the selected smoothness coefficient. With this, the regularization matrix is given as:

$$\mathbf{R} = \mathbf{S}_0^{-1} + \begin{bmatrix} \mathbf{T}_{\mathbf{O_3}} & \mathbf{0} \\ \mathbf{0} & \mathbf{T}_{\mathbf{NO_2}} \end{bmatrix}^T \times \begin{bmatrix} \mathbf{T}_{\mathbf{O_3}} & \mathbf{0} \\ \mathbf{0} & \mathbf{T}_{\mathbf{NO_2}} \end{bmatrix} \tag{2.37}$$

For V3.1 the NO_2 smoothing parameter decreases from 10 at 50 km to 1.0 at 10 km, which represents stronger smoothing at high altitudes.

To solve the minimization problem (Eq. 2.31) the information operator approach (Doicu *et al.*, 2007; Hoogen *et al.*, 1999; Kozlov, 1983) is applied. The idea and advantage of the information operator approach with respect to the optimal estimation approach is that in the ideal case only those parameters are used in the fitting process, which contain information. In this approach, the solution is projected into the space of eigenvectors of the information operator, which is defined by

$$\mathbf{P} = \mathbf{R}^{-1}\mathbf{K}^T\mathbf{S}_\epsilon^{-1}\mathbf{K}. \tag{2.38}$$

With a particular measurement only an effective state subspace can be accessed, which is limited by considering only eigenvalues larger than a selected threshold value. The Gauss–Newton iterative scheme is employed to account for the non-linearity of the inverse problem and the solution at the $(i+1)$-th iterative step is written as

$$\boldsymbol{x}_{i+1} = \boldsymbol{x}_i + \sum_{\mathtt{k=1}}^{\mathtt{N_i}} \beta_{i,k}\psi_{i,k}, \tag{2.39}$$

where $\psi_{i,k}$ are the eigenvectors of the information operator **P**. The number of eigenvectors whose eigenvalues are larger than the selected threshold value is represented by `Ni` and the expansion coefficients $\beta_{i,k}$ are given by

$$\beta_{i,k} = \frac{\eta_{i,k}}{c_{i,k}(1+\eta_{i,k})}\,\psi_{i,k}^T\,\mathbf{K}_i^T\mathbf{S}_\epsilon^{-1}\Big(\boldsymbol{y}_\epsilon - \boldsymbol{F}(\boldsymbol{x}_i) + \mathbf{K}_i\,(\boldsymbol{x}_i - \boldsymbol{x}_0)\Big). \tag{2.40}$$

Here, $\eta_{i,k}$ denotes the eigenvalue of the information operator **P**, corresponding to the eigenvector $\psi_{i,k}$, and $c_{i,k}$ is the following scalar product:

$$c_{i,k} = \left\langle \mathbf{K}_i^T \mathbf{S}_\epsilon^{-1} \mathbf{K}_i \, \psi_{i,k} | \psi_{i,k} \right\rangle . \tag{2.41}$$

The iterative process is terminated, when the maximum difference between the components of the solution vector at two subsequent iterative steps does not exceed 1%. Typically three to five iterations are required to achieve convergence.

This approach is applied in the current version of the SCIATRAN NO_2 limb retrieval processor Version 3.1. The settings are listed in Table 2.2.

The above described SCIATRAN V3.1 NO_2 retrieval is in two ways very important for this work: It forms the basic retrieval, which has been modified for improved NO_2 UTLS sensitivity, see section 3.3.2, and it also provides a priori NO_2 profiles of high quality, which are then used for the improved retrieval.

Overview of possible improvements

Several possible improvements can be considered in order to increase the sensitivity of the retrieval process regarding NO_2 results in the UTLS altitude region. In this work mainly two of them are investigated in detail:

- Choice of an optimal retrieval method: SCIATRAN features Optimal Estimation, Tikhonov regularization and the Information Operator Approach. Analyzing the quality and stability of the results regarding the UTLS region is of high importance for choosing the optimal method.
- Use of different spectral windows in order to receive more spectral information.

Although SCIATRAN is used for retrievals in this work, other retrieval programs and methods are discussed including their relative performance for NO_2 UTLS limb retrievals.

Discussion of third-party retrieval implementations

Different retrieval methods which are linked to the data sources used for validation are described in section 2.5. In this section, a selection of retrieval methods other than SCIATRAN for SCIAMACHY or similar satellite instruments are presented. This

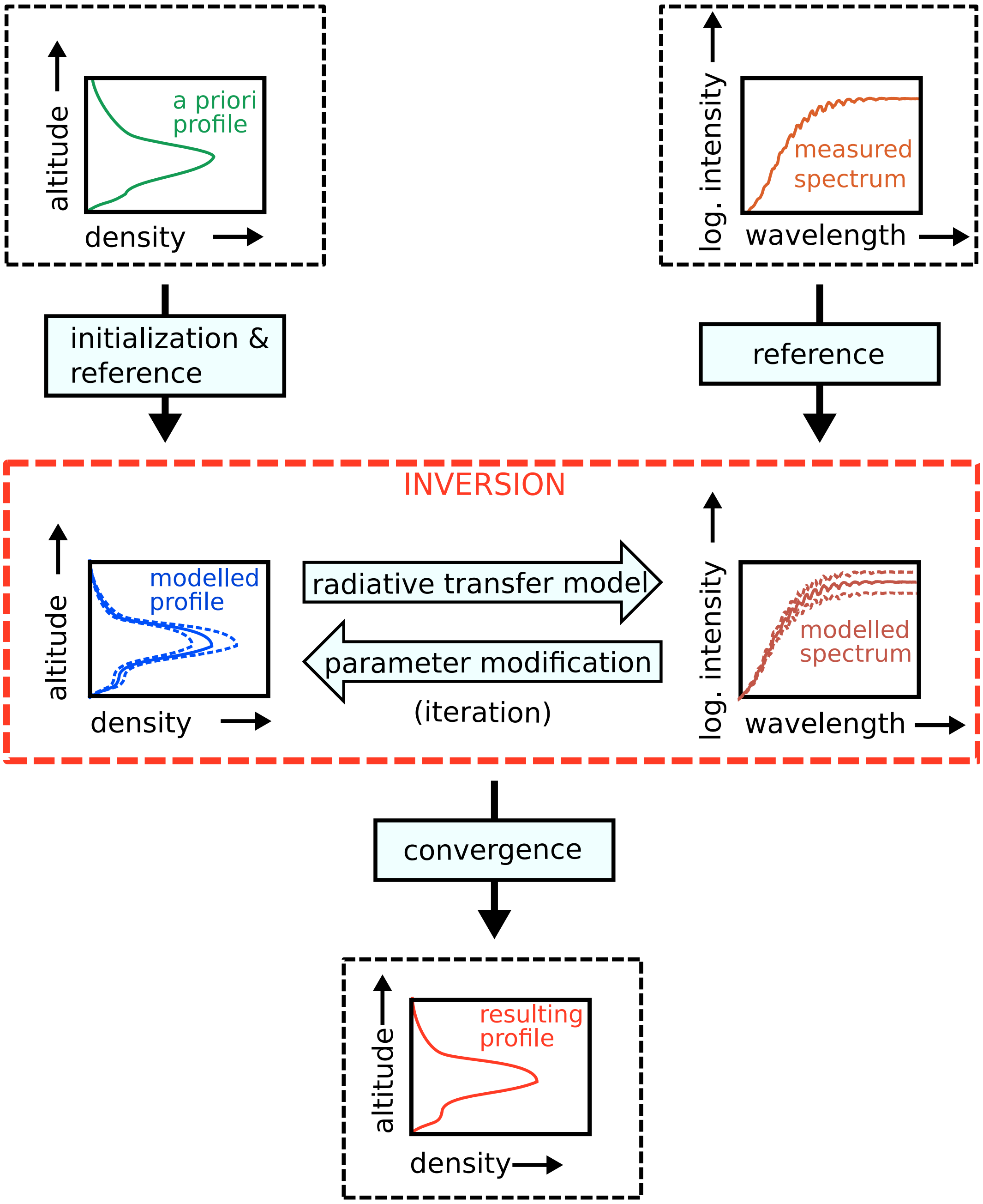

Figure 2.13: In this figure the optimal estimation method is illustrated.

SCIAMACHY NO_2 limb V3.1 retrieval parameter settings	
Forward model	SCIATRAN 2.2
Spectral region	420 – 470 nm
Surface albedo	0.3
Cloud treatment	neglected in the retrieval, cloud information included in the output files
Weighting function type	single scattering
Atmospheric species in the forward model	NO_2, O_3, O_4
Retrieved atmospheric species	NO_2, O_3
Reference tangent height number	15 ($\approx$ 43 km)
Tangent heights selected for the retrieval	5 – 14 ($\approx$ 10 – 40 km)
Polynomial order	3
Spectral corrections	shift, offset, undersampling, eta, ring
Spectral smoothing	not applied
A priori uncertainty	5×10^9 molecules/cm^3
Signal to Noise Ratio	estimated from spectral residuals
Correlation length	1.5 km
Additional regularization	Tikhonov smoothing (smoothing parameter linearly decreases with altitude from 10 at 50 km to 1.0 at 10 km)
Solution method	Information Operator Approach
Eigenvalue threshold	0.01
Iterative scheme	Newton

Table 2.2: SCIATRAN V3.1 NO_2 limb retrieval parameter settings

serves both as an overview of the implementation of different retrieval methods, as well as background information, as several data sets obtained with these methods are used in the present.

Mainz SCIAMACHY NO_2 retrieval featuring a least squares approach

One retrieval method is described in Puķīte *et al.* (2006), while an overview of the first results and the algorithm performance is given in Kühl *et al.* (2008). Besides NO_2, two other species are also discussed for retrieval, BrO and OClO, which play a role in the depletion of ozone in polar spring and are related to the Antarctic ozone hole, see Solomon (1999); Wennberg *et al.* (1994).

The method is described as a two-step approach. This division must not be confused with the approach described in the present work in section 3.3.2 as the details of each step are quite different. The approach however is not developed with the specific goal of improving the NO_2 UTLS sensitivity only, but to accelerate the overall retrieval process by dividing the retrieval into two separate steps. In the first step, a Differential Optical Absorption Spectroscopy (DOAS) approach (Platt, 1994) is used to retrieve slant column densities (SCDs). A SCD is the integrated concentration of the absorber along the light path. In the second step, box air mass factors calculated by the Monte-Carlo-Method are used as weighting functions to convert the SCDs to vertical concentration profiles.

For the inversion (second step) different methods can be applied. While an optimal estimation approach (Rodgers, 2000) is implemented, the a priori independent least squares fitting (LSQ) technique can also be used, see Menke (1999). Avoiding the usage of a priori profiles has the advantage of avoiding the influence of a priori in general. However, it is stated in Puķīte *et al.* (2006), that below 15 km and above 40 km it is still necessary to apply a priori profiles. Instead of this a priori-free approach, the more widely used optimal estimation method is therefore employed for the retrieval in the UTLS altitude region, which is found usually below 15 km. Despite this conclusion, a description of both retrieval methods is given.

The first step in the two-step-approach remains the same for both retrieval algorithms, as the retrieval of the SCDs is in both cases performed with a DOAS approach, see Platt (1994). Based on the Beer-Lambert Law, one can determine optical densities of trace gas absorptions. Information is needed on the spectral absorptivity of the trace gases, which are to be retrieved. This is provided by absorption cross sections. In the case of NO_2, the 223 K cross section from Bogumil *et al.* (2003) is used. In the DOAS approach, not the absolute absorption structures are utilized, but they are separated into broadband and differential cross sections. The retrieval generates slant column densities (SCD) as results. The optical density is related to this, as the product of the SCD and the respective absorption cross section yields the optical density of an absorber.

Similar as in other retrieval approaches, several spectral features are accounted for, including Ring spectra (Ring effect) and a polynomial of degree 3 to 5 to deal with broadband features. In addition, eta and zeta spectra are used to correct for polarization features. For the NO_2 retrieval, the 420 to 450 nm spectral region is used and the reference spectrum is taken at a tangent height of about 42 km. Contrary to the current SCIATRAN product retrieval (see section 2.4), the four different horizontal retrieval sections are averaged, i.e. not 240 km wide sections are investigated, but the hole 960 km is used for one profile.

In the second step, the trace gas profiles are determined from the slant column densities. Using a 3D full spherical Monte Carlo method (Wagner *et al.*, 2007), box air mass factors (AMF) are calculated. The matrix of calculated AMFs $\boldsymbol{A}_{mn}$ describes the impact of the trace gas concentrations x_n at all considered layers of the atmosphere on the SCDs y_m as follows:

$$\boldsymbol{y}_m = \boldsymbol{A}_{mn}\boldsymbol{x}_n + \boldsymbol{\epsilon}_n. \tag{2.42}$$

ϵ is the measurement error. Equation 2.42 needs to be inverted to retrieve the trace gas concentrations, it is however not exact and can be both under-determined as well as over-determined. Two methods are available to continue the retrieval process.

The least squares approach mentioned before offers the following equation to solve the problem:

$$\hat{\boldsymbol{x}}_d = (\boldsymbol{A}^T\boldsymbol{S}_\epsilon^{-1}\boldsymbol{A})^{-1}\boldsymbol{A}^T\boldsymbol{S}_\epsilon^{-1}\boldsymbol{y}, \tag{2.43}$$

in which $\boldsymbol{S}_\epsilon$ is the measurement error covariance matrix. This solution provides reasonable results only if the altitude range is restricted to 15 km to 42 km.

As an alternative, the optimal estimation approach can be used, which also yields averaging kernels. The a priori information for the NO_2 profile retrieval is taken from different sources in order to determine the a priori influence on shape and magnitude of resulting profiles.

While the results of this retrieval are useful, the improvement of the UTLS NO_2 retrieval is not considered. The advantages of avoiding a priori profiles cannot be utilized below 15 km, as a priori information is still needed at this altitude range to stabilize the retrieval. A cloud masking method may be added in the future, as mentioned in Kühl *et al.* (2008).

NO_2 limb retrieval for OSIRIS used for the search of lightning events

Another method used for NO_2 retrieval was developed mainly for a further limb instrument other than SCIAMACHY. The Canadian satellite instrument OSIRIS on board the Swedish research satellite Odin (launched on February 20, 2001) is also capable of performing limb measurements, see Llewellyn *et al.* (2004). The Optical Spectrograph and InfraRed Imager System (OSIRIS) is specifically designed to obtain altitude profiles of minor atmospheric species in limb geometry. A spectral range of 280 to 800 nm is covered with a resolution of about 1 nm. The vertical field of view is about 1 km for the limb scans, and with repetitive measurements the altitude range from about 10 km to 100 km is covered. Also a three channel infrared imager is installed, but is not considered for the NO_2 retrieval. The achieved vertical resolution of about 2 km is somewhat better as compared to SCIAMACHY with about 3 km. The horizontal field of view is only 30 km compared to 110 km for SCIAMACHY, while the horizontal sampling at tangent point for a limb measurement is 200 km for OSIRIS and 240 km for SCIAMACHY, if the full horizontal scan of 960 km is not needed. However, the spectral resolution for OSIRIS is stated to be only about 1 nm, while SCIAMACHY features a resolution of about 0.44 nm or 0.48 nm, respectively, for the same spectral region, see Table 2.1.

A basic retrieval method for OSIRIS NO_2 is described in Haley *et al.* (2004). It features a DOAS retrieval to yield column densities, which are used to compute trace gas profiles using a *maximum a posteriori* approach (Rodgers, 2000). It also uses a least squares fitting approach, however, already in the DOAS part of the retrieval. The retrieval is not a priori free as the alternative SCIAMACHY retrieval described in the previous section. The spectral region 435 nm – 451 nm is used for the NO_2 retrieval and the retrieved profiles show an accuracy of 10% in the altitude range from 15 km to 40 km with a vertical resolution of about 2 to 3 km (Haley *et al.*, 2004).

For NO_2 in the UTLS region, Sioris *et al.* (2007) present a different approach used specifically for the detection of lightning events. By using the method described before and a comparison with a photochemical model, a handful of measurements is selected, which are candidates for observation of lightning events. Also a cloud masking method is used to determine the cloud top height and to discard cloud-contaminated measurements.

The main difference to the basic retrieval method is the usage of Chahine's relaxation method for the inversion part of the retrieval, see Chahine (1970). This method is chosen, because it is mostly independent of the first guess for the retrieval and also preserves the vertical resolution at lower altitude ranges, which is about 2 km for OSIRIS. Large deviations from the first guess are not suppressed, and as NO_2 enhancements by lightning events are estimated to be very high, but also very localized, the retrieval approach is well-suited for this task. Also, a surface albedo database has been included into the retrieval.

The implementation of Chahine's relaxation method is described in Sioris *et al.* (2003). The retrieval process consists of iterative updates, starting with a first guess, the number density $x_{i=0,z=40}$, with i as the iteration number and z as the altitude in km. Simulated SCDs ($y_{0,40}$) can be obtained from this, which can be compared to the measured SCDs $y_{t,40}$. For the first step in Chahine's method $x_{1,z} = x_{0,z} + \Delta x_{1,z}$, the relation is as follows:

$$x_{1,z} = x_{0,z}(y_{t,z}/y_{0,z}) \tag{2.44}$$

This first step does not lead to a good agreement between modelled and measured SCD, but after several iterations convergence can be achieved. The correction $\Delta x_{i+1,z}$ is given as

$$\Delta x_{i+1,z} = \Delta x_{i,z} \frac{y_{t,z} - y_{i,z}}{|y_{i,z} - y_{i-1,z}|} \tag{2.45}$$

Thus, using the two guesses above, the algorithm creates a new estimation for the number densities by interpolation or extrapolation of modeled number densities. This is repeated, until modeled SCDs and measured SCDs agree. Also, this method is performed only for the respective lowermost layer at each iteration step from top to bottom altitude to save computation time. Only after convergence for each tangent height is reached, the influence of lower tangent heights on higher tangent heights is addressed.

The above approach is mainly used for the investigation of single profiles and very high, localized emission sources. Under these circumstances, a detection of NO_2 events in single profiles might be feasible. In section 4.2 it is investigated, if the retrieval approach described in this work (see section 3.3.2) also detects enhanced NO_2 amounts for the lightning events reported.

Summary

The Mainz SCIAMACHY NO_2 retrieval (Puķīte *et al.*, 2006) is very promising, when the least squares approach is performed, as it does not include a priori profiles. This is still an advantage, although the altitude range is limited in this case (15 to 42 km) and methods, which include a priori profiles do not show high influence by the a priori for these altitudes. As there is no a priori profile included, under no circumstances can a priori profiles have an influence on the results.

The retrieval method described by Sioris *et al.* (2007) is adopted especially for very large localized NO_2 emissions in the UTLS region, and it is used to detect lightning events. For other altitude ranges, however, a more conventional retrieval method (Haley *et al.*, 2004) is applied.

2.5 Data sources for validation

To determine the quality of NO_2 retrieval results, they need to be validated. Retrieved NO_2 profiles from different, independent data sources are needed for this task. The described data sources in this chapter are measurements by the satellite instruments SAGE II (Stratospheric Aerosol Gas Experiment) in section 2.5.1, HALOE (Halogen Occultation Experiment) in section 2.5.2, and ACE-FTS (Atmospheric Chemistry Experiment-Fourier Transform Spectrometer) in section 2.5.3, balloon borne measurements (Butz *et al.*, 2006) in section 2.5.4, and observations by the airborne instruments SPURT (German: Spurenstofftransport in der Tropopausenregion, trace gas transport in the tropopause region, Engel *et al.* (2006)) and CARIBIC (Civil Aircraft for the regular investigation of the atmosphere based on an instrumented container, Brenninkmeijer *et al.* (2007)), see section 2.5.5. In section 2.5.6, results from the atmospheric chemistry model EMAC are presented (ECHAM5/MESSy Atmospheric Chemistry model (Jöckel, 2012; Jöckel *et al.*, 2006)).

2.5.1 SAGE II

The Stratospheric Aerosol Gas Experiment (SAGE II, Chu *et al.*, 1989; Cunnold *et al.*, 1991) was an occultation instrument aboard the United States Earth Radiation Budget Satellite (ERBS) launched in 1984. Although planned with an operation time of two years, ERBS delivered data until the end of August in 2005. This very long operation time (21 years) provides an overlap with SCIAMACHY from 2002 to 2005. With the SAGE II instrument, aerosols, O_3, NO_2 and water vapour were measured.

The instrument is a sun-photometer with seven spectral channels. From the instantaneous field-of-view a vertical resolution of 0.5 km can be calculated. The holographic grating disperses the incoming radiation. This leads to seven spectral regions centered at 1020, 940, 600, 525, 453, 448 and 385 nm, where measurements take place. The SAGE II instrument data covers the whole global longitudinal range and latitudes from 80° N to 80° S.

SAGE II version 6.2 data products are used in this study. The vertical resolution of NO_2 profiles included there is 2 km. The data products also provide error values, which include measurement errors, altitude uncertainty, aerosol contributions, errors from the removal of ozone and temperature profile errors (which affect the removal of the Rayleigh-scattered contributions). For more information on this see Gordley *et al.* (1996). The errors for SAGE II NO_2 are less than 5% to 10% at altitudes between 25 km to 35 km for most measurements. At height levels below 25 km these errors can exceed 50% and above 35 km error values above 10% are found in the data product files.

2.5.2 HALOE

Launched on September 12, 1991 the UARS satellite (Upper Atmosphere Research Satellite) carried several instruments for the investigation of the Earth's atmosphere. One of its ten instruments was the Halogen Occultation Experiment (HALOE, Russel III & Remsberg, 2012; Russell III *et al.*, 1993). HALOE was created to perform solar occultation measurements of ozone (O_3), hydrogen chloride (HCl), hydrogen fluoride

(HF), methane (CH_4), water vapour (H_2O), NO, NO_2 and aerosol extinction at 4 infrared wavelengths. Additionally, pressure and temperature vertical profiles were retrieved. The altitude range which was covered by HALOE for each trace gas is shown in Fig. 2.14. The latitudinal coverage is 80° South to 80° North, which is achieved over the course of one year. Special observations were performed above the Antarctic region during spring. Among others, the scientific purpose of the instrument was to investigate stratospheric ozone depletion, determine the anthropogenic contribution to this phenomenon and also to retrieve aerosol extinction coefficients.

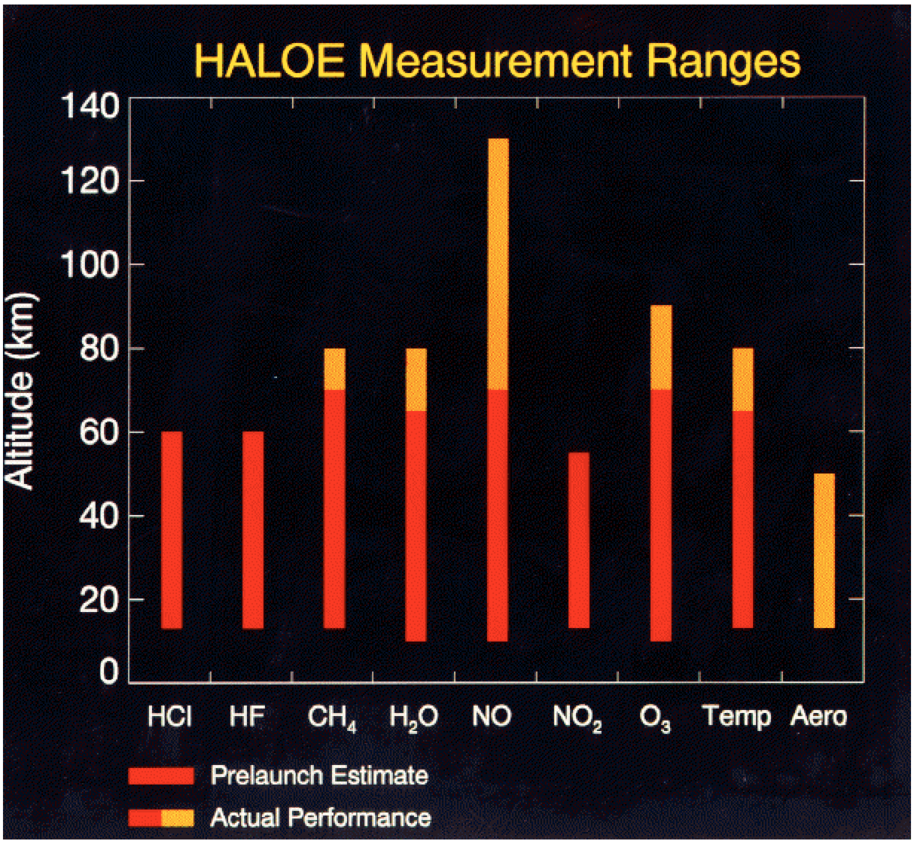

Figure 2.14: This figure shows the altitude ranges covered by HALOE retrieved vertical profiles. For example, the NO_2 vertical range reaches from about 15 to about 50 km. Source: Russel III & Remsberg (2012)

The UARS satellite and with it the HALOE instrument has been decommissioned on November 21, 2005. Since ENVISAT has been launched in March 2002, this results in 3 years overlap in which both instruments were active and comparisons are possible. Since the HALOE NO_2 vertical profiles are used for validation in this study, this product is described in some more detail. For the present work, the current HALOE data version 19 is used.

As discussed in Gordley *et al.* (1996), NO_2 is retrieved from a different spectral region outside the spectral range covered by SCIAMACHY. The HALOE NO_2 retrieval is based on the channel centered at 6.25 μm, while the NO retrieval is performed using the channel centered at 5.26 μm.

The HALOE NO_2 channel uses a broadband radiometer equipped with a spectral bandpass filter. Other trace gas absorbers in this channel are H_2O, CH_4, N_2O, and O_2. These and also the aerosol concentrations are considered in the retrieval as follows: The O_2 concentration is known. H_2O and CH_4 are retrieved using a different HALOE channel, respectively. The aerosol concentration is retrieved using the NO channel. Only N_2O cannot be retrieved elsewhere, it is only a minor absorber in that spectral region for lower altitudes.

The retrieval method used is a modified onion peeling method, which was chosen for numerical efficiency. It is described in Gordley *et al.* (1994) with respect to its application for occultation retrievals. In this method, the atmosphere is described as consisting of cells, or tangent cells in the limb retrieval case. The ray path integration of transmission and radiance is performed starting with the outermost cell. This allows updating the total ray by updating the tangent layer transmission, which is much faster than recalculating the total ray. Also, the uppermost layer or cell is used to approximate the conditions in the atmosphere above. The algorithm allows to include filter shift, Doppler shift and gas cell spectra.

For NO_2 a vertical resolution of about 2 km is achieved. In comparison, due to computational limitations, the vertical resolution of HALOE NO profiles is only 4 km below 60 km and degrades further to 7 km at lower altitudes.

It is especially interesting, that this instrument uses a different spectral region for NO_2 retrieval compared to the SCIATRAN retrievals described here (infrared instead of the visible region).

2.5.3 ACE-FTS

One of the two main instruments aboard SCISAT-1, a Canadian satellite launched in August 2003, is ACE-FTS (Atmospheric Chemistry Experiment-Fourier Transform

Spectrometer, Bernath *et al.*, 2005; Walker *et al.*, 2005). Still operational in 2011, ACE-FTS allows the validation of more recent results compared to SAGE II and HALOE. The vertical resolution of the measurements is about 3 to 4 km, based on the field of view of the ACE-FTS instrument (1.25 mrad).

ACE-FTS is capable of investigating a large number of atmospheric trace gases including H_2O, O_3, N_2O, CO, CH_4, NO, NO_2, HNO_3, HF, HCl, N_2O_5, $ClONO_2$, CCl_2F_2, CCl_3F, COF_2, CHF_2Cl, HDO, SF_6, OCS, HCN, CF_4, CH_3Cl, C_2H_2, C_2H_6, N_2, ClO, as well as isotopologues for some of these molecules. For NO_2, a vertical range from 13 to 45 km is covered in version 2.2 ACE-FTS data used for this study, see Boone *et al.* (2005). A newer version (3.0) might provide a wider altitude range in the future, but was still under development at the course of this work.

The data product includes uncertainties given by statistical fitting errors from the least-squares process, see Kerzenmacher *et al.* (2008). A normal distribution of errors was assumed for these calculation. For most profiles these error values are less than 5% between 20 and 40 km. Below 20 km they are higher than 10% and exceed 40% at about 15 km.

2.5.4 Balloon-borne measurements

Obtaining data for validation of Earth-observing satellite missions is one of the important objectives of balloon-borne measurements. Despite the advantage, that each individual balloon campaign is less expensive than a satellite mission, only a limited number of profiles can be generated this way. Still, each profile is expected to be of good quality.

The balloon mission results used here are also the basis for a validation in Butz *et al.* (2006) for an older version of SCIATRAN/SCIAMACHY NO_2 and O_3 results. The launch sites and the measurement season were selected foresightfully to allow validation of ENVISAT. Details for the individual balloon missions are shown in Table 4.6. Results from these missions are used for validation in section 4.1.2.

The instruments are described in detail by Ferlemann *et al.* (1998) and Camy-Peyret (1995). The payload is mounted on an azimuth-controlled gondola and comprises a sun-tracker. Almost the entire wavelength range from the UV to mid-IR is covered using three optical spectrometers. The instrument setup is optimized in such a way, that the instruments for UV/visible (DOAS) and IR (Limb Profile Monitor of the Atmosphere/LPMA, Fourier Transform Spectrometer/FT-IR) analyze direct sunlight, which passed through almost the same atmospheric air masses. Measurements are performed in solar occultation and during both balloon ascent and descent. Also, since 2002 a small UV/visible limb spectrometer measuring scattered solar light has been added to the gondola.

The retrieval of O_3 and NO_2 profiles consists of two steps. First of all, trace gas concentrations integrated along the line-of-sight are obtained (SCDs). For the DOAS instrument the NO_2 absorption is obtained from the 435 to 485 nm spectral region. Using a solar reference spectrum, solar Fraunhofer lines are removed. Broad band spectral features are treated with a fourth order polynomial. The pressure dependence is low, but the temperature dependence of NO_2 absorption cross section was considered in the retrieval.

For the retrieval of NO_2 with the LPMA/FT-IR instrument, the spectral window from 2914.36 cm^{-1} to 2915.16 cm^{-1} is used. Weak absorption of NO_2 in the HCl window (2944.71 to 2945.11 cm^{-1}) helps to improve the retrieval of the NO_2 SCDs. Based on HITRAN 2004 absorption line parameters (see Rothman *et al.* (2005)) and an a priori guess for the trace gas profiles, similar to other approaches described in this work, synthetic spectra are calculated. These are fitted to the measured spectra using a non-linear Levenberg-Marquardt algorithm. Also several fitting parameters are applied including a third order polynomial, a zero order wavelength-shift and parameters to adjust the instrumental line shape.

Based on the slant column densities (SCD) from either the DOAS or the LPMA the inverse problem has to be solved in the second step:

$$\boldsymbol{y} = \mathbf{K}\boldsymbol{x} + \varepsilon. \tag{2.46}$$

$\boldsymbol{y}$ is the set of SCDs in this case, $\boldsymbol{x}$ is the true trace gas profile, ε is the measurement error of the balloonborne instrument and $\boldsymbol{K}$ is a weighting function matrix with elements K_{ij}. A spherical layered atmosphere is assumed and the elements K_{ij} are given by the ratio of the slant path through layer j and the height of layer j for the observation geometry, in which spectrum i was determined. To solve equation 2.46 the linear maximum a posteriori approach was used, see Rodgers (2000).

$$\hat{\boldsymbol{x}} = (\mathbf{K}^T\mathbf{S}_\varepsilon^{-1}\mathbf{K} + \mathbf{S}_a^{-1})^{-1}(\mathbf{K}^T\mathbf{S}_\varepsilon^{-1}\boldsymbol{y} + \mathbf{S}_a^{-1}\boldsymbol{x}_a) \tag{2.47}$$

$\mathbf{S}_a$ is the a priori and $\mathbf{S}_\varepsilon$ the measurement covariance matrix which are assumed to be diagonal. $\hat{x}$ is the retrieved trace gas profile.

Regarding comparison or validation purposes two additional points are important. First of all, the quality of the retrieval can be investigated by using the averaging kernel matrix $\mathbf{A}$. With x_a as the a priori profile and x as the true trace gas profile $\mathbf{A}$ can be written as

$$\hat{x} = x_a + \mathbf{A} * (\hat{x} - x_a) + \text{error terms}, \tag{2.48}$$

and for the maximum a posteriori approach as

$$\mathbf{A} = \hat{\mathbf{S}}\mathbf{K}^T\mathbf{S}_\varepsilon^{-1}\mathbf{K} \tag{2.49}$$

Secondly, for a meaningful validation the different vertical resolutions need to be considered. This can be done by smoothing, thus purposely lowering the vertical resolution of the high resolution measurement. Along with the photochemical corrections, this smoothing is performed on the balloon profiles used in section 4.1.2. The smoothed trace gas profile $\hat{x}_s$ is given by

$$\hat{x}_s = x_a + \mathbf{A}_l(\hat{x}_h - x_a). \tag{2.50}$$

$\mathbf{A}_l$ is the averaging kernel matrix of the lower resolution measurement, while the trace gas profile $\hat{x}_h$ is the retrieval result from the high resolution measurement.

2.5.5 Airborne measurements: SPURT and CARIBIC

Since one of the NO_2 sources in the upper troposphere/lower stratosphere region is airplane emissions (see section 2.1), instruments which are directly mounted to airplanes are quite valuable for validation purposes. Also, they provide in situ measurements. For validation, data sets from two airplane based instruments are available, called SPURT and CARIBIC.

One important difference between SPURT and CARIBIC are the airplanes, which carry the instruments. For SPURT, a small airplane is used as a platform and the SPURT crew can decide where to take measurements. CARIBIC is flown with a regular passenger plane and thus follows typical flight routes.

SPURT (German: Spurenstofftransport in der Tropopausenregion, trace gas transport in the tropopause region) measures a wide range of trace gases in the upper troposphere and the lowermost stratosphere of the Northern Hemisphere. It consists of a large array of in situ instruments, deployed on a Learjet 35a, flying up to 13.7 km, see Engel *et al.* (2006). For a total of 36 flights in eight campaigns, measurements were performed for N_2O, CH_4, CO, CO_2, CFC12, H_2, SF_6, NO, NO_y, O_3 and H_2O. SPURT has the minor disadvantage, that it doesn't measure NO_2 directly, but it measures NO. Thus, the NO has to be converted to NO_2 results by photochemical model calculations.

CARIBIC (Civil Aircraft for the regular investigation of the atmosphere based on an instrumented container, Brenninkmeijer *et al.*, 2007) follows a different concept. Originally, it consisted of an aircraft container with automated instruments on board a Boeing 767-300 R of LTU International Airways during 1997 to 2002. Subsequently an improved version of the container was built and installed on a Lufthansa Airbus A340-600 long-range aircraft, with first flights in 2004. Only the latter one is of interest for validation in the present study, since ENVISAT has been launched in March 2002. In Fig. 2.15 CARIBIC flight routes are shown.

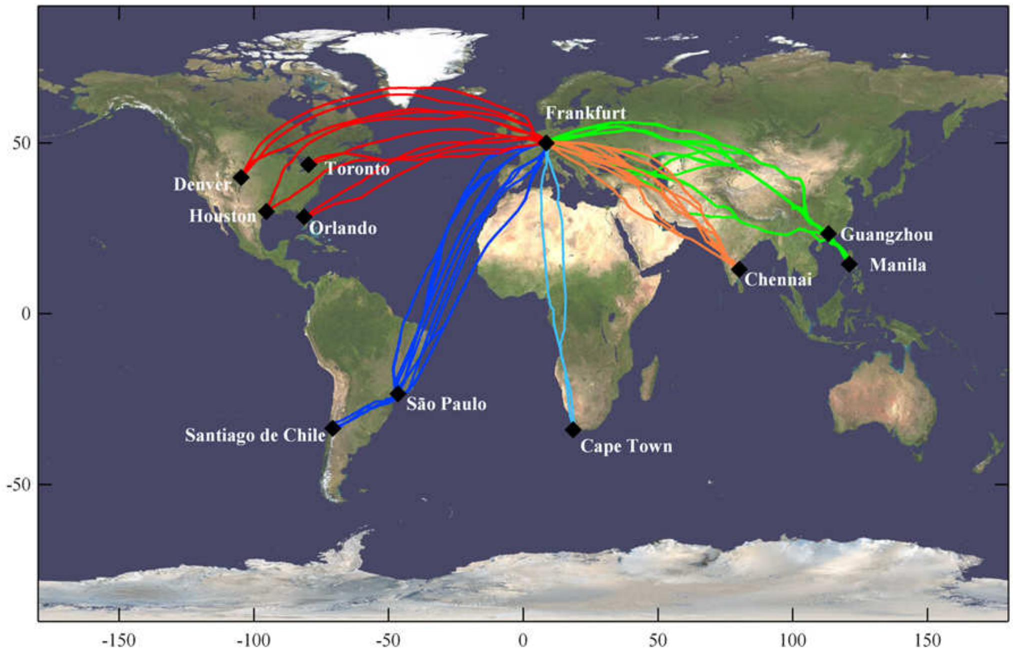

Figure 2.15: Shown here are some of the flight routes during the CARIBIC campaign. As the CARIBIC container is mounted on an airplane with passenger transport as its main purpose, its flight routes cannot be changed. Source for satellite image: NASA Earth Observatory. From Brenninkmeijer (2012)

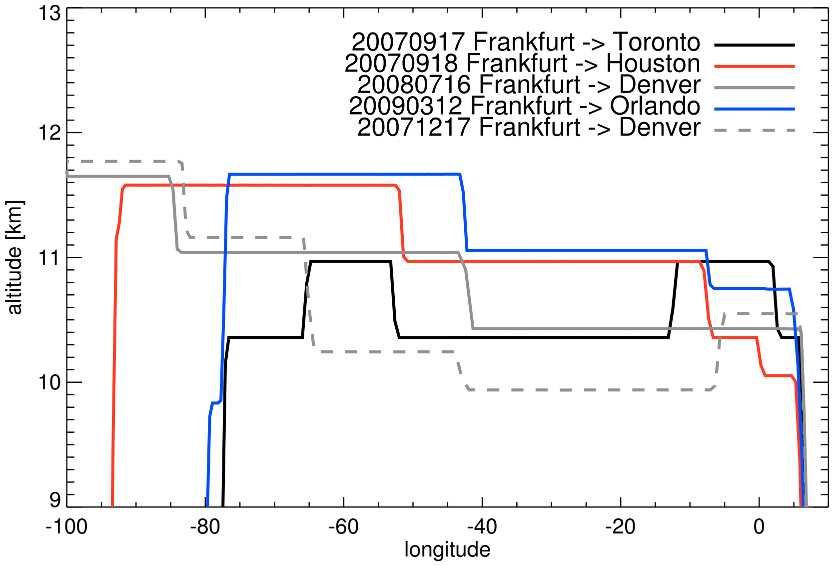

Figure 2.16: For a selection of CARIBIC flights, the recorded altitude is shown here depending on the longitude. All flights are going from East to West.

Using an inlet system, CARIBIC performs in situ measurements of O_3, total and gaseous H_2O, NO and NO_y, CO, CO_2, O_2, Hg, and number concentrations of submicrometer particles (> 4 nm, > 12 nm, and > 18 nm diameter). Among other devices, there are also three internal DOAS instruments added on the inlet system, which allow the detection of atmospheric trace gases such as BrO, HONO and NO_2. Due to the nature of these measurement campaigns vertical profiles are not produced, but longitudinal comparisons are possible.

The CARIBIC flight recordings also contain the flight altitude. Depending on the flight direction, the altitude on flights between Europe and North America varies strongly. The altitude is shown as a function of the longitude for a selection of flights over the North Atlantic from East to West in Fig. 2.16 and from West to East in Fig. 2.17. A qualitative impression of the latitudes during these flights can be seen in Fig. 2.15.

2.5.6 Climate model EMAC

Model results from the global-coupled chemistry-transport model EMAC (ECHAM5/ MESSy Atmospheric Chemistry model) are used for calculation on the SPURT data (section 4.1.4) and for comparison purposes regarding case studies in section 4.3. EMAC

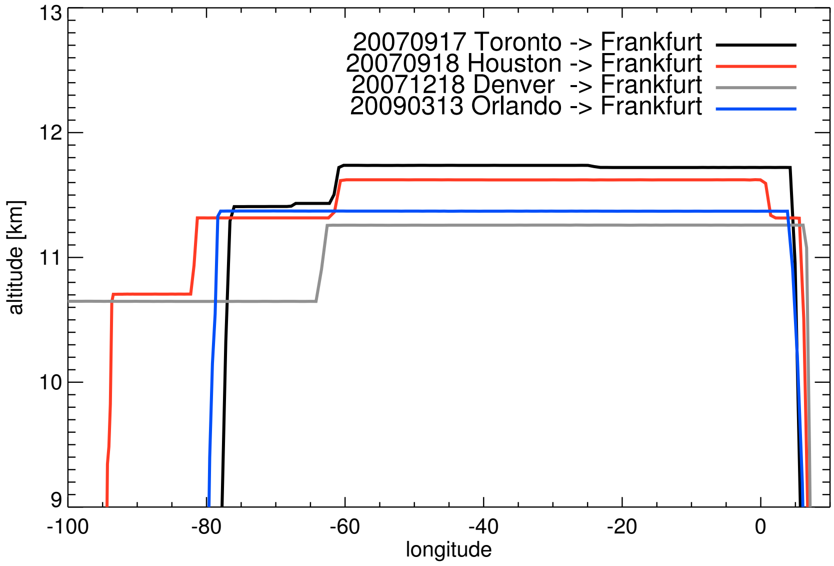

Figure 2.17: The flights shown here use the same routes as in Fig. 2.16. The flight direction is reversed, and only flights going from West to East are shown here.

is developed at the Max Planck Institute for Chemistry in Mainz, Germany, see Jöckel (2012); Jöckel *et al.* (2006).

The Modular Earth Submodel System (MESSy) describes atmospheric chemistry and meteorological processes and provides a modular framework. The ECHAM5 general circulation model (5th generation European Centre Hamburg GCM, Roeckner *et al.*, 2003, 2004) has been modified and coupled to MESSy. The MESSy framework contains a variety of submodels, each of them used for the simulation of a particular process, such as the calculation of, e.g. the radiative temperature tendencies.

The model setup features 90 layers up to 0.01 hPa. It should be noted, that altitudes in atmospheric models such as in EMAC are usually given as pressure levels and not in km, as the models are operating on a pressure level grid. The vertical resolution at the tropopause height is about 500 m and the horizontal resolution about 2.8° × 2.8°, see Jöckel *et al.* (2006).

The high vertical resolution was chosen to improve the results for the UTLS region. This is helpful with respect to advective transport, which is strongly height dependent and it also avoids numerical problems with steep gradients of some trace gases in certain regions.

Another feature is the possibility to switch off specific trace gas sources. In particular in section 4.3, the ability to simulate atmospheric composition with and without modelled NO_x emissions by airplanes is used.

3

Methods

3.1 SCIAMACHY NO_2 limb retrieval: sensitivity analysis and error sources

Although SCIAMACHY NO_2 results already include information on the theoretical precision, it is important to discuss some error sources individually. Instead of as a retrieval tool, SCIATRAN can also be used as a forward model, converting profiles and other atmospheric parameters into simulated spectra. Using a variety of simulated spectra with different atmospheric parameters, synthetic retrievals performed on these spectra provide an estimate how these parameters would influence the retrieval results in real measurements. This is done for clouds, aerosols and for pointing errors. Errors resulting from uncertainties in the pressure and temperature profiles have already been investigated in Rozanov *et al.* (2005). These are estimated to be less than 5% above 20 km, as accurate ECMWF measurements are included in the retrieval.

For the beginning, the sensitivity of the current retrieval processor is discussed for two examples, which also form the basis of the analysis in sections 3.1.1 to 3.1.3. The measurement details are described in Table 3.1, and SCIAMACHY NO_2 limb Version 3.1 retrieval results are displayed in panels (a) of Figures 3.1 and 3.2. Figure 3.1 represents a high latitude example and features a lower altitude maximum and a higher NO_2 amount compared with the example from the tropics shown in Figure 3.2.

In panel (b), values for the theoretical precision and the measurement response are shown. The former describe the total retrieval error (noise + smoothing errors). These

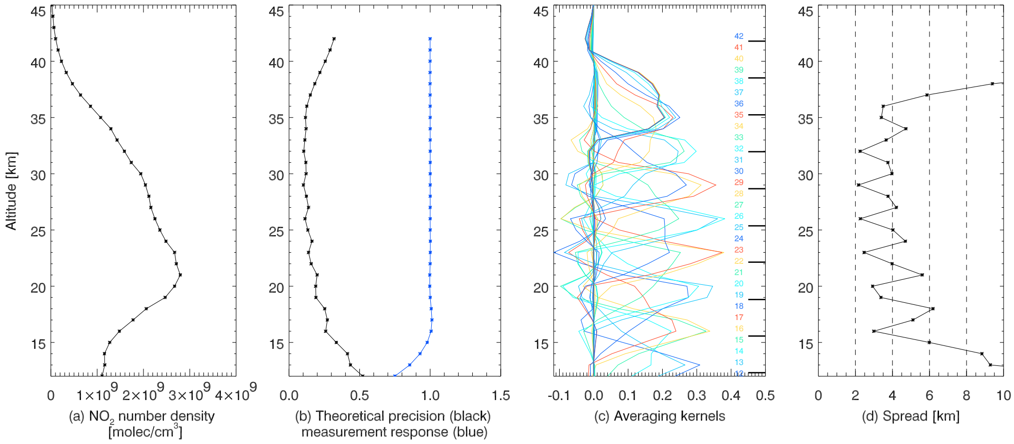

Figure 3.1: An example retrieval at about 77.5°N is analyzed to study the measurement sensitivity. The retrieved NO_2 profile is shown in panel (a). Panel (b) shows the theoretical precision (black), as well as the measurement response (blue). Panel (c) displays the respective averaging kernels, color coded for altitude levels. Panel (d) shows the spread of the averaging kernels.

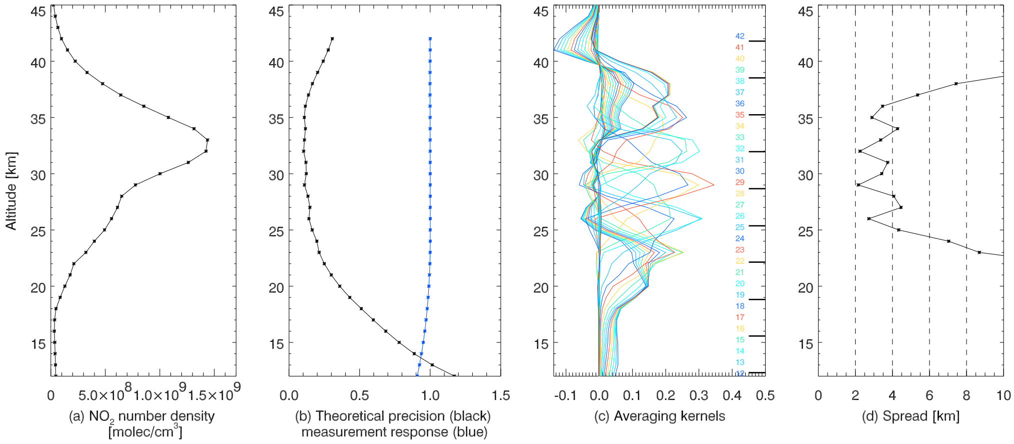

Figure 3.2: Same as in Fig. 3.2, but for a latitude of 1.45° N.

are provided with the V3.1 data product and calculated from the square root of the diagonal elements of the solution covariance matrix $\hat{\mathbf{S}}$, see also Rodgers (2000). $\hat{\mathbf{S}}$ is associated with the result $\hat{x}$ of the last iteration in the retrieval process and is defined as

$$\hat{\mathbf{S}} = \left(\hat{\mathbf{K}}^T \mathbf{S}_\epsilon^{-1} \hat{\mathbf{K}} + \mathbf{R}\right)^{-1}. \tag{3.1}$$

At lower altitudes, the precision is better (smaller values for high latitudes) than in the tropics, while there is no significant difference at higher altitudes, as seen in the examples here.

Also in panel (b), the measurement response is displayed, which is given by the area of the averaging kernels. It describes the relative contribution of the measurement and the a priori information on the retrieved profile. Values smaller than one indicate influence from the a priori information, which is not desired. The response is in both cases (Figures 3.1 and 3.2) close to one for altitudes above 20 km (tropics) or 15 km (high latitudes). In the tropics, NO_2 values at lower altitudes are low with 2.0×10^8 molec./cm^{-3} and the measurement response is about 0.9 below 20 km. In the high latitudes however, below 15 km an NO_2 amount of about 1.0×10^9 molec./cm^3 is seen. Nevertheless, the measurement response at low altitudes is smaller than in the tropics, which results from the altitude range of the given averaging kernels. The reason for this is that the averaging kernels are cut off at 12 km. At high latitudes, where averaging kernels still have large values below 12 km (see panel (c) of Figure 3.1), the truncation leads to an underestimation of the averaging kernel areas. In contrary, the cutoff has almost no effect in the tropics because the averaging kernel values below 12 km are negligibly small (see panel (c) of Figure 3.2).

The averaging kernels shown in panel (c) are calculated on a 1 km grid. As this grid is smaller than the resolution of the instrument (3.3 km), one must pay attention when analyzing these values. Due to the grid size, values between 0.3 and 0.4 indicate insignificant influence from a priori and no higher values are expected. In other studies, averaging kernels close to 1 are seen, which result from a retrieval method with a grid size similar to the resolution of the instrument. However, this does not indicate more accurate results. Furthermore, at about 43 km the averaging kernels are expected to be negative, as this altitude corresponds to the reference tangent height, see Figure 3.2.

The effective vertical resolution of the retrieved vertical NO_2 profile is difficult to estimate. In panels (d) of Figures 3.1 and 3.2, the vertical resolution of the retrieved profiles is estimated employing the Backus and Gilbert approach (Backus & Gilbert (1970), see Haley *et al.* (2004) for an application). This approach suggests a characteristics called spread which is given by

$$s(z) = 12 \frac{\int (z - z')^2 \mathbf{A}^2(z, z') dz'}{\left[\int |\mathbf{A}(z, z')| \, dz'\right]^2}. \tag{3.2}$$

Here, z is the altitude, and $\mathbf{A}$ denotes the averaging kernel matrix. The integration is performed with respect to all available altitudes z'. As expected, close to the actual tangent heights of the measurement, the spread shows the smallest values, which indicates a better vertical resolution there. In the tropics, only between 37 and 25 km good vertical resolution in the range of 2 to 6 km is seen. For the high latitudes, good vertical resolution is achieved for a larger altitude range from 15 to 37 km. Below 15 km (or 25 km in the tropics), the low signal resulting from low NO_2 values and an increasing optical light path along the line of sight lead to higher spread values and hence, a lower vertical resolution.

3.1.1 Influence of clouds on the NO_2 retrieval

On average, half of the Earth's surface is covered by clouds (page 85, Houghton, 2002). It is important for the retrieval of NO_2 in limb geometry to consider the influence of clouds on the results. Since the main focus of this work is to improve the sensitivity of NO_2 limb retrieval in the UTLS altitude region at about 10 to 12 km, cloud contamination is expected to be more severe than in the case of stratospheric NO_2 retrievals. Since SCIAMACHY has a vertical field-of-view of 2.5 km and a sampling of 3.3 km, clouds at 8 km or lower altitudes can already affect the results. Scattering is also an important factor.

The most straightforward solution to deal with this problem is not to consider those measurements where clouds are detected. A cloud detection algorithm (see section 2.3) is available, that is adapted for the same instrument and viewing geometry, so cloud-contaminated measurements are easily identified. The method of only using cloud-free scenarios is known as cloud-masking. SCIAMACHY NO_2 version 3.1 limb

Orbit	State nb.	Azimuth	time (UT)	Latitude	Longitude	SZA
17255	21	3 of 4	18-Jun-2005 13:01	1.2° N	44.1° E	35.7°
17255	08	2 of 4	18-Jun-2005 12:34	77.5° N	91.27° W	69.3°

Table 3.1: Selected states for cloud simulations. Latitudes, longitudes and solar zenith angles (SZA) are given at the tangent point of the measurement.

profiles already include cloud flags in the product files, while clouds are not considered in the retrieval processor.

Cloud-free scenes might be of limited availability due to large areas of the Earth being covered with clouds. Additionally, while limb geometry provides a good vertical resolution of about 3 km for SCIAMACHY, the horizontal resolution is about 240 km resulting in considerable difficulties in obtaining cloud-free measurements. This can lead to problems in finding suitable amounts of cloud-free measurements for averaging. Furthermore, lightning events occur in company with clouds, and airplanes usually produce a specific type of clouds called contrails.

Since cloud-masking can severely limit the number of available profiles, it is important to investigate how clouds actually change the retrieved NO_2 profiles. Based on a similar approach used in Sonkaew *et al.* (2009) for ozone retrievals, simulated cloud-contaminated spectra are used to investigate the influence of clouds.

Basically, cloud features are simulated in the forward model and synthetic spectra are calculated. These are based on NO_2 profiles from actual V3.1 retrievals. Two profiles serve as examples, one for the high latitudes and one for the tropics. Details about these two profiles are contained in Table 3.1.

In the present work the CDI/CDIPI radiative transfer model is used for NO_2 retrievals. For cloud simulations, however, this is not supported (Rozanov, 2007). Therefore, the discrete ordinate model ("DOM") is applied instead.

Using the DOM, simulated spectra are generated for two different solar zenith angles (35° and 70°), for two different cloud types (water clouds and ice clouds) and selected values of the cloud optical thickness τ. In addition, for both solar zenith angles (SZA) a cloud-free scenario has been simulated for comparison. Technically, identical NO_2 profiles for both SZAs can be used for this simulation. However, this would yield unrealistic results, as SZAs smaller than 40° do not occur in the high latitudes for SCIAMACHY measurements and because NO_2 profiles are typically different at high latitudes and the tropics. The same is true for SZAs larger than 70° in the tropics. Therefore, more realistic estimations are obtained with different NO_2 profiles.

The retrieval settings are set to be as similar as possible to SCIAMACHY NO_2 limb V3.1 retrieval settings. Correction spectra are not used in the synthetic retrieval, since e.g. Ring effects were not simulated in the forward model and thus do not need to be accounted for in the retrieval. Noise with a signal to noise ratio of 1000/1 is added to the signal.

Starting with a solar zenith angle of 35° in Fig. 3.3 the results show a reducing effect on the NO_2 values. Simulations were performed for four different τ values, of which two ($\tau = 1$ and $\tau = 20$) are shown. The retrieval difference in the righthand plots is given with respect to a retrieval of the cloud-free scene. A simulated cloud with a range from 5 to 7 km is marked with magenta, a cloud from 7 to 10 km with green, a cloud from 10 to 12 km with red, a cloud from 15 to 17 km with blue (dashed) and the 12 to 17 km cloud as grey (dashed). Clouds with different top height and thickness have a similar effect on the retrieved profile for this scenario, considering that the absolute values for NO_2 are small below 25 km. With the exception of 12 to 17 km all clouds with $\tau = 1$ result in less then 10% difference at all altitudes above 19 km. For the 12 to 17 km cloud, this is true above 22 km. For a cloud optical thickness $\tau = 20$, the influence of all simulated clouds is less than 10% above 22 km. At lower tangent heights this can exceed 60%, but still the absolute NO_2 values for this altitude and example are very low. It is worth mentioning, that even lower altitude clouds (7 to 10 km) have a noticeable effect for an altitude of up to 20 km. In the current implementation of the SCIAMACHY NO_2 retrieval processor, the lowermost altitude in the data files (11 km) can be flagged for lower altitude clouds (between 8 and 9 km), as the field of view (3.3 km) of the SCIAMACHY instrument is considered. However, clouds might still have a significant influence in cases where the cloud is several kilometers below the investigated altitude.

For ozone, an influence of clouds even outside the field of view of the instrument is seen (Sonkaew *et al.*, 2009). Therefore, an effect also on the retrieved NO_2 is expected. The simulations have also been repeated for ice clouds. The obtained results are similar to the water cloud case and thus they are not shown here.

The same simulations and synthetic retrievals have been performed for a similar case with a different solar zenith angle of about 70°. The resulting profiles can be

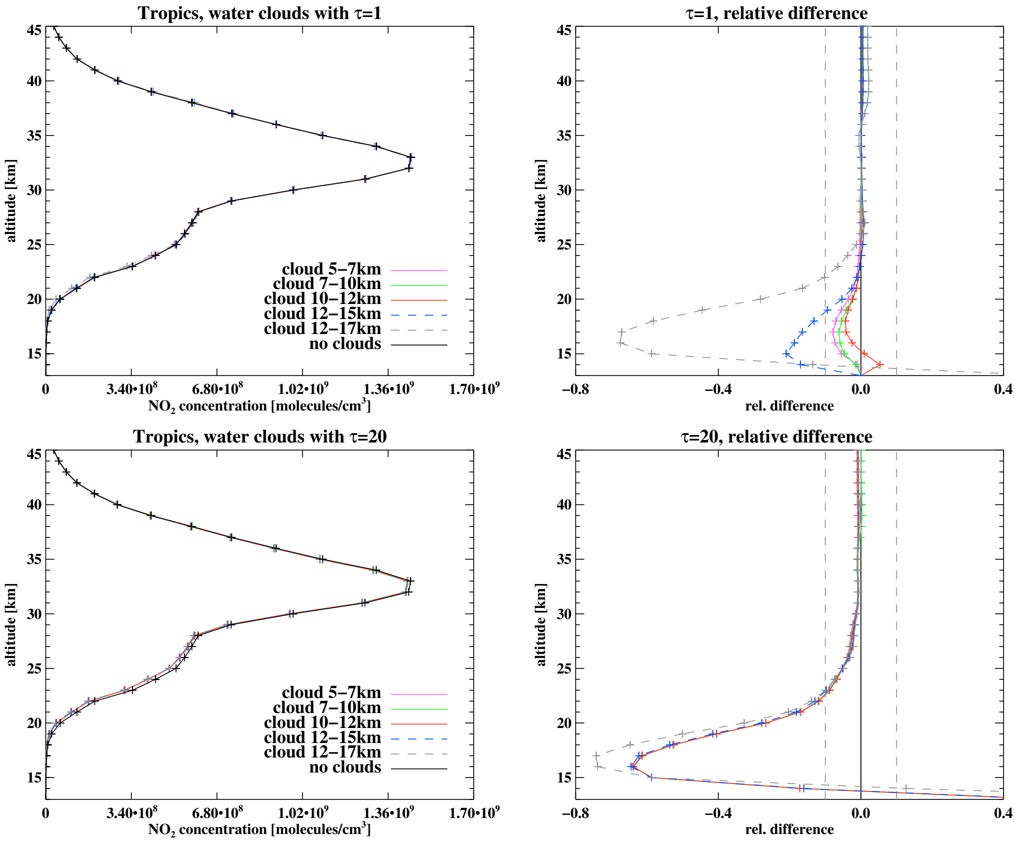

Figure 3.3: Influence of simulated water clouds on the NO_2 retrieval, solar zenith angle 35°.

seen in Fig. 3.4 for water clouds and Fig. 3.5 for ice clouds. Contrary to the SZA 35° results, in this case the relative differences between scenarios with and without clouds in the forward models are low and do not exceed 10% above 17 km for all simulated scenarios. At 13 km, only the 12 to 15 km cloud results in differences larger than 40%. However, clouds at this altitude are rarely observed in the high latitudes. Excluding this case, the difference is less than 5% for all simulated altitudes ($\tau = 1$), or less than 10% in the case of a cloud optical thickness of $\tau = 20$.

3.1.2 Influence of aerosols

Aerosols might also be an important error source for UTLS NO_2 retrievals. Gordley *et al.* (1996) even state that, for the occultation instrument HALOE, aerosol errors may render NO_2 retrievals at the lower stratosphere impossible. It is therefore very impor-

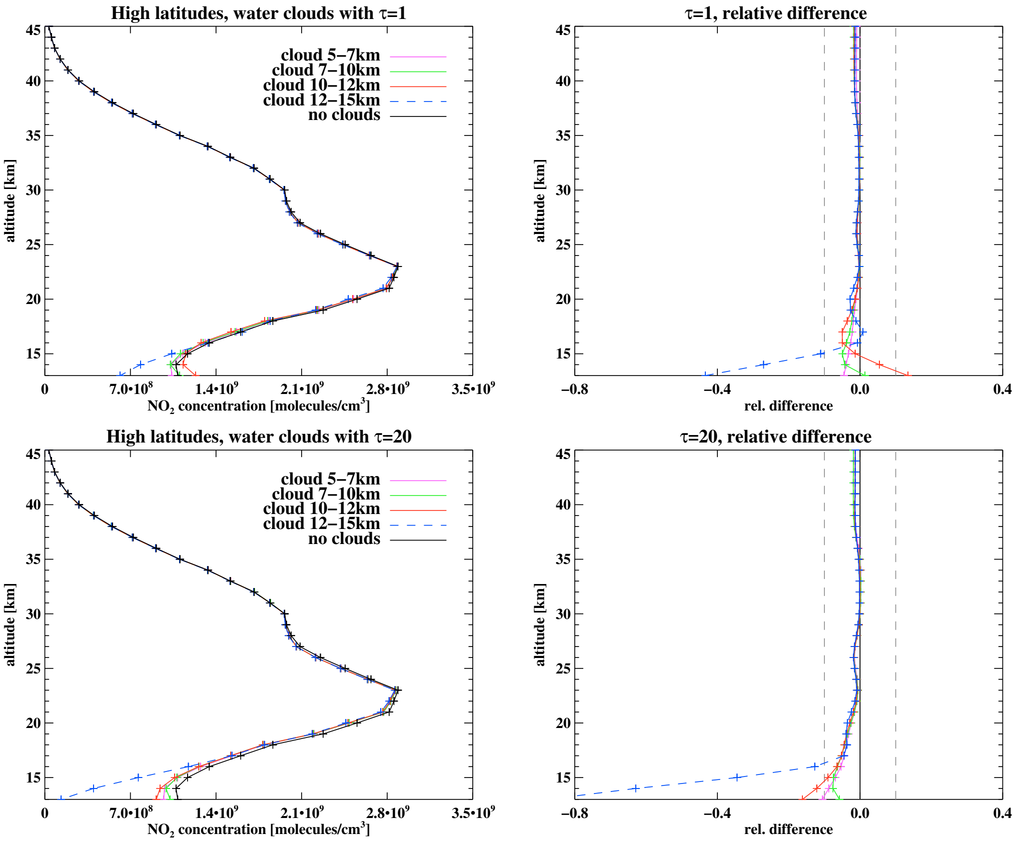

Figure 3.4: Influence of simulated water clouds on the NO_2 retrieval, solar zenith angle 70°.

tant to investigate how the presence of aerosols changes the retrieved NO_2 profiles. In the SCIAMACHY NO_2 V3.1 retrieval processor, background aerosols are already included. It is rather straightforward to simulate different aerosol scenarios based on these settings.

Based on LOWTRAN (Kneizys *et al.*, 2002), the scenarios 'no aerosols', 'aged aerosols from moderate volcanic activity' and 'fresh aerosols from high volcanic activity' are simulated for the two cases already used for the cloud simulations, see Table 3.1. Additionally, the 'background' aerosol scenario is simulated as a reference. Contrary to the cloud simulations, the CDI model can be used as the forward model, which eliminates one possible error source. In the synthetic retrieval settings, correction spectra are switched off and noise with a signal to noise ratio of 1000/1 is added.

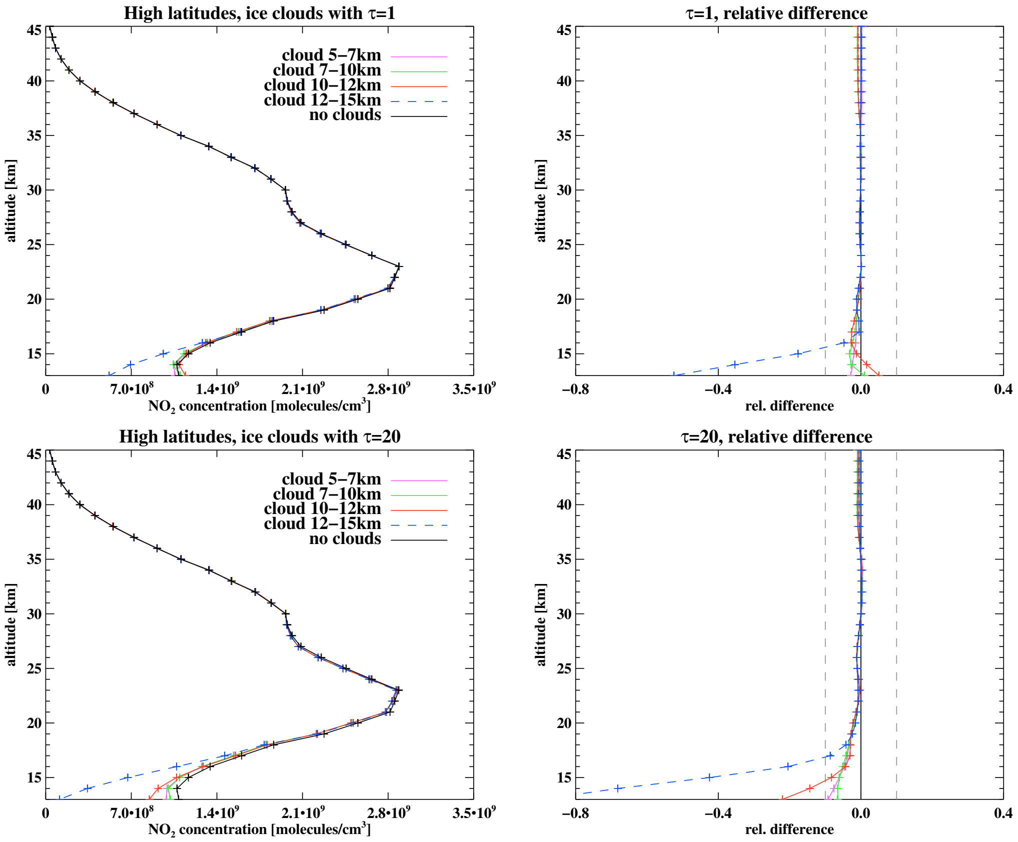

Figure 3.5: Influence of simulated ice clouds on the retrieval, solar zenith angle 70°.

The influence of these different aerosol scenarios on the retrieval outcome is summarized in Figure 3.6. While the unrealistic scenario with no aerosols in the forward model leads to increased NO$_2$, the two scenarios with volcanic aerosols result usually in less NO$_2$ in the profile. At high latitudes, the change in NO$_2$ is less than 5% above 23 km. Below this altitude at about 15 km, the relative difference can increase to 20% ('aged aerosols from moderate volcanic activity') or to more than 40% ('fresh aerosols from high volcanic activity'). In the tropics, above 24 km less than 10% difference from aerosols can be seen. Also, the two volcanic scenarios result in relative differences, that exceed 60% below 15 km. However, the absolute NO$_2$ values are small at these altitudes.

For profiles above 20 to 25 km, aerosols are not a large error source. Aerosols are more important for the UTLS, but as there is comparably low volcanic activity in the

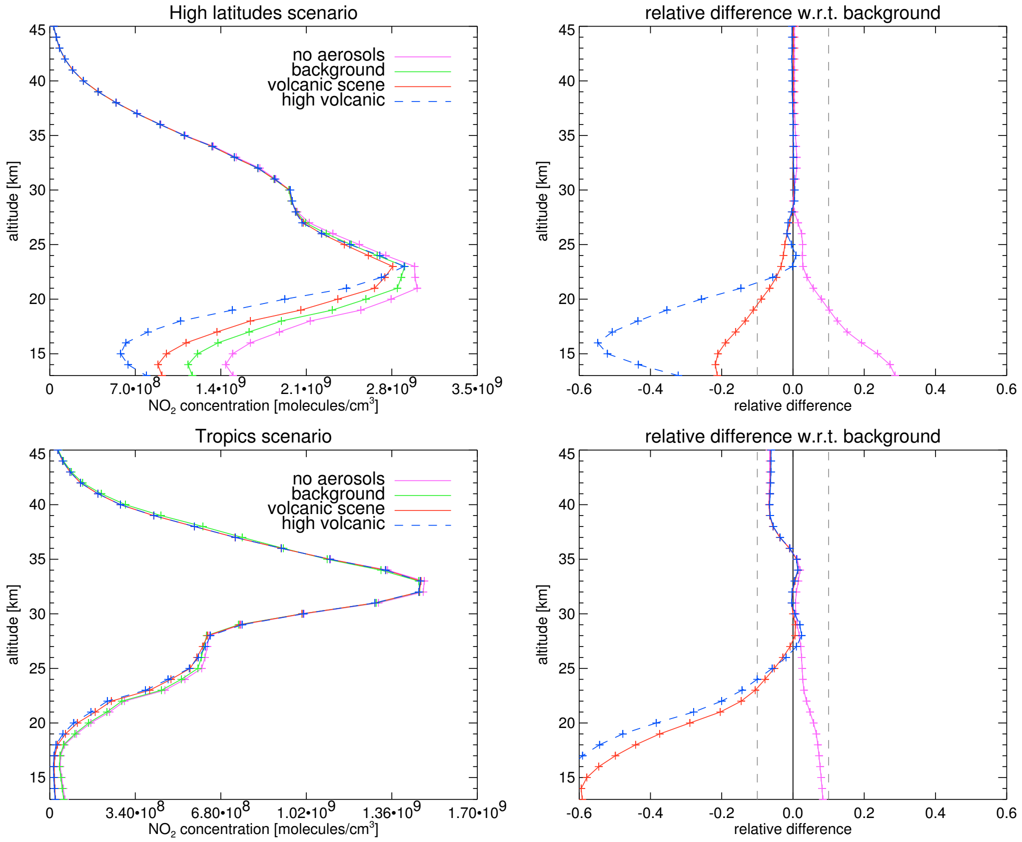

Figure 3.6: The upper panel shows the influence of aerosols on the retrieved NO_2 profile for the high latitudes, while the lower panel does the same for the tropics. In the left panels synthetic retrieved NO_2 profiles for different aerosol loadings are seen, while the right panels show the corresponding relative deviations.

investigated time frame and regions, errors from these aerosol should not affect the results.

3.1.3 Influence of pointing uncertainties

Another error source results from the uncertainty in the tangent height altitudes of the limb measurements. As of SCIAMACHY level 1 data version 6.03, this error is estimated to be less than ±200 m (von Savigny *et al.*, 2009), see also von Savigny *et al.* (2007). How a shifted tangent height influences the retrieval result, can be investigated with the same method as in sections 3.1.1 and 3.1.2. The tangent height altitudes in the forward model are shifted by 200 m up and down.

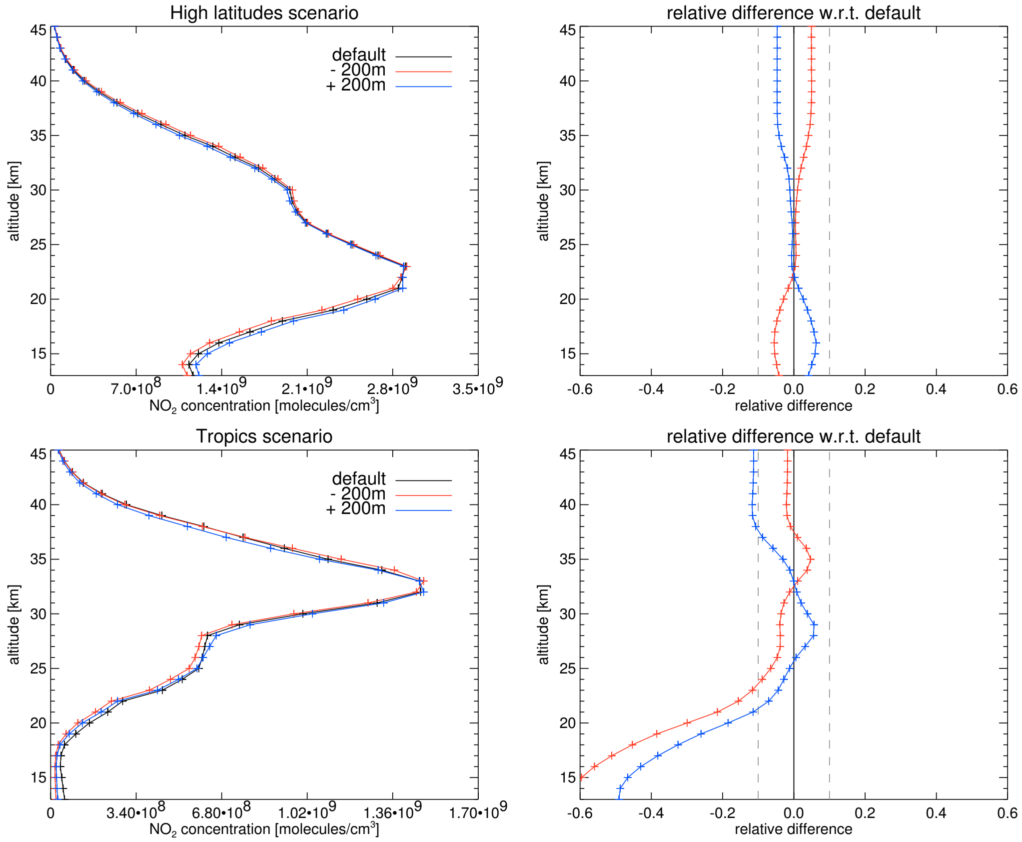

Figure 3.7: In this figure, the influence of pointing errors on the retrieval results is shown for high latitudes (upper panels) and tropics (lower panels). In both left panels, profiles for shifted (±200 m) and unperturbed default tangent heights are shown. The relative deviations (with respect to the unperturbed profile) are shown in the right panels.

The results of the synthetic retrievals on these simulated spectra are shown in Figure 3.7. In the high latitude case, the shift in tangent height results in a relative difference in the retrieved NO_2 amounts of up to 5%, even at low altitudes below 15 km. For the tropics, the relative difference can exceed 50% at 15 km. However, the NO_2 is low in absolute numbers at this altitude levels for the tropics. Hence, the relative errors should be read with care. Generally, due to improvements in pointing accuracy, this error source has a minor impact on UTLS retrievals compared to other error sources and former versions with larger pointing errors.

3.2 Validation of NO_2 retrievals

As discussed in section 2.1, NO_2 is a photochemically highly active species and has a pronounced diurnal cycle. This causes additional difficulties for validation activities. Two measurements that are to be compared might have a reasonably small spatial distance, so a small difference in NO_2 could be expected. However, if when they are performed at different local times (and thus, different SZAs), the retrieved NO_2 concentrations are not directly comparable. One of the two profiles has to be *photochemically corrected* to allow a comparison with the other profile.

For this task a program code has been created which uses model simulations to perform these photochemical corrections. A similar approach has been used by Butz *et al.* (2006). A detailed discussion of the photochemical correction method and associated errors is presented by Bracher *et al.* (2005). This approach has been used for the correction of the balloon borne measurements discussed in section 4.1.2.

A flowchart of the photochemical correction method is given in Fig. 3.8. At first, the two NO_2 data sources are opened as described in the given configuration file. As the goal is to compare different data sources with SCIATRAN results, the photochemical correction is performed on the external data source. This is named data set 1, while the SCIATRAN results are referred to as data set 2.

Depending on the data source given (e.g. balloon data) a subprogram opens the given data file and reads the necessary information. Especially coordinates, UT time and SZA are read. If the data source provides it, additional information (O_3 vertical profile, pressure, temperature) is also used. The next aim is to perform photochemical calculations, but the model (TOMCAT/SLIMCAT based, Chipperfield, 2006) needs more information for that purpose. A complete set of profiles for the simulated gaseous species is needed.

Therefore, precalculated model results from a 2D model (based on the THIN air model, Kinnersley, 1996) are used. The 2D model has the dimensions of altitude (in pressure levels) and latitude. Precalculated model profiles are interpolated to the geolocation of data set 2. Depending on the program settings, pressure, temperature and ozone profiles are replaced by profiles from data set 1. The original approach was to use the geolocation of data set 1 for the calculations, but this has one major disadvantage: The difference in position of both measurements has an influence on the SZA at

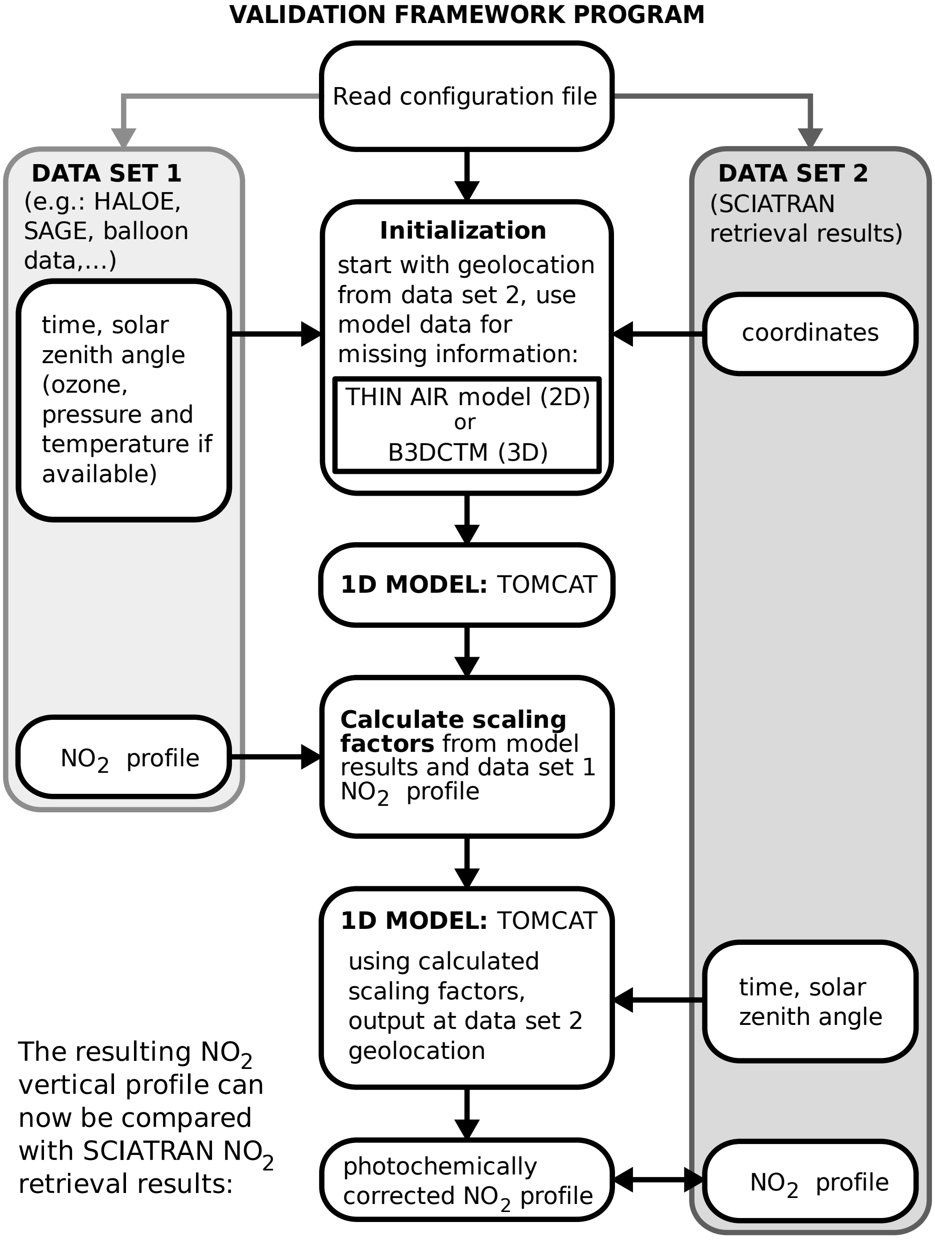

Figure 3.8: Outline of the validation algorithm used for photochemical corrections of NO_2 profiles. Basically a profile from a selected source (data set 1) will be corrected to allow comparisons with SCIAMACHY/SCIATRAN NO_2 vertical profiles.

a given time. In certain cases it is possible (as seen in balloon measurements), that the SZA of the SCIAMACHY measurement (data set 2) does not occur during the simulated day at the geolocation of data set 1. As most validation sources are occultation measurements, the SZA is usually about 90°, which is seen from most geolocations during a day. Therefore, the geolocation of data set 2 is selected.

With these settings, the 1D model (based on TOMCAT) is started and runs for the model time of two days. The one dimension (1D) is the altitude in km or pressure levels. The simulation time is needed for the model to stabilize. At the measurement time or SZA from data set 1 the calculation is stopped. By comparing the NO_2 vertical profiles from the 1D model results and the data set 1 NO_2 vertical profile scaling factors F are calculated.

With these scaling factors F (and all other settings unchanged) the model NO_2 is scaled to the data set 1 NO_2 vertical profile. As NO_2 is highly reactive (see section 2.1) other trace gases, which are linked through reactions, are also scaled with the same scaling factors F. These trace gases are NO, nitrate radicals (NO_3), dinitrogen pentoxide (N_2O_5), nitric acid (HNO_3) and hydroxy nitrate (HNO_4). With these changes the 1D model is run again for two days of simulated time.

At time and SZA of data set 2 the model is stopped and the modelled NO_2 profiles are used for comparison with the data set 2 results.

There is one limitation in this concept, which is encountered at the tropopause height. The precalculated model data is of lesser quality for the troposphere and the 1D model is not optimized either for this altitude region. Therefore, the accuracy of the photochemical corrections below the tropopause height might be poor. As NO_2 limb measurements are less sensitive for the lower troposphere, this is not a problem for validation at the moment. It must be, however, considered for the UTLS region. Above the tropopause the approach of a photochemical correction is of valualable and it is suitable for validations.

The validation program code is of modular design to allow the investigation of different data sources or initialization models. For example, a more sophisticated 3D model (B3DCTM, Wieters *et al.*, 2009) could be used instead of the 2D model. The additional dimension is the longitude, i.e. longitudinal variations can be accounted for this alternative model. Furthermore, different validation data sources (e.g., the satellite instruments HALOE, ACE-FTS, and SAGE II) can be utilized.

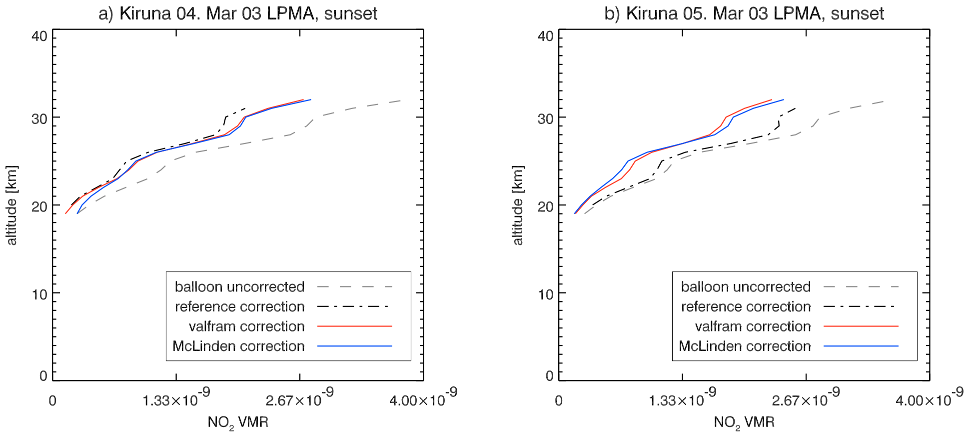

Figure 3.9: A comparison for different photochemical corrections is shown for one balloon borne measurement and two SCIAMACHY based geolocations as seen in Table 4.6. The photochemical correction described in the present work is marked as 'valfram'

3.2.1 Accuracy of the photochemical correction

To investigate the performance of the validation program, the balloon measurements from Butz *et al.* (2006) are photochemically corrected and compared with results from a different approach. The comparisons are shown in Figures 3.9 and 3.10. The uncorrected balloon measurements are shown as grey and dashed lines, while photochemically corrected (see section 2.5.4) balloon measurements using the approach from Butz *et al.* (2006) are depicted as black and dash-dotted lines. Results from the validation approach described here are shown in red. Chris McLinden (Air Quality Research Division, Environmental Canada, Toronto, Ontario, Canada) has also provided a set of photochemically corrected profiles for these balloon data sets, using the University of California, Irvine, photochemical box model (McLinden *et al.*, 2000; Prather, 1992). Results from the McLinden approach are shown in blue. Of these three methods, smoothing is only applied for the approach from Butz *et al.* (2006).

In most cases, the results are very similar with a difference less than 20%. For very low NO$_2$ values larger differences than 20% are seen, but in those cases a discussion of the relative quality is less suitable. There is one case, in which both the validation program results and the corrections from Chris McLinden are very different compared to the reference correction from Butz *et al.* (2006). This case is shown in Fig. 3.9, panel (b). Since this plot refers to air masses which are only coincident for a range of just

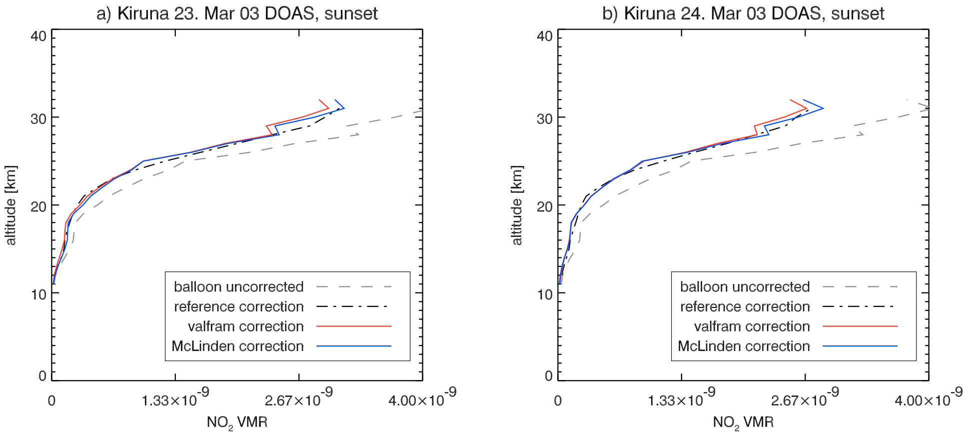

Figure 3.10: A similar comparison as in Fig. 3.9 is shown for another balloon measurement.

1 km, it is not considered for the validation in section 4.1.2.

For a validation using numerous solar occultation measurements, it appears that the photochemically corrected NO_2 values are over-corrected (i.e. too low) at altitudes between 30 and 40 km. This becomes prominent, when the SZA of the SCIAMACHY instrument is small, for example around 30°. The agreement of SCIAMACHY and any occultation instrument investigated becomes worse at altitudes higher than 20 km in the tropics (where SCIAMACHY SZAs are low) without a physical reason. As an anti-correlation between the SZA and differences between the SCIAMACHY NO_2 profiles and the photochemically corrected NO_2 profile from the solar occultation instrument is seen, a comparison with a different model was necessary.

Using data from a photochemical box model provided by Chris McLinden the diurnal cycle from the validation algorithm and the box model model is compared for one scenario, see Fig. 3.11. Panel (a) shows the initial NO_2 profiles. The profile from the validation algorithm is less smooth in comparison, as it has been scaled to match the NO_2 profile measured from the balloon-borne instrument. From these profiles, the change in NO_2 is shown for three SZAs, namely for 87°, 62°, and 36° in panels (b), (c), and (d), respectively. The agreement between the two methods is best for panel (a), where the difference is only 3° in SZA. Despite a small difference in SZA, these NO_2 profiles are about 50% smaller than the profiles at 90° SZA - similar to all three panels. The reason for this is a very rapid change of NO_2 at sunrise/ sunset, i.e. around an

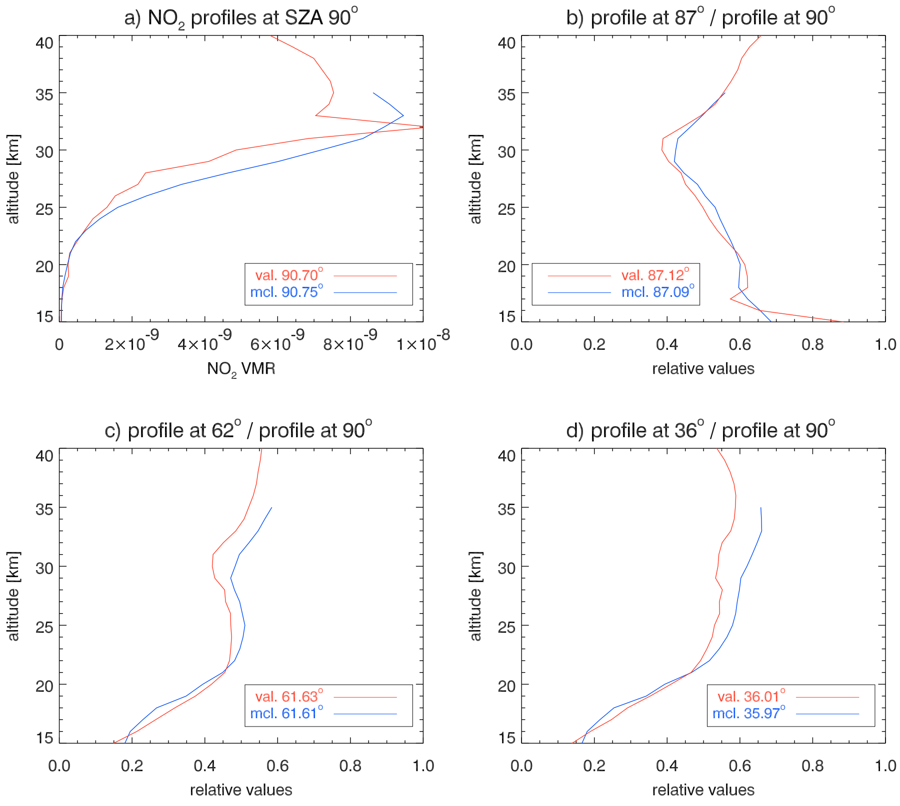

Figure 3.11: Difference in diurnal NO_2 changes calculated from the photochemical corrections described here (red) and a photochemical box model (blue).

SZA of 90°, see Figures 2.3 and 2.4. Although the three SZAs show profiles at similar orders of magnitude (in most cases in the range of 40 to 60% compared with the profile at an SZA of 90°) the difference between the two corrected profiles is largest at small SZAs. For this reason, the validation using the three different occultation satellite instruments is performed with a different approach than the one described above.

It is also important to pay attention to the volume mixing ratios (VMR), as most instruments investigated provide the NO_2 amounts in therms of number densities, while the models incorporated in the validation program calculate with VMR values. It is straightforward to convert VMRs to number densities N and vice versa, if the temperature T and the pressure p are known:

$$\mathrm{VMR}_{NO_2} = \mathrm{N}_{NO_2} * k_B * T * 10^6 / p \tag{3.3}$$

$$\mathrm{N}_{NO_2} = \mathrm{VMR}_{NO_2} * p / (k_B * T * 10^6), \tag{3.4}$$

where $k_B = 1.38 * 10^{-23}$ J/K is the Boltzmann constant. Although only a horizontal distance of up to several hundred km (exact value dependent on the validation source) is allowed between the two collocated measurements, variations of pressure and temperature or differences in the sources of these data sets (external databases, e.g. ECMWF) could influence the results. Therefore, once a conversion from number densities to VMRs is performed, the conversion back to number densities is always performed using the same pressure and temperature values.

Limitations at higher stratospheric altitudes (anticorrelation of SZA difference and difference between SCIA and photochemically corrected NO_2 profiles) lead to the usage of a different approach for the validation with solar occultation instruments. This is described in section 3.2.2. Still, the approach described above works reasonably well for balloon borne instruments and as a testing method for the improvement of NO_2 retrievals in the UTLS region. For these purposes the method is used in the present work.

3.2.2 Validation of limb NO_2 using solar occultation instruments

Three solar occultation satellite instruments are selected for a large number of comparisons, SAGE II, HALOE, and ACE-FTS. For a description of these instruments see sections 2.5.1 to 2.5.3. Here, the methods and criteria applied in the comparisons are described, i.e. the criteria for collocation, the method used for the photochemical correction and a method to estimate the so-called diurnal effect error explained later.

Collocation criteria

It is straightforward to apply the same criteria for collocation requirements to all three instruments. As a first step, for each collocation pair a maximum spatial difference of 500 km and a time difference of up to 8 hours is accepted. Secondly, only a difference of up to 2 km in the tropopause height is allowed. However, if both tropopause heights are estimated to be lower than 10 km, larger differences are accepted as well.

The tropopause heights are derived from ECMWF pressure and temperature profiles using the method described in Hoinka (1998). The tropopause heights are selected (as nearest neighbour) from a 1.5° × 1.5° grid (Felix Ebojie, personal communication, 2010).

Additionally, as in Bracher *et al.* (2004), collocation pairs are rejected, if they are not both inside or both outside the polar vortex, or basically if they are measured under different vortex conditions. To perform this discrimination, the potential vorticity (PV) is calculated. The PV is the absolute circulation of an air parcel, which is enclosed between two isentropic surfaces. On the order of days, the PV of an air parcel is conserved, if friction and diabatic heating are considered absent. Hence, the potential temperature difference between two isentropic surfaces of an air parcel is conserved along the parcel's directory. The potential temperature is defined as the temperature of an air parcel, if it is brought adiabatically to surface pressure conditions (about 1000 hPa). A commonly used unit for the potential vorticity is 1 PVU (potential vorticity unit), given as as $10^{-6}m^2Ks^{-1}kg^{-1}$.

This value, as stated in Houghton (2002), is also useful as a tracer of air motion, as the PVU is a conserved quantity. Software implemented by Sonkaew (2010) provides the necessary data, using the UKMO (United Kingdom Meteorological Office) assimilated meteorological data set (with a grid of 3.75° × 2.5°). As in Bracher *et al.* (2004), the collocation pair is accepted if the potential vorticities at the isentropic level of 475 K for both measurements are less than -40 PVU or higher than 40 PVU. The pair is are also accepted, if both potential vorticities are in the range from -30 to 30 PVU.

All these criteria are applied automatically, which allows the investigation of a large number of collocation pairs.

Photochemical correction method

As discussed in section 3.2.1, the method for the photochemical correction described in section 3.2 does not perform very well at altitudes between 30 km and 40 km. However, in a comparison with solar occultation instruments which does not focus exclusively on the UTLS altitude region, these altitudes are important. Therefore, a different approach was chosen and applied for the photochemical correction of solar occultation measurements.

Instead of individual model runs, a precalculated data set forms the basis of the method. For the 1st, 11th and 21st day of each month, a complete diurnal cycle of NO_2 profiles calculated with the chemical box model developed at the University of California, Irvine (McLinden *et al.*, 2000; Prather, 1992) is provided in a look-up-table. The latitude grid size is 2.5° and for a vertical step size of 2 km, each data set covers the range from 8 to 56 km. For each collocating pair of a SCIAMACHY NO_2 profile and a NO_2 profile from an occultation instrument, matching geolocations and SZAs are found in the look-up-table. Scaling factors are then determined by dividing the profile from the look-up-table at the SCIAMACHY SZA by the profile corresponding to the SZA of the occultation instrument. By multiplying the NO_2 values at each altitude with these scaling factors, the photochemical correction is applied.

Estimating the diurnal effect error

Most retrieval approaches assume a homogeneous atmosphere, i.e. the variation of the SZA along the light path is not considered, see McLinden *et al.* (2006). Depending on the measurement situation this can lead to significant errors, which is referred to as the diurnal effect error. Especially close to an SZA of 90° the concentration of NO_2 in the atmosphere changes most rapidly, see Figures 2.3 and 2.4.

For solar occultation instruments, the diurnal effect error can be estimated using simulated occultation retrievals provided by Chris McLinden. It was discussed in Brohede *et al.* (2007a), that this error is among other measurement circumstances subject to seasonal variation. Therefore, the error is estimated for each collocation pair in the satellite validation sets individually. Two data sets are provided with synthetic NO_2 profiles retrieved from simulated solar occultation instruments, one data set with the diurnal effect in the forward model $N_{diurnal}$ and one without $N_{nodiurnal}$. An estimated relative error $\epsilon_{diurnal}$ can be calculated:

$$\epsilon_{diurnal} = \frac{N_{diurnal} - N_{nodiurnal}}{N_{nodiurnal}}. \tag{3.5}$$

The diurnal effect error also affects limb measurements, depending on the SZA, as the SZA changes from measurement to measurement. For SZAs close to 90° the diurnal effect error is of similar magnitude as for the occultation instruments. For example in the tropics, where SZAs close to 30° are typical for SCIAMACHY measurements, a less rapidly changing NO_2 results in a far smaller diurnal effect error as it is the case

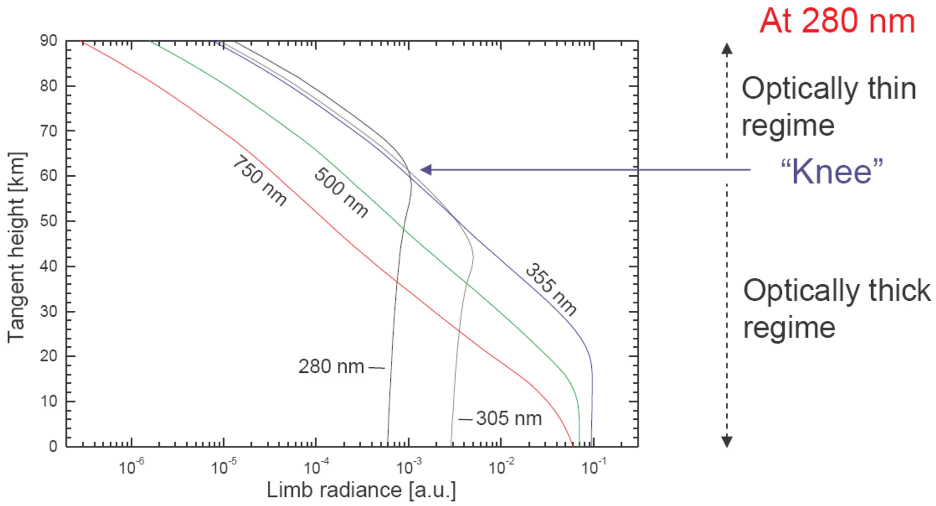

Figure 3.12: Modelled limb radiance profiles. Figure from Christian von Savigny (pers. communication).

for solar occultation measurements. Therefore, the influence of the diurnal effect on the validation efforts can be estimated for the tropics and mid latitudes, under the assumption that the diurnal effect error for SCIAMACHY limb observations is low. This cannot be assumed for high latitudes, due to the higher SZA values.

3.3 Improving the NO_2 limb retrieval in the UTLS region

Using SCIATRAN for NO_2 limb retrieval already provides profiles, which are reasonably validated and can be used for studies regarding the stratospheric altitude region. However, the sensitivity in limb geometry declines close towards the troposphere.

There are several problems rendering retrievals at the UTLS altitude region very difficult, for example the presence of a significant NO_2 maximum in most retrieved profiles at about 30 km altitude, i.e. above the investigated area. Another important aspect is that, depending on the wavelength, the atmosphere becomes optically thick for limb measurements at lower tangent heights, see Fig. 3.12. The wavelength window used for V3.1 limb NO_2 retrievals is 420 to 470 nm. At least below a tangent height of 10 km NO_2 detection will be extremely difficult if not impossible due to scattering processes.

To be more precise, sensitivity studies (Rozanov *et al.*, 2005) have shown, that at about 12 km altitude results regarding the NO_2 limb retrieval show a decline in averaging kernels and are also sensitive to changes in pressure and temperature information. Changing the a priori profile also has a significant effect at these altitudes, which also indicates a reduced sensitivity. Figure 3.13 shows as an example, how averaging kernels decline at lower tangent heights, which is seen more clearly in the left panel.

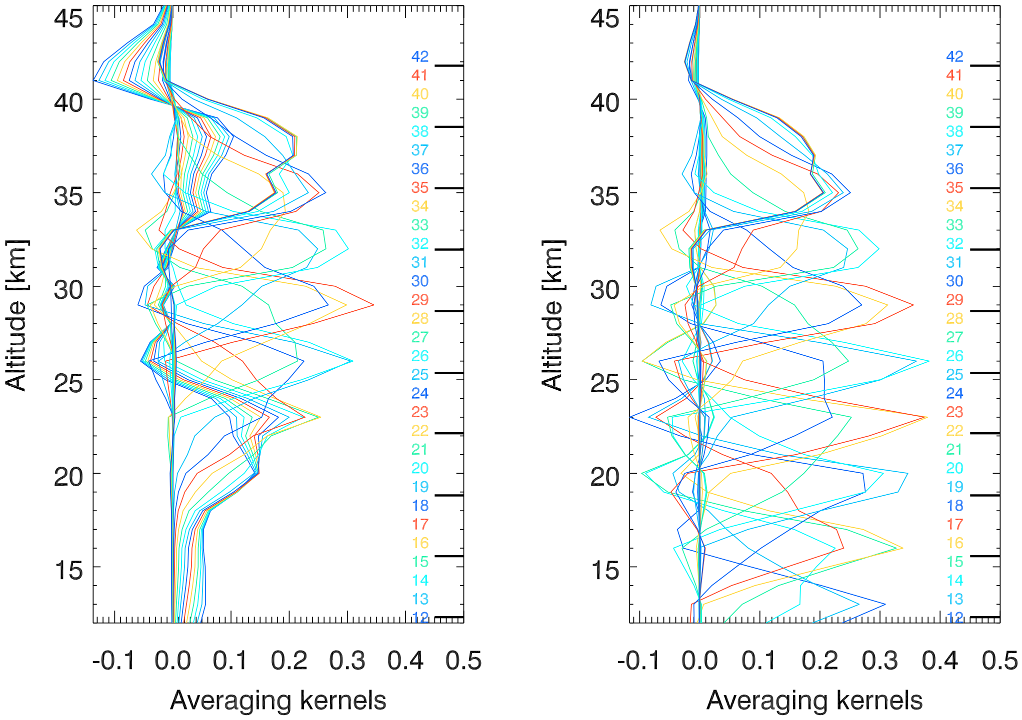

Figure 3.13: Example averaging kernels for SCIATRAN V3.1 retrieval for the tropics (left) and high latitudes (right), as seen in Figures 3.1 and 3.2. At lower altitudes averaging kernels are weaker, displaying lower sensitivity and a stronger influence of the a priori information.

It is however worth the effort to optimize the retrieval process for the UTLS region around 10 - 12 km for high latitudes. Even a small improvement in sensitivity justifies the effort, since in this altitude region interesting atmospheric processes of anthropogenic and natural origin can be investigated.

3.3.1 Sensitivity studies

In this section the possibility of detecting changes in NO_2 amounts in the UTLS region is investigated. The first aim is to obtain an estimate of expected enhancements in NO_2 amounts at these altitudes. This estimation is needed for the decision, if the achieved sensitivity is sufficient to allow a detection of increased NO_2. Based on results from Gauss *et al.* (2006) a maximum of 45 pptv increase in NO_2 is estimated for the case of NO_2 from airplane emissions in high-traffic flight corridors and this value is used as the basis for the sensitivity studies.

SCIATRAN works both as a retrieval algorithm and a forward model. Used as a forward model starting with given vertical profiles synthetic spectra are simulated. Those vertical profiles can be perturbed using the information above. Using the perturbed profiles in the forward model, results in different simulated spectra. A SCIATRAN retrieval can be performed on those spectra and the difference in the retrieved NO_2 profiles between the unperturbed and perturbed cases gives an estimate on the actual sensitivity.

A limitation of this approach is that it can only be as good as the knowledge about the atmosphere implemented in SCIATRAN. However, it provides a comparison, that can not be provided by in situ measurements. Two perfectly identical measurement scenarios would be needed, and the only difference should be the perturbation which is to be detected. In situ and other data sources are still extremely valuable, but rather for validation purposes as performed in section 4.1.

Four synthetic scenarios are used, each for a different month. The four months are January, April, July and October. After performing these retrievals the first step is to check how a perturbation at 11 to 12 km is expected to affect the retrieved profile. This is performed by a convolution of the averaging kernels with the high resolution perturbance:

$$\hat{\boldsymbol{x}} = \boldsymbol{x}_0 + \hat{\mathbf{A}}_k(\boldsymbol{x}_p - \boldsymbol{x}_0) \tag{3.6}$$

Here A_k are the averaging kernels, x_0 is the true profile and x_p is the perturbed profile. The profile information is given on a 1 km grid. The result can be seen in 3.14 for a synthetic perturbation of an increased NO_2 VMR by 45 ppt at 11 km and 12 km when using both, the 420 to 470 nm and the 520 to 560 nm spectral regions. The blue line shows the a priori profile, while the red line shows the selected perturbation. The

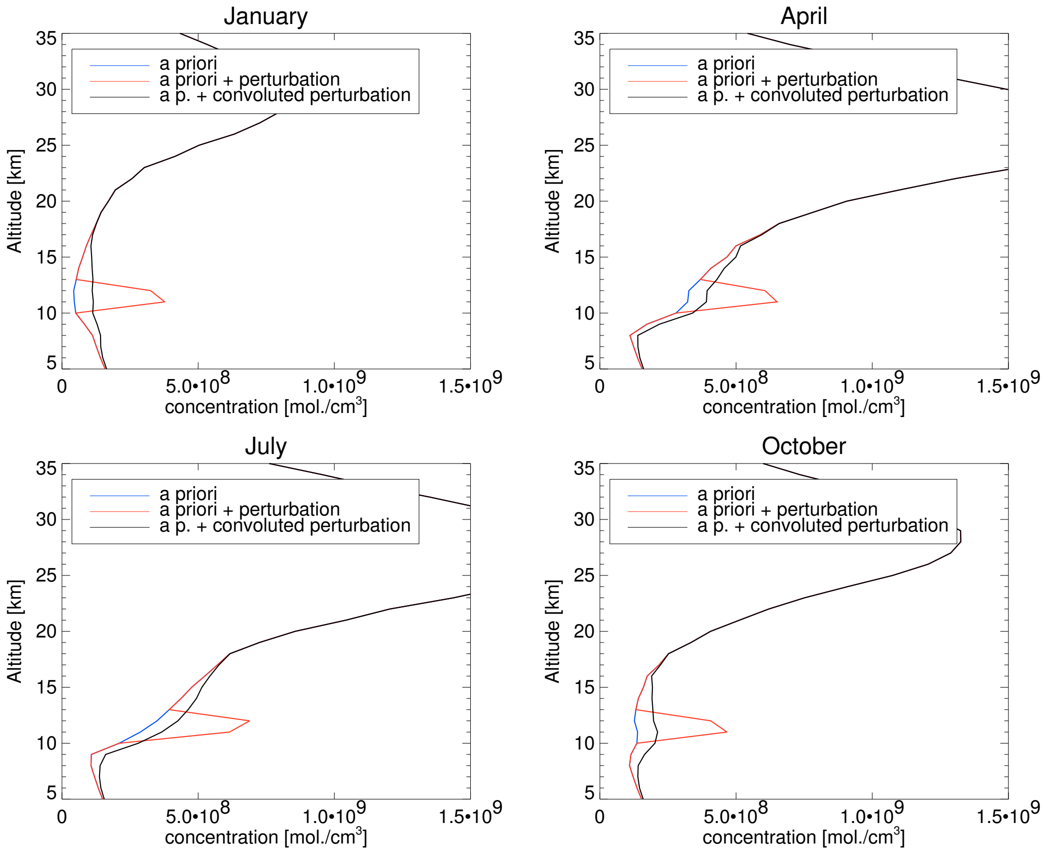

Figure 3.14: A synthetic perturbation in the NO_2 concentration of 45 ppt at 11 km and 12 km has been convoluted with averaging kernels for four scenarios. The averaging kernels are based on a retrieval using both, the 420 to 470 nm and 520 to 560 nm spectral regions.

convoluted profile resulting from equation 3.6 is marked in black. Mainly due to the resolution of the SCIAMACHY instrument the perturbation is smoothed considerably. As a consequence, even if an emission source produces more local NO_2 than needed judging from theoretical precisions, this smoothing effect has to be considered. A very localized peak may not be observed as a sharp peak in the resulting profiles. However, this does not mean that the retrieval is insensitive to NO_2 perturbations

The next step is the investigation of actual retrievals. The convolution approach in the last paragraph has one interesting advantage: It avoids retrieval artifacts. In synthetic retrievals (and even more, in real retrievals) artifacts can occur, e.g. poor convergence leading to surprisingly large peaks or unphysical results. The judgement

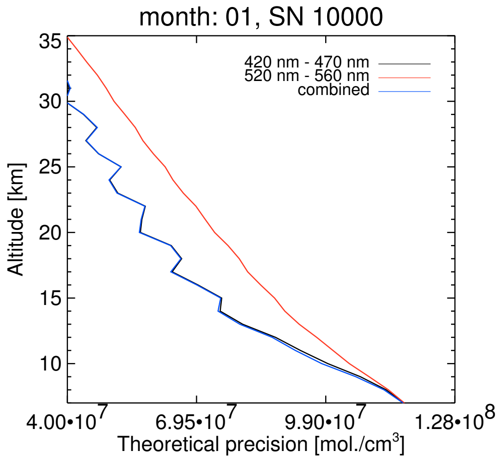

Figure 3.15: This figure shows theoretical precisions using different retrieval settings. The black line shows the results for the 420 to 470 nm spectral range, the red line for 520 to 560 nm and the blue line for both spectral windows combined.

if a large peak is not the result of a good set of retrieval settings, but rather a retrieval error, is very important for sensitivity studies and retrievals in general.

Investigation of theoretical precisions needs to be performed as well. Results seen in Fig. 3.15 show an interesting comparison of the three investigated settings regarding the spectral region. The 520 to 560 nm spectral region shows the worst theoretical precision, while the other two settings do not seem to differ significantly in their theoretical precisions. Although the difference to the 420 to 470 nm range is not large, the theoretical precisions for the combined setting show the best results.

Synthetic retrievals are performed using different spectral regions. Figures 3.16 to 3.17 all show a signal to noise ratio of 10,000. This value is however not reached by single SCIAMACHY measurements, but reflects the usage of a number of profiles for averaging, as it is performed in section 4.3. From the performed simulations, two scenarios are shown here: Figure 3.16 depicts the 'January' scenario and Figure 3.17 the 'October' scenario. In both cases, the three different spectral ranges were used for the retrievals, while all other settings remained unchanged if possible. The two graphs at the top are retrieved with a spectral range of 420 to 470 nm, the middle ones with 520 to 560 nm and the plots at the bottom with the combined spectral range 420 to 470 nm and 520 to 560 nm. The panels on the left show the NO$_2$ retrieval results, and on the right the averaging kernels are shown. The altitudes for the averaging kernels

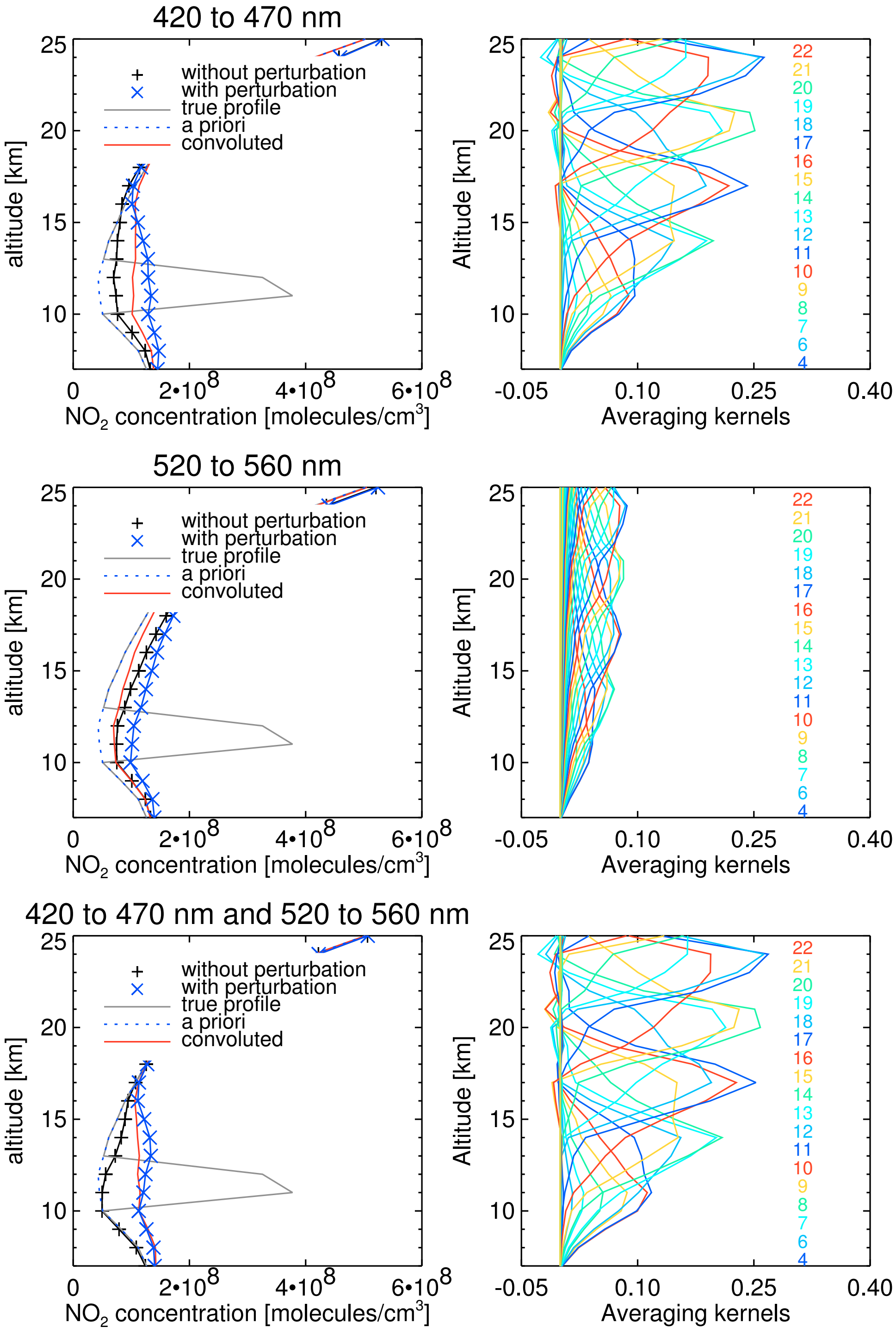

Figure 3.16: Synthetic retrievals for different spectral ranges simulated for a January scenario are shown.

are written as numbers in km in the same color. The black line in the left panels is the retrieval result for the unperturbed profile. The retrieved profile of the perturbed case is shown as blue, while the true, perturbed profile is seen as a grey line. The red curve is the convoluted true profile, i.e., the profile which is expected to be seen by the retrieval.

It can be easily seen from Fig. 3.15, that the 520 to 560 nm scenario provides the least useful results. The averaging kernels show, that the influence of the a priori is large and in addition the sensitivity is low. It can be concluded, that this spectral region alone is not very useful for this particular task. At least, the retrieval is not completely insensitive, there is a difference between the perturbed and unperturbed profiles.

The results from a retrieval taking into account both spectral regions are seen in the respective bottom panels. Although the difference between the unperturbed (black) and the perturbed (blue) retrieval results does not show a large improvement if compared with the 420 to 470 nm results in the top panels, the deviation from the true profile is much smaller and the enhanced value is originating from the perturbation and not so much enhanced from a retrieval artifact. Concluding from these results, the reliability if the two spectral regions are used is better than if only one spectral window is used. This change represents an improvement for the retrieval. Furthermore, there is an improvement in the averaging kernels for lower altitudes, as shown in Figures 3.16 and 3.17. From this it can be concluded, that an increase in sensitivity is obtained from the usage of both spectral regions.

It is also worth to note the consequence of needing high signal to noise ratios: Retrieved profiles have to be averaged to produce meaningful results. Monthly and seasonal means are to be computed as in section 4.3. Sensitivity in single profiles might only be sufficient for retrieval of strong emissions, like from lightning events as investigated in section 4.2. In this section only synthetic retrievals are analyzed, the results have to be validated as in section 4.1.

3.3.2 NO_2 limb retrieval implementation optimized for UTLS

From the sensitivity studies (see section 3.3.1) it can be concluded, that the use of a second spectral region in the retrieval process leads to an improvement. It is not intended to adapt the spectral region for the stratospheric altitude region, since in

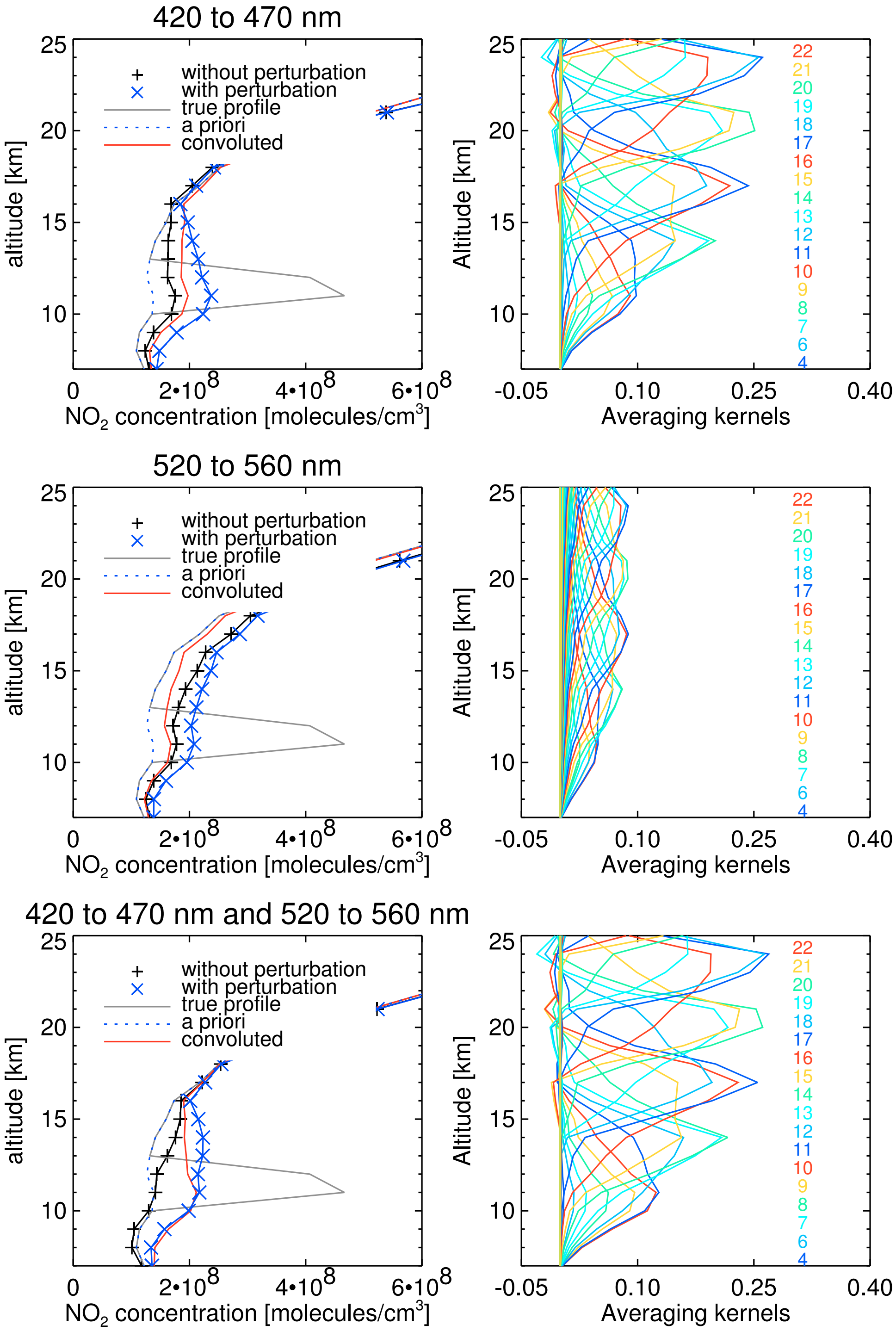

Figure 3.17: This figure shows simulated retrieval results as in Fig. 3.16. An October scenario is shown here.

that case the spectral region of 420 to 470 nm is a well tested and validated choice, see Rozanov *et al.* (2005). Adapting a second spectral range from 520 to 560 nm here is the major difference with respect to the alternative retrieval approaches described starting on page 28. For these approaches, similar spectral ranges as the 420 to 470 nm range are preferred (if the retrieval is performed for an instrument which measures in the UV- visible range). At higher altitudes an improvement from applying the second spectral region (520 to 560 nm) in addition to the 420 to 470 nm range is not expected.

The goal of the present study is to combine the advantages of both spectral regions. Results from the tested and validated version 3.1 of the Bremen NO_2 product are used as a priori profiles. To simplify the discussion, the improved version discussed here is designated as version 3.2 in the context of this work. Since a significant improvement above an altitude of 20 km in the limb profiles is not expected, the regularization is set to strict settings in that altitude region, i.e., the resulting profile is not expected to differ much from the a priori profile of stratospheric NO_2 values. This will result in potentially misleading averaging kernels, because a higher influence of the a priori profiles is usually to be avoided.

One of the reasons for this unconventional approach is the choice of the retrieval settings. Instead of using the information operator approach as in the V3.1 product version, SCIATRAN is set to perform optimal estimation for UTLS retrievals. The SCIAMACHY NO_2 limb V3.1 settings tend to suppress small deviations for the UTLS region, which are not desired. The basic setup is illustrated in Fig. 3.18.

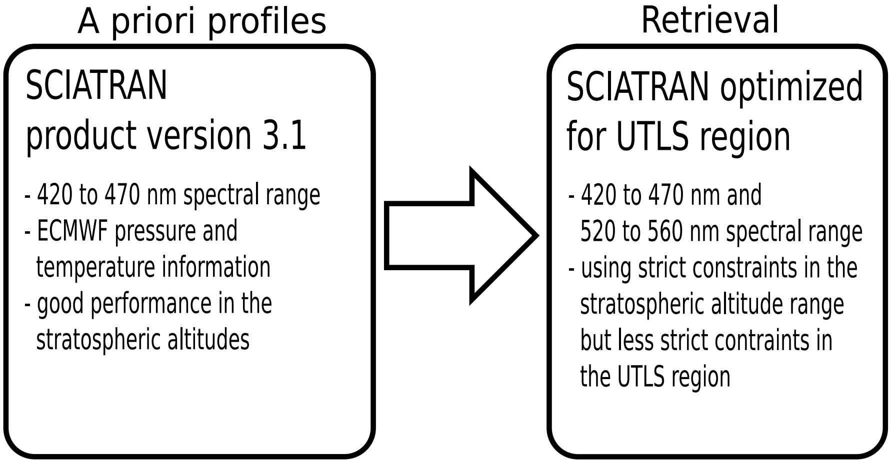

Figure 3.18: This figure shows the setup for the modified retrieval approach.

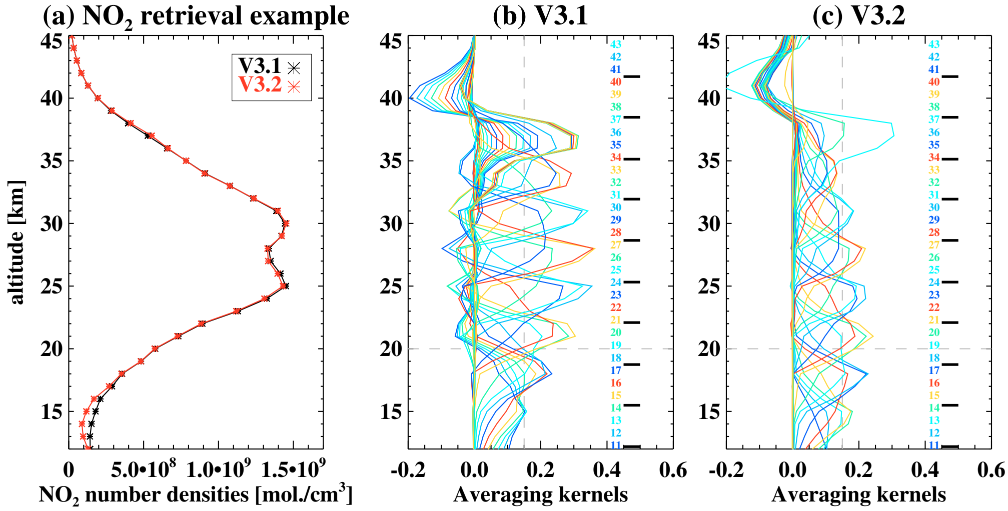

Figure 3.19: An example for the retrieval from V3.1 and V3.2 is given. As intended, the averaging kernels are weak in V3.2 for higher altitudes compared with V3.1 and are similar or better at lower altitudes.

To achieve an altitude-dependent regularization, the diagonal elements of the a priori covariance matrix are changed depending on the altitude. For the altitude of 40 km a variance of only 3% is considered, while the variance for 5 km is set to 36 %. The values for other altitudes are generated by linear interpolation.

One unfortunate aspect is related to the correction spectra. For technical reasons, no Ring correction spectra for the additional spectral region 520 to 560 nm could be calculated. However, using a series of tests investigating the influence of the eta, Ring and undersampling correction spectra, the Ring correction has been found to be of minor influence on the retrieval results. All other correction spectra were successfully extended for the second spectral range and included in the retrieval. Table 3.2 gives an overview of the changes. Changed settings with respect to the SCIATRAN NO$_2$ V3.1 retrieval are highlighted by the boldface. It is also possible to apply different settings for the two spectral regions for some options, such as the polynomial degree. If not stated otherwise, each option is applied to both spectral regions.

An example retrieval is shown in Figure 3.19. The profile belongs to the orbit number 8495, state number 10, azimuth number 3 of 4 (counting from 0), an SZA of 55.7°, and the average coordinates at the tangent point are 45.3° N and 39.98° W. The measurement was performed on the 15th of October in 2003 at 13:23:06 UT. As

SCIATRAN improved retrieval parameter settings	
Forward model	SCIATRAN 2.2 **modified**
Spectral region	420 – 470 nm **& 520 – 560 nm**
Surface albedo	0.3
Clouds treatment	neglected in the retrieval, cloud information included in the output files
Weighting functions type	single scattering
Atmospheric species in the forward model	NO_2, O_3, O_4
Retrieved Atmospheric species	NO_2, O_3
Reference tangent height number	15 ($\approx$ 43 km)
Tangent heights selected for the retrieval	5 – 14 ($\approx$ 9 – 40 km)
Polynomial order	3
Spectral corrections	shift, offset, undersampling, eta (**Ring switched off**)
Spectral smoothing	No
A priori uncertainty	**modified source code, see text**
Signal to Noise Ratio	estimated from spectral residuals
Correlation length	1.5 km
Additional regularization	**Tikhonov smoothing is switched off.**
Solution method	**optimal estimation**
Eigenvalue threshold	**not applicable, since optimal estimation is used**
Iterative scheme	Newton
trace gas replacement	**SCIATRAN V3.1 NO_2 vertical profile**

Table 3.2: These are the changed retrieval settings for version V3.2. Changes with respect to SCIATRAN V3.1 retrieval parameter settings (see Table 2.2) are marked by the **boldface**.

expected, the difference between these two profiles is small above 17 km, and only below this altitude significant differences are seen in panel (a). Above 20 km, the averaging kernels of V3.1 are larger than for V3.2. This is intended, as V3.1 serves as a priori profile and while V3.2 is intended to increase the sensitivity in the UTLS region,no improvement from the additional spectral range is expected in the 20 to 40 km altitude range. At lower altitudes however, the a priori constraints are less strict, allowing larger deviation from the V3.1 a priori profile, resulting in a different NO_2 profile and stronger averaging kernels at 15 km. It should be noted, that this behaviour is not seen in every single profile. There are examples, where the averaging kernels of V3.2 are of the same magnitude at low altitudes compared with V3.1.

Generally, applications and retrievals of both the V3.1 product version and the version improved for UTLS (V3.2) described here, are to be investigated and validated in detail. As V3.1 is used to produce a priori profiles for V3.2, both versions are important for the sensitivity of the V3.2 approach, and thus the validation and discussion of V3.1 data sets in chapter 4 is equally important.

4

Results

4.1 Validation of NO_2 retrieval results

The retrieval of NO_2 is a challenging task with a lot of possible error sources and a sophisticated method is needed to determine the NO_2 amount in the atmosphere from satellite measurements.

Assessing the quality of NO_2 limb retrievals is not trivial. Not all error sources can be quantified in advance and, thus, validation is the only way to estimate the overall error of the retrieved quantities. It is therefore mandatory to validate the results using other sources for NO_2 profiles. These validation sources have to be as precise as possible, and preferably obtained from a different retrieval method, e.g., in situ measurements or results based on the IR spectral region. In this section, various sources for NO_2 profiles in the atmosphere are used for validation. For a description of each source see section 2.5.

4.1.1 Solar occultation instruments

The validation using the solar occultation instruments is performed in a similar way for each instrument. It is straightforward to discuss results from these instruments together in a separate section, as the differences between these three instruments regarding the validation of NO_2 can be analyzed in addition. The results presented in this section have been published in Bauer *et al.* (2011)[1].

---

[1] The following text in Section 4.1.1 is included in the final revised version. However, the peer review process is not fully completed yet. While the text presented here is written by the author of this

The validation results are shown as scatter plots (for SCIAMACHY profiles and the respective photochemically corrected profile) for three different altitude regions, given as partial vertical NO_2 columns (20 to 25 km, 28 to 32 km and 35 to 40 km). This means, that the NO_2 amounts are summed up in 1 km steps for each altitude range. In each scatter plot, results from different latitude regions are identified by color, i.e., black for 90°N to 60°N, red for 60°N to 30°N, blue for 30°N to 30°S, green for 30°S to 60°S, and brown for 60°S to 90°S. To avoid bias resulting from seasonal differences in NO_2 amounts, collocations from each season are analyzed separately. For example, the panels marked with D,J,F (December, January, February) contain collocations from the meteorological winter in the Northern Hemisphere and meteorological summer in the Southern Hemisphere. Linear regression parameters are also given (three cases: all/sunset/sunrise collocations) and the linear regression curve is plotted for all collocations in the scatter plot.

For further investigation, at each altitude h the relative difference RD can be calculated for each collocation pair, defined as:

$$\mathrm{RD}(h) = \frac{x_{\mathrm{SCIA}}(h) - x_{\mathrm{Val}}(h)}{(\overline{x_{\mathrm{SCIA}}}(h) + \overline{x_{\mathrm{Val}}}(h)) \times 0.5}, \tag{4.1}$$

with x_{SCIA} as SCIAMACHY NO_2 number densities and x_{Val} as number densities from the respective validation source. The profiles are normalized with respect to the average of the mean SCIAMACHY NO_2 profile $\overline{x_{\mathrm{SCIA}}}$ and the mean profile from the validation source $\overline{x_{\mathrm{Val}}}$. Both mean NO_2 are calculated from the respective collocation subset. This definition avoids the problem of overemphasized relative deviations due to occasionally very small NO_2 amounts.

4.1.1.1 SAGE II

In Fig. 4.1, a comparison for the profiles in 2003 and 2004 is given for SAGE II and SCIAMACHY with 2338 comparisons, after all collocation criteria are applied as mentioned in Sect. 3.2.2. Of these 2338 cases, 1121 SAGE II measurements were performed during sunset and 1217 during sunrise. The panels on the lefthand side represent partial vertical columns from 20 to 25 km, the middle columns from 28 to 32 km

---

thesis, coauthors have contributed mainly with data sets and support. Their individual contribution is mentioned in the acknowledgements at the end of the present work.

Table 4.1: Latitude ranges for all collocations with SCIAMACHY for each season and instrument in the years 2003 and 2004 (2004 and 2005 for ACE-FTS)

Months	SAGE II	HALOE	ACE-FTS
D,J,F	56.6°N - 78.0°S	56.0°N - 73.2°S	80.0°N - 68.4°S
M,A,M	80.3°N - 79.5°S	78.0°N - 74.9°S	83.4°N - 78.8°S
J,J,A	78.0°N - 54.3°S	72.5°N - 54.7°S	68.2°N - 63.6°S
S,O,N	78.1°N - 68.6°S	77.8°N - 78.7°S	83.7°N - 76.0°S

and the panels on the righthand side from 35 to 40 km. The upper panels include collocations from the months December, January and February (winter in the Northern Hemisphere and summer in the Southern Hemisphere), the panels (d) to (f) the months March, April and May, panels (g) through (i) the months June, July and August, while the lowermost panels (j) to (l) contain collocation pairs from September, October and November. In each panel, latitudinal regions are color-coded, i.e. black for 90°N to 60°N, red for 60°N to 30°N, blue for 30°N to 30°S, green for 30°S to 60°S, and brown for 60°S to 90°S. It should be noted, that due to the orbits of the satellite instruments, collocations might not be found for some seasons and latitude bins, as listed in Table 4.1. For example, in NH winter season (December, January and February) no collocations in the 90°N to 60°N latitude range are found for SAGE II, see also Panels (a) to (c) of Fig. 4.1.

While for lower altitudes (20 to 25 km and 28 to 32 km) the squared correlation coefficient r^2 is larger than 0.80 in most cases and the slope is mostly close to 1, this is not the case for the 35 to 40 km altitude range. At these altitude levels, NO_2 amounts are generally small. Thus, the dynamic range is not high enough to calculate a meaningful linear correlation.

For sunset measurements, r^2 is higher than for sunrise measurements with the notable exception of the uppermost panels, which include a large number of SAGE II sunrise measurements in the SH summer. Generally, the quality of SAGE II NO_2 results is lower for sunrise measurements as a result of technical issues, see Cunnold *et al.* (1991). This is also seen in a comparison with ACE-FTS (Kerzenmacher *et al.*, 2008), which agrees well with sunset SAGE II NO_2, but has a significant high bias compared to sunrise SAGE II NO_2 amounts. This high bias is, however, not seen

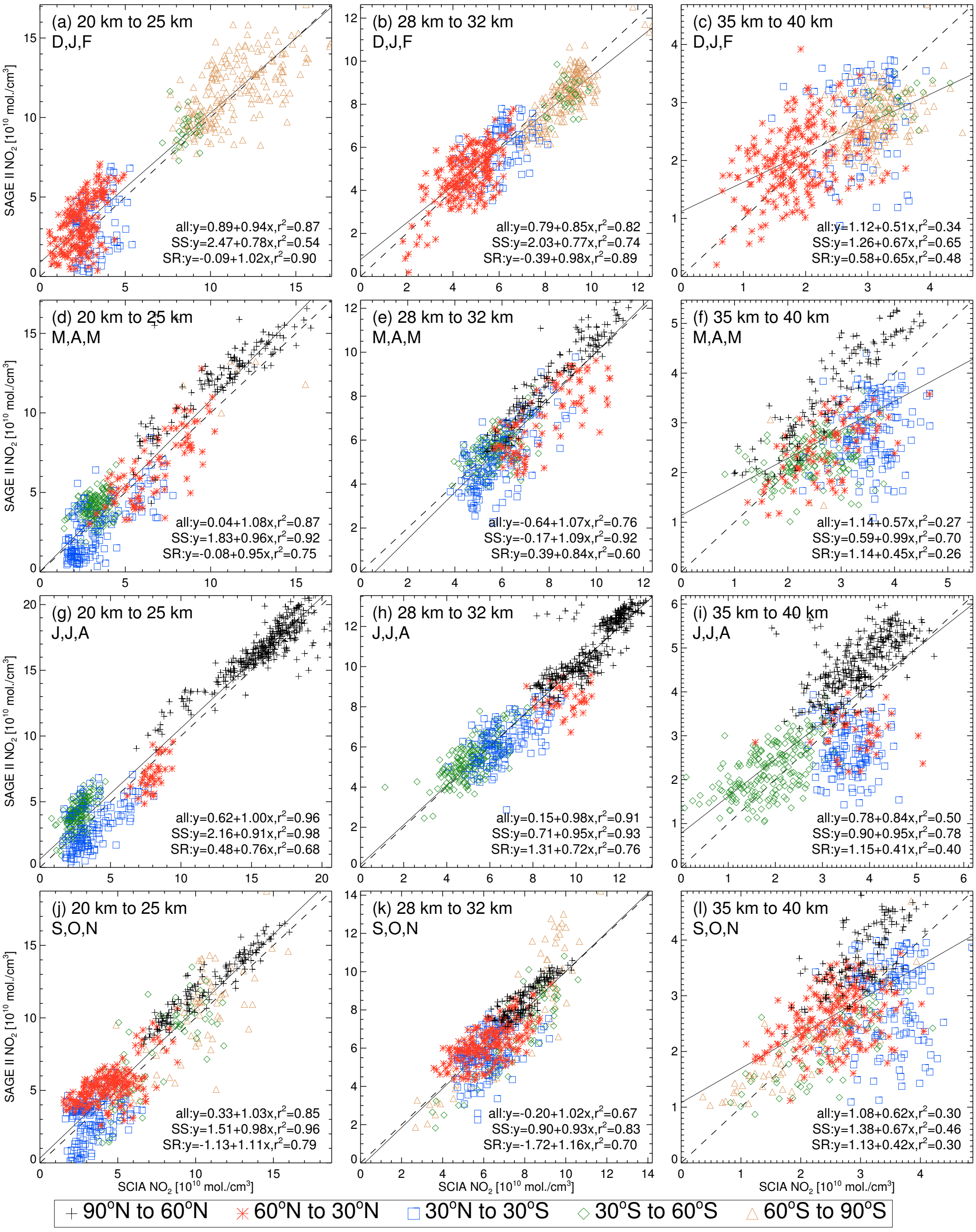

Figure 4.1: Scatter plots of collocated SCIAMACHY and photochemically corrected SAGE II NO_2 results for the years 2003 and 2004 are given for partial vertical columns and grouped in 4 seasonal and 3 altitude ranges (20 to 25 km, 28 to 32 km, and 35 to 40 km). In each panel, collocated pairs from different latitude regions are shown with different colors (black for 90°N to 60°N, red for 60°N to 30°N, blue for 30°N to 30°S, green for 30°S to 60°S, and brown for 60°S to 90°S).

when comparing ACE-FTS to the other satellite instruments in the analysis.

To discuss the results of the scatter plots, average NO_2 profiles are calculated and shown in Fig. 4.2. Averaged SCIAMACHY NO_2 amounts for each bin are shown in black, and standard deviations of these values calculated for the particular collocation sample are given as black dashed lines. Photochemically corrected and averaged SAGE II NO_2 amounts are plotted as red line, and the respective standard deviations are shown as red-dashed line. As expected for SCIAMACHY measurement conditions, the NO_2 levels are largest in summer conditions at high latitudes. In NH summer (JJA) conditions, NO_2 levels decrease southwards with the lowest values seen in the 30°S to 60°S latitude range. Unfortunately, there are no collocations available south of 54.3°S, see Table 4.1. This is mirrored in NH winter conditions (DJF), with the largest NO_2 amounts in the South (30°S to 60°S). In the Tropics (30°N to 30°S), NO_2 levels are low on average, especially at altitudes below 25 km. This directly influences the validation results, as high NO_2 levels are expected to be easier detected. Also, the same absolute NO_2 errors result in large relative differences, if the NO_2 levels are small.

From the relative differences (RD) calculated with Eq. 4.1, mean values (MRD) are computed for each latitude/season bin and summarized in Table 4.2. The MRD values are given for an altitude range from 20 to 40 km for sunset and sunrise values separately. The $MRD_{corr.}$ values are related to the diurnal effect error correction and are discussed later. In the same table, SZAs and average local times $\overline{l.t.}$ for the SCIAMACHY measurements and the number of collocations, n (sunset/sunrise), are given. The MRD is not calculated for cases with less than 10 collocations. Since SCIAMACHY measurements at NH high latitudes can include afternoon measurements, these local times are averaged separately. Large relative NO_2 differences can be found in tropics, while small MRDs are correlated whit higher NO_2 amounts. Also, the uncertainty of the photochemical correction increases from high latitudes to the tropics. It is noteworthy, that between 90°N to 60°N, SAGE II NO_2 levels are generally higher than SCIAMACHY. Since all measurements at 90°N to 60°N in this comparison are sunset measurements, this agrees well with Bracher *et al.* (2005). Similar results were also reported for the comparison of data from MIPAS (Michelson Interferometer for Passive Atmospheric Sounding) instrument on ENVISAT with SAGE II results, see

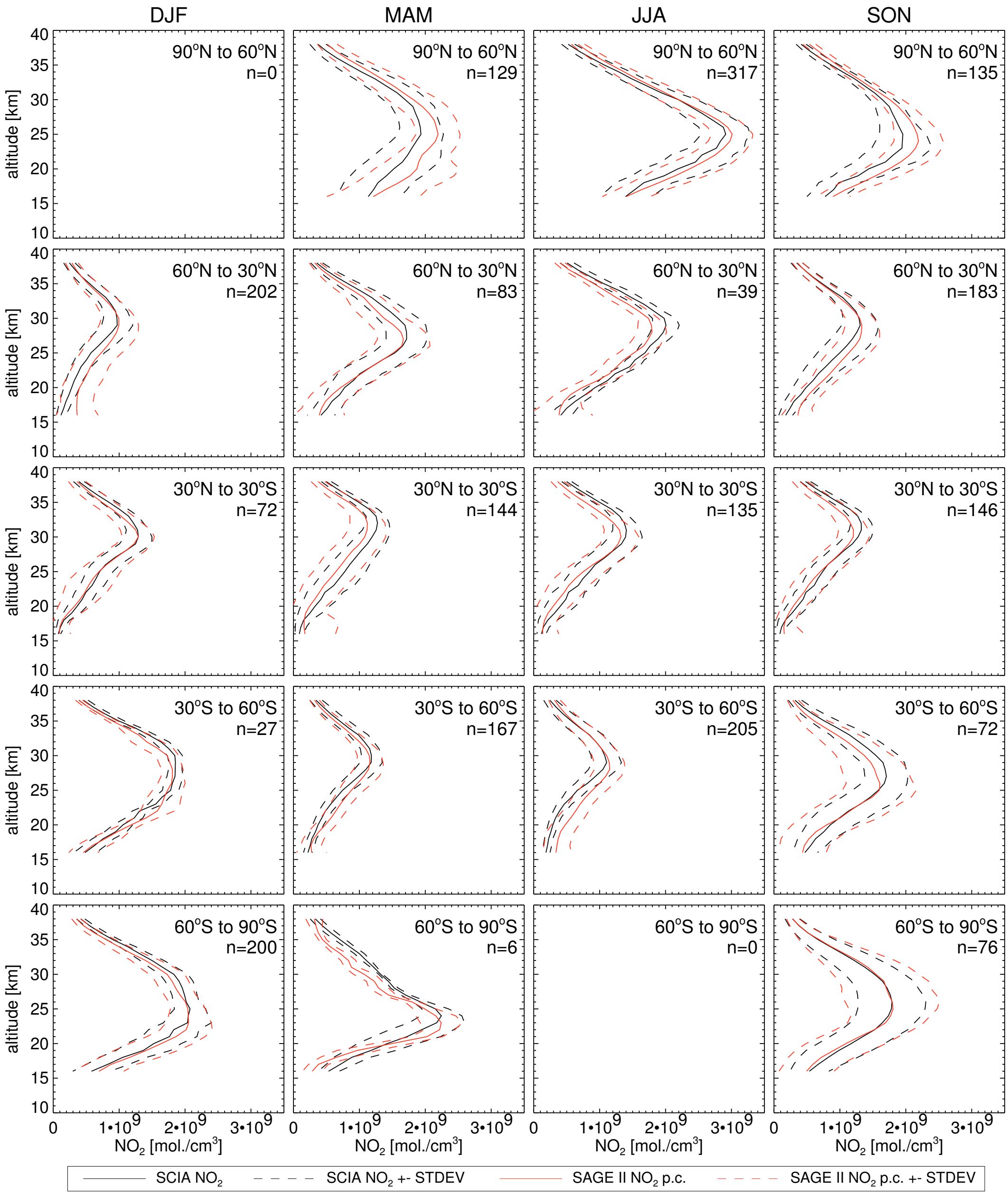

Figure 4.2: From the SCIAMACHY and SAGE II collocation pairs for 2003 and 2004, vertical NO_2 profiles are averaged for collocation subsets of different latitude ranges and seasons. The panels are ordered from top to bottom depending on latitude range, with northern latitudes on top. The panels are also ordered from left to right depending on season. In each panel, the NO_2 profiles are averaged for SCIAMACHY (black line) and photochemically corrected SAGE II NO_2 profiles (red). The standard deviations for both subsets are given as dashed lines in the respective color and added/subtracted from the averaged profiles.

Wetzel *et al.* (2007). At 76°N to 60°N and pressure levels from 32 to 2.7 hPa, mean relative differences (normalized w.r.t. to SAGE II) were found to be within -32 to -11% for several months from April to September in 2002 and 2003. This agrees well with the present results at similar regions and timeframes (e.g., -36% to -8% at 90°N to 60°N in June to August (J,J,A)). While the results for other latitude ranges agree less well, the tendency for more positive MRDs at southern latitudes is present as well (e.g. 63°S to 80°S in December and February, 27 to 2.3 hPa, 0 to 38% compared with -10 to 6% in the present work). Unfortunately, the distribution of the coincidences between SAGE II sunset and sunrise measurements was not discussed, which might have an impact on the mean relative differences.

An important error source in the compared data is the diurnal effect error. NO_2 concentrations from solar occultation instruments show a significant high bias at altitudes below 25 km if the diurnal effect is not considered. Since it is known to vary depending on latitude and season (Brohede *et al.*, 2007a), an individual error estimation is calculated for each collocation pair. For profiles and latitude zones (except for high latitudes) shown in Fig. 4.2, the mean values for the relative diurnal effect error are presented in panels (a) to (c) of Fig. 4.3.

To estimate the influence of the diurnal effect error on retrieved NO_2 profiles, each photochemically corrected SAGE II NO_2 profile is adjusted with the matching estimated diurnal effect error. As sunset and sunrise measurements are expected to lead to different results, the correction is applied separately for these cases. The red curve in panels (e) to (x) shows averaged RDs calculated with Eq. (4.1) for SAGE II sunset conditions while sunrise conditions are shown in orange. In both cases, a dotted line gives the mean relative differences $\mathrm{MRD}_{corr.}$ after the diurnal effect error correction has been applied. The $\mathrm{MRD}_{corr.}$ values are summarized in Table 4.2.

This is not done for high latitudes, as the SCIAMACHY profiles with high SZAs are also expected to be significantly influenced by the diurnal effect error. Although the agreement is improved for sunset measurements, the relative differences increase for sunrise measurements. As discussed before, there is a significant difference between SAGE II NO_2 sunset and sunrise NO_2 comparisons with sunset measurements believed to be of a better quality, which is a known feature of SAGE II.

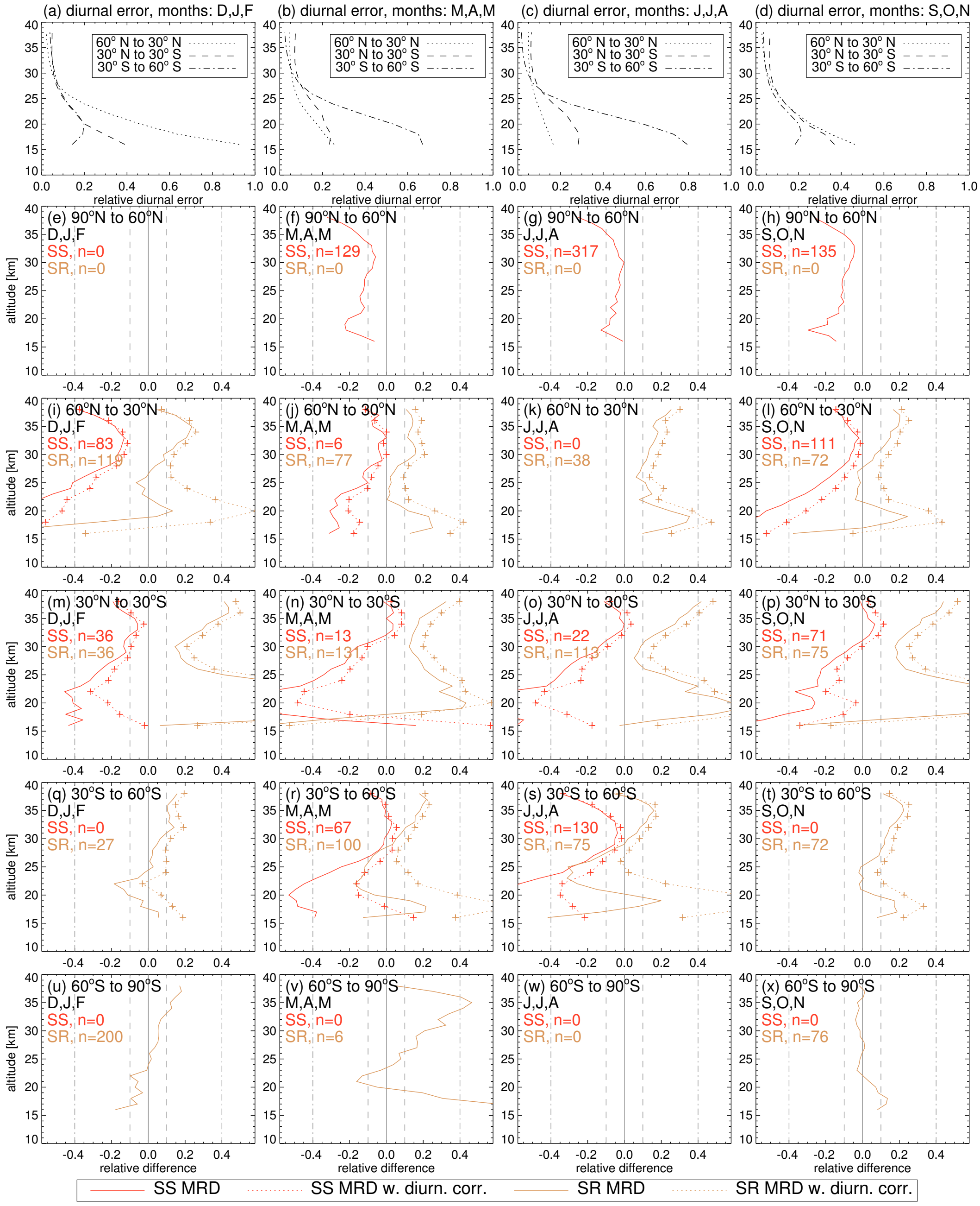

Figure 4.3: Panels **(a)** to **(c)**: Relative diurnal effect errors for the SAGE II profiles shown in Fig. 4.2. A model was used to estimate the diurnal effect error for each SAGE II occultation. These represent the mean errors over the latitude/seasonal bin. The influence of this error on the agreement between the SAGE II and SCIAMACHY is estimated in panels **(i)** to **(t)** for each latitude and season. MRDs with photochemical corrections and without diurnal scaling are displayed as red (sunset) and orange (sunrise) solid lines. MRDs with consideration of the diurnal effect are given as dashed lines with the same color-coding.

Table 4.2: Mean relative differences (MRD) for all SAGE II comparisons and for an altitude range from 20 to 40 km, respectively. Mean solar zenith angles $\overline{\text{SZA}}$ and mean local times $\overline{\text{l.t.}}$ for SCIAMACHY are given for each bin. $\text{MRD}_{corr.}$ represents comparisons, where an additional diurnal effect error correction can be applied.

months	latitude	SCIA	SCIA $\overline{\text{l.t.}}$	n	MRD min/max/avg [%]			$\text{MRD}_{corr.}$ min/max/avg [%]	
	range	SZAs	am(pm)	SS/SR	all	SS	SR	SS	SR
DJF	90°N - 60°N			0/0	n<10				
	60°N - 30°N	55.9-76.8	10.0	83/119	-36/6/-11	-67/-13/-31	-8/24/8	-57/-11/-29	-21/59/19
	30°N - 30°S	34.2-57.8	9.6	36/36	-2/13/5	-45/-6/-21	15/88/40	-32/-2/16	21/112/51
	30°S - 60°S	50.1-59.0	8.7	0/27	-19/16/5	n<10	-19/16/5	n<10	-3/19/12
	60°S - 90°S	50.3-89.7	7.8(22.9)	0/200	-10/18/6	n<10	-10/18/6		
MAM	90°N - 60°N	55.7-86.9	11.3(17.2)	129/0	-43/-6/-15	-43/-6/-15	n<10		
	60°N - 30°N	22.7-61.8	10.0	6/76	-2/14/7	n<10	0/16/9	n<10	0/26/15
	30°N - 30°S	22.8-62.3	9.4	13/131	10/29/19	-70/4/-19	12/37/23	-48/8/-13	20/57/33
	30°S - 60°S	58.3-84.5	8.8	100/67	-28/12/-3	-49/3/-13	-17/22/3	-24/6/-6	2/39/16
	60°S - 90°S	73.3-80.7	7.3	0/6	n<10	n<10	n<10		
JJA	90°N - 60°N	39.1-87.2	11.3(19.1)	317/0	-36/0/-8	-36/0/-8	n<10		
	60°N - 30°N	26.9-51.9	9.9	0/38	6/24/14	n<10	6/25/15	n<10	14/37/23
	30°N - 30°S	24.6-61.6	9.4	22/113	1/32/16	-69/0/-22	5/50/25	-48/4/-17	14/74/37
	30°S - 60°S	57.0-84.6	8.8	130/75	-52/1/-18	-66/-4/-24	-31/16/-6	-57/-2/-20	-40/65/9
	60°S - 90°S			0/0	n<10				
SON	90°N - 60°N	54.6-87.3	11.1(16.5)	135/0	-35/-4/-12	-35/-4/-12	n<10		
	60°N - 30°N	40.6-74.8	10.0	111/72	-23/5/-6	-44/-2/-16	-4/20/7	-31/-1/-12	5/36/17
	30°N - 30°S	26.2-51.9	9.5	71/75	0/20/11	-37/7/-10	18/78/36	-20/11/-3	25/97/48
	30°S - 60°S	39.1-75.1	8.6	0/72	-2/22/10	n<10	-2/22/10	n<10	-11/25/15
	60°S - 90°S	47.6-89.7	8.2	0/76	-7/4/-1	n<10	-7/4/-1		

4.1.1.2 HALOE

Similarly to SAGE II, available data allow a comparison of the years 2003 and 2004 for HALOE. A total of 2592 comparisons are performed, of which 913 are done during the HALOE sunset and 1679 during the sunrise. As for SAGE II, the comparison results are presented as a scatter plot, see Fig. 4.4. In comparison, the r^2 levels are mostly closer to 1, and the differences between sunset and sunrise linear regression parameters are smaller. For 20 to 25 km and 28 to 32 km, the SCIAMACHY NO_2 amounts are smaller on average compared with HALOE NO_2.

Fig. 4.5 shows the averaging vertical distributions from SCIAMACHY and HALOE in the similar way as it was done for SAGE II (see Fig. 4.2). Again, the MRD values in Table 4.3 are smaller for latitude/season bins with generally larger NO_2 amounts. Contrary to SAGE II, it is the SCIAMACHY product which shows larger NO_2 amounts than HALOE, at least for altitudes below 20 km, which are not displayed in the scatter plot (Figure 4.4), but for MRD values in Fig. 4.6. At altitudes above 22 to 25 km, SCIAMACHY NO_2 shows a low bias compared with HALOE NO_2 for NH and SH high latitudes. A low bias in HALOE NO_2 v17 was discovered in Gordley *et al.* (1996) for altitudes below 25 km, and aerosols were reported as a major error source. For HALOE NO_2 v19, a comparison with the shuttle-based FTIR-instrument ATMOS is done by Randall *et al.* (2002), which indicates that the low bias of about 0.5 ppbv for HALOE at low altitudes was reduced to 0.2 to 0.3 ppbv in the new version. It is stated, that with the low NO_2 levels below 25 km, this can still result in a negative bias of up to 40%. In Borchi & Pommereau (2007), a low bias or altitude mismatch for O_3 is reported at altitudes below 23 km in the tropics for HALOE v19. This indicates, that the positive bias of SCIAMACHY seen below 25 km is most probably due to quality issues of HALOE data. Additionally, HALOE NO_2 retrieval applies a correction for the diurnal effect error, which would lead to a negative bias of SCIAMACHY compared with HALOE if uncorrected.

4.1.1.3 ACE-FTS

The third instrument to compare with is ACE-FTS. Because of the mission time, the years 2004 and 2005 are chosen for investigation. In this comparison, 525 collocations

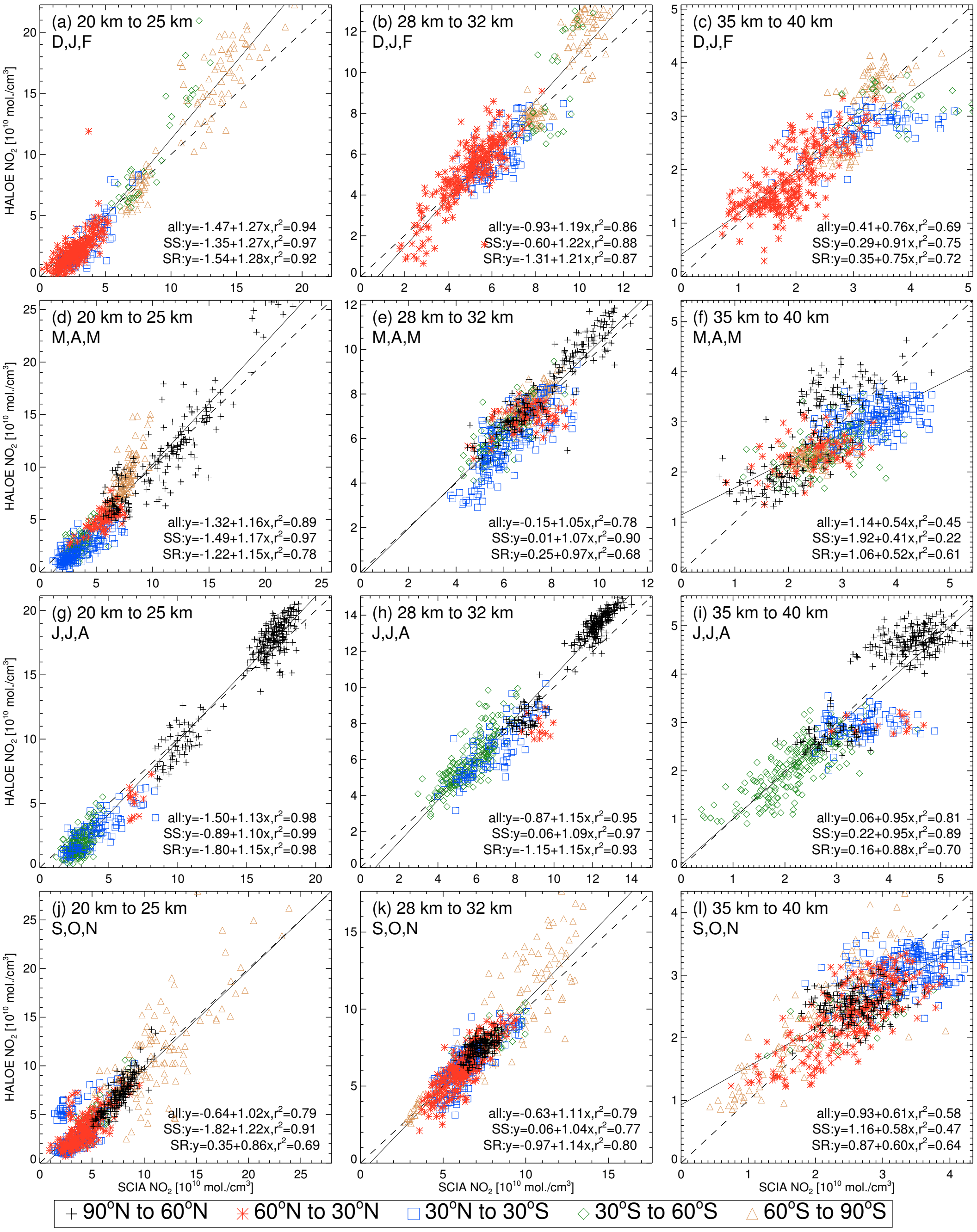

Figure 4.4: Same as Figure 4.1, but for HALOE data.

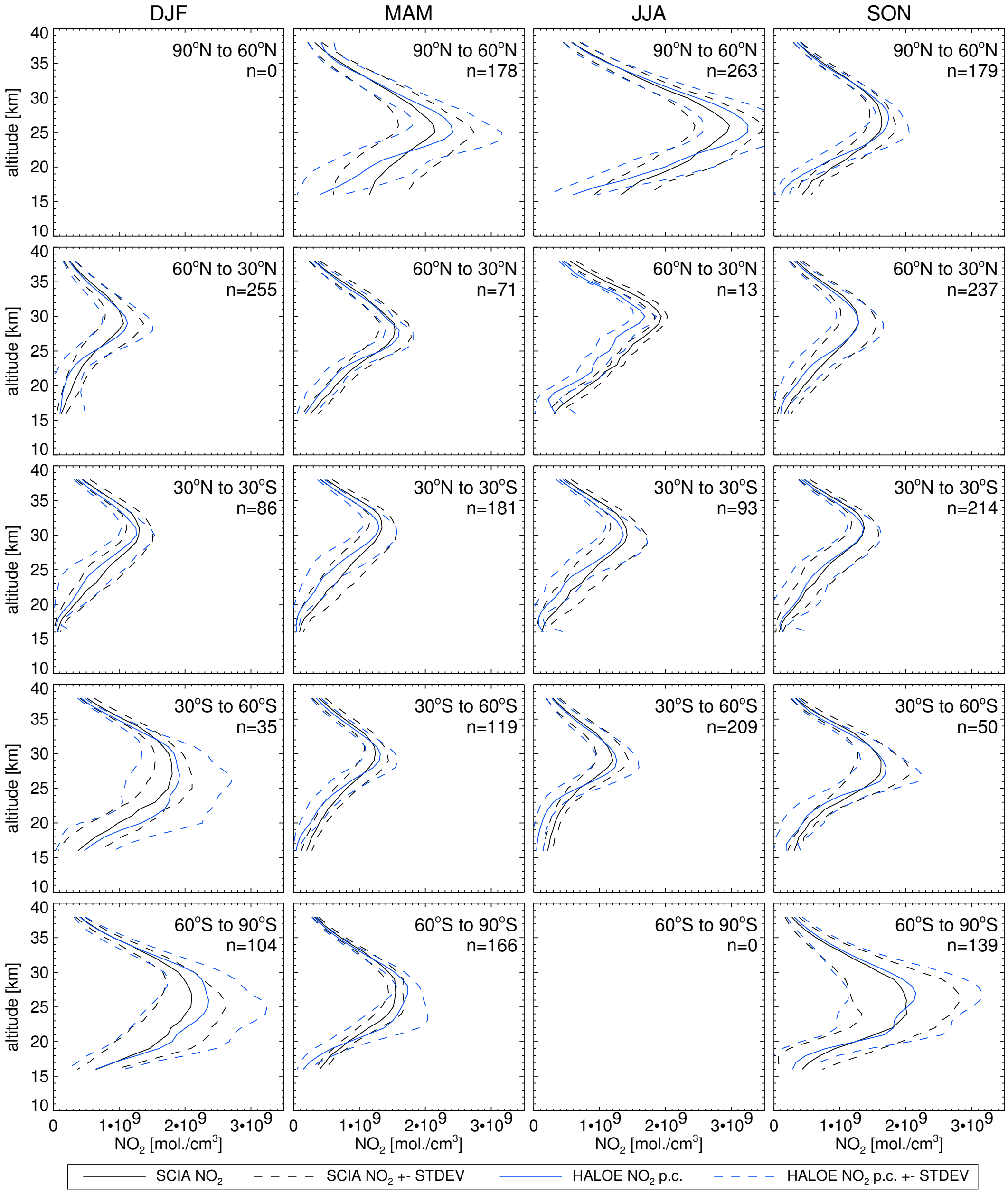

Figure 4.5: Same as Fig. 4.2, but for HALOE data.

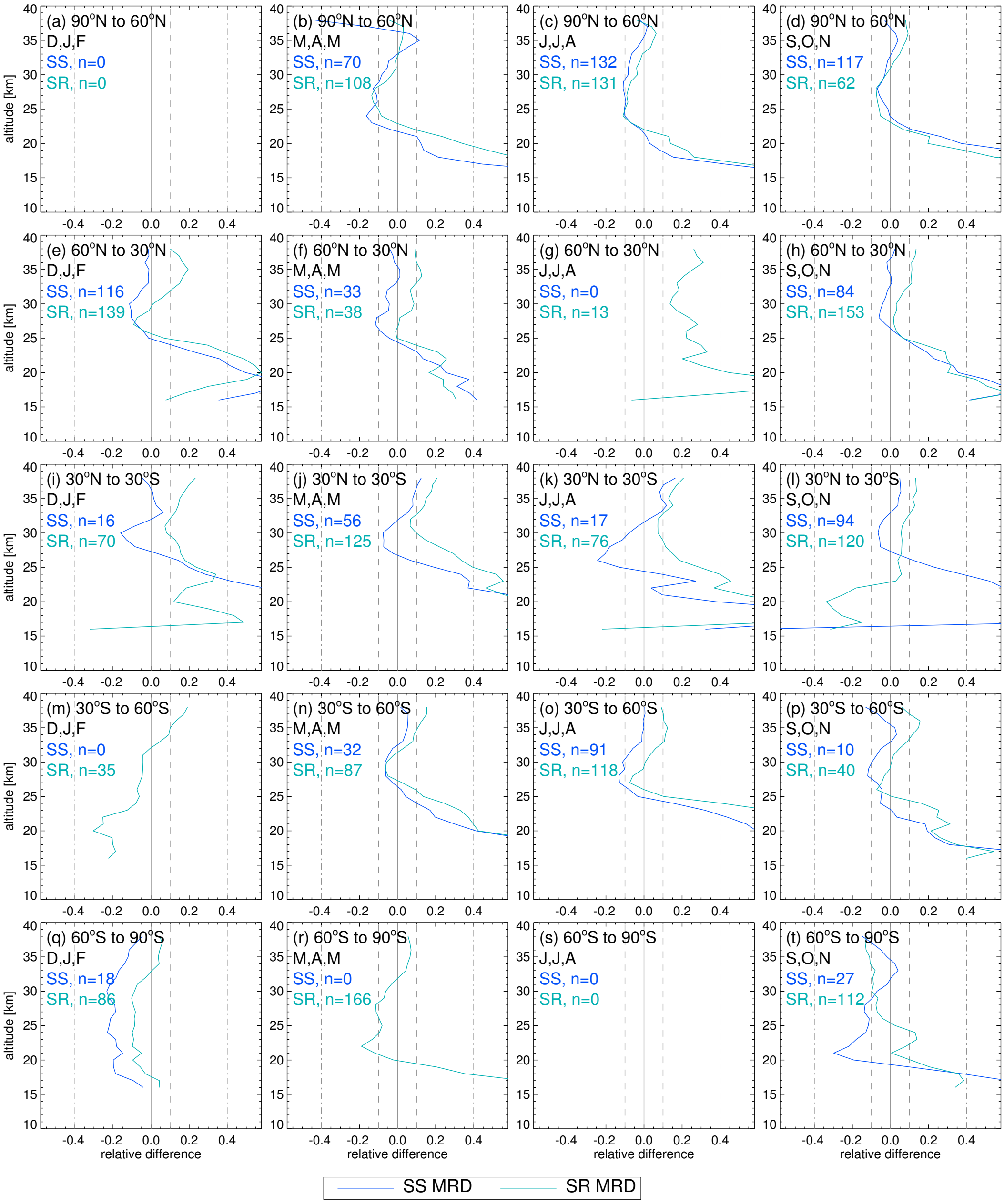

Figure 4.6: MRDs between SCIAMACHY and photochemically corrected HALOE NO_2 profiles are displayed as blue (sunset) and cyan (sunrise) solid lines for each latitude and season.

Table 4.3: Same as Table 4.2, but for HALOE collocations. An altitude range from 20 to 40 km is covered. $\mathrm{MRD}_{corr.}$ values are not given, as the diurnal effect error correction can not be applied for HALOE, as HALOE NO_2 is already corrected for this.

months	latitude range	SCIA SZAs	SCIA $\overline{\text{l.t.}}$ am(pm)	n SS/SR	MRD min/max/avg [%] all	SS	SR
DJF	90°N - 60°N			0/0	n<10		
	60°N - 30°N	54.9-75.9	10.0	116/139	-9/48/8	-11/42/2	-9/55/14
	30°N - 30°S	28.4-55.3	9.4	16/70	3/34/16	-16/88/11	7/34/18
	30°S - 60°S	31.1-50.8	8.8	0/35	-25/19/-1	n<10	-25/19/-1
	60°S - 90°S	46.8-72.8	8.0	18/86	-13/3/-6	-23/-3/-16	-10/6/-4
MAM	90°N - 60°N	57.8-87.7	11.0(18.9)	70/108	-46/16/-7	-70/12/-11	-18/24/-3
	60°N - 30°N	38.5-61.4	10.0	33/38	-5/23/5	-12/23/-1	-1/26/9
	30°N - 30°S	23.1-62.3	9.5	56/125	3/57/21	-8/59/12	7/56/26
	30°S - 60°S	54.1-78.6	9.0	32/87	-6/37/10	-7/30/4	-6/40/12
	60°S - 90°S	65.6-78.8	7.9	0/166	-19/7/-4	n<10	-19/7/-4
JJA	90°N - 60°N	40.4-87.1	10.8(20.1)	132/131	-13/6/-5	-11/2/-6	-17/13/-3
	60°N - 30°N	27.7-34.6	9.8	0/13	14/33/24	n<10	14/33/24
	30°N - 30°S	22.1-62.9	9.4	17/76	4/45/17	-24/27/2	7/52/21
	30°S - 60°S	54.4-82.9	8.9	91/118	-10/78/12	-13/54/4	-8/102/20
	60°S - 90°S			0/0	n<10		
SON	90°N - 60°N	55.6-69.8	11.0(12.3)	117/62	-7/24/1	-7/26/1	-8/21/2
	60°N - 30°N	40.5-72.0	10.0	84/153	-1/32/9	-6/33/4	2/32/12
	30°N - 30°S	26.9-54.5	9.5	94/120	0/20/8	-6/82/14	-25/14/5
	30°S - 60°S	29.4-68.1	9.0	10/40	-7/29/6	-18/18/-4	-7/31/8
	60°S - 90°S	66.6-89.7	6.8	27/112	-13/6/-7	-30/4/-10	-13/14/-5

in 2004 are used (304 at ACE-FTS sunset, 221 at sunrise) and 1143 collocations (513 at sunset, 630 at sunrise) in 2005.

A large number of profiles in 2004 (525 collocations, 304 at ACE-FTS sunset, 221 at sunrise) is used for this comparison, and even more (1143 collocations, 513 at sunset, 630 at sunrise) for the year 2005. However, with 879 sunset and 920 sunrise profiles, this is the smallest dataset of the three instruments. Scatter plots are shown in Fig. 4.7 revealing generally high r^2 values, larger than 0.9 in all cases below 35 to 40 km (Both sunset and sunrise measurements are included).

Fig. 4.8 shows the averaged NO_2 profiles in each latitude/season bin, where SCIAMACHY results are shown as a black line with the standard deviations for the subset of collocations as a dashed black line. Photochemically corrected and averaged ACE-FTS NO_2 profiles are given as a green line, while the standard deviations for each

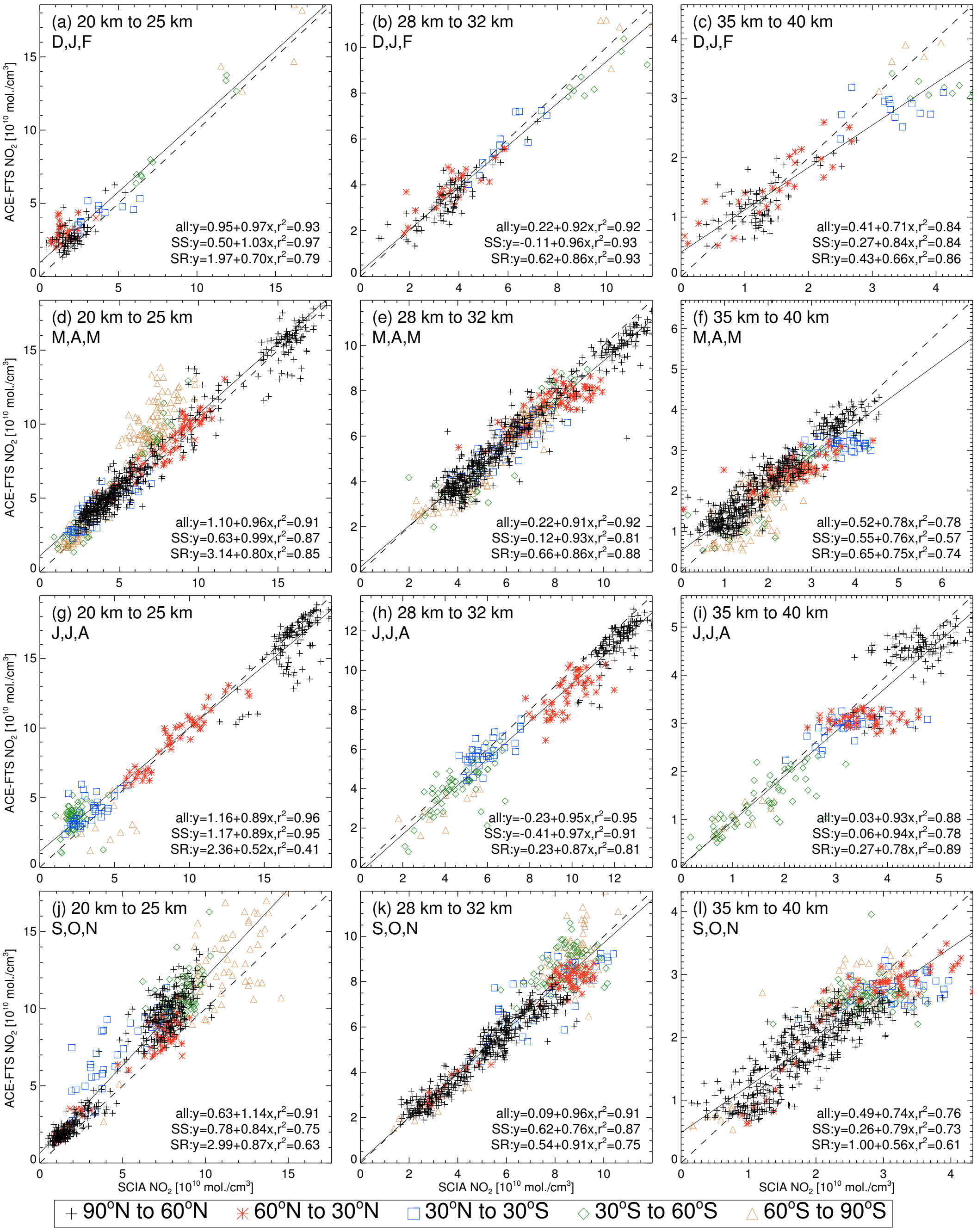

Figure 4.7: Same as Fig. 4.1, but for ACE-FTS. Data sets from the years 2004 and 2005 are shown in this figure.

subset of profiles are shown as dashed green lines. Contrary to HALOE and SAGE II, collocations are also available at 90°N to 60°N in NH winter and 60°S to 90°S in SH winter. About 50% of all collocations are found between 90°N to 60°N in just two seasons, namely, in March, April and May (487 collocations), and in September, October and November (409 collocations). Two latitude/seasonal bins in the Southern Hemisphere contain less than 10 collocations in December, January and February. The summary of MRDs for SCIAMACHY to ACE-FTS comparisons is given in Table 4.4.

With the same method as applied for SAGE II, the possible influence from the diurnal effect is removed from each photochemically corrected ACE-FTS profile, see Fig. 4.9. Although in many cases the $\mathrm{MRD}_{corr.}$ values are larger above 25 km, an considerably improvement below this altitude for both tropics and middle latitudes is seen for both sunset and sunrise measurements, i.e. $\mathrm{MRD}_{corr.}$ is closer to zero in most cases. Contrary to SAGE II, this correction can be regarded as an improvement for both sunset and sunrise ACE-FTS NO_2, at least at altitudes below 25 to 30km. Also not considering the diurnal effect correction, averaged MRD values for sunset and sunrise measurements do not show the large differences seen for SAGE II. However, the number of collocations, n, is low in many latitude/seasons bins for either sunset or sunrise measurements appears. Excluding 90°N to 60°N and 60°S to 90°S, where the assumption of low diurnal effect errors for SCIAMACHY is not valid, the $\mathrm{MRD}_{corr.}$ values are given in Table 4.4.

In Kerzenmacher *et al.* (2008), ACE-FTS V2.2 NO_2 VMR profiles were compared with data from a number of instruments. It was found, that ACE-FTS NO_2 has a small negative bias (about 10%) in the 23 to 40 km altitude range. This agrees well with the (varying) positive bias of SCIAMACHY limb NO_2 in Figure 4.9 for altitudes above 25 km. The negative bias below this altitude can be mostly attributed to the diurnal effect error. This statement might also be true for the NH and SH high latitudes (Fig. 4.8), but this cannot be analyzed with the present method.

4.1.1.4 Discussion

Summing up the results from the three instruments, the lowest MRDs are found at high latitudes and summer conditions (North and South) and all three instruments show a reasonable agreement with SCIAMACHY, although distinct features are seen.

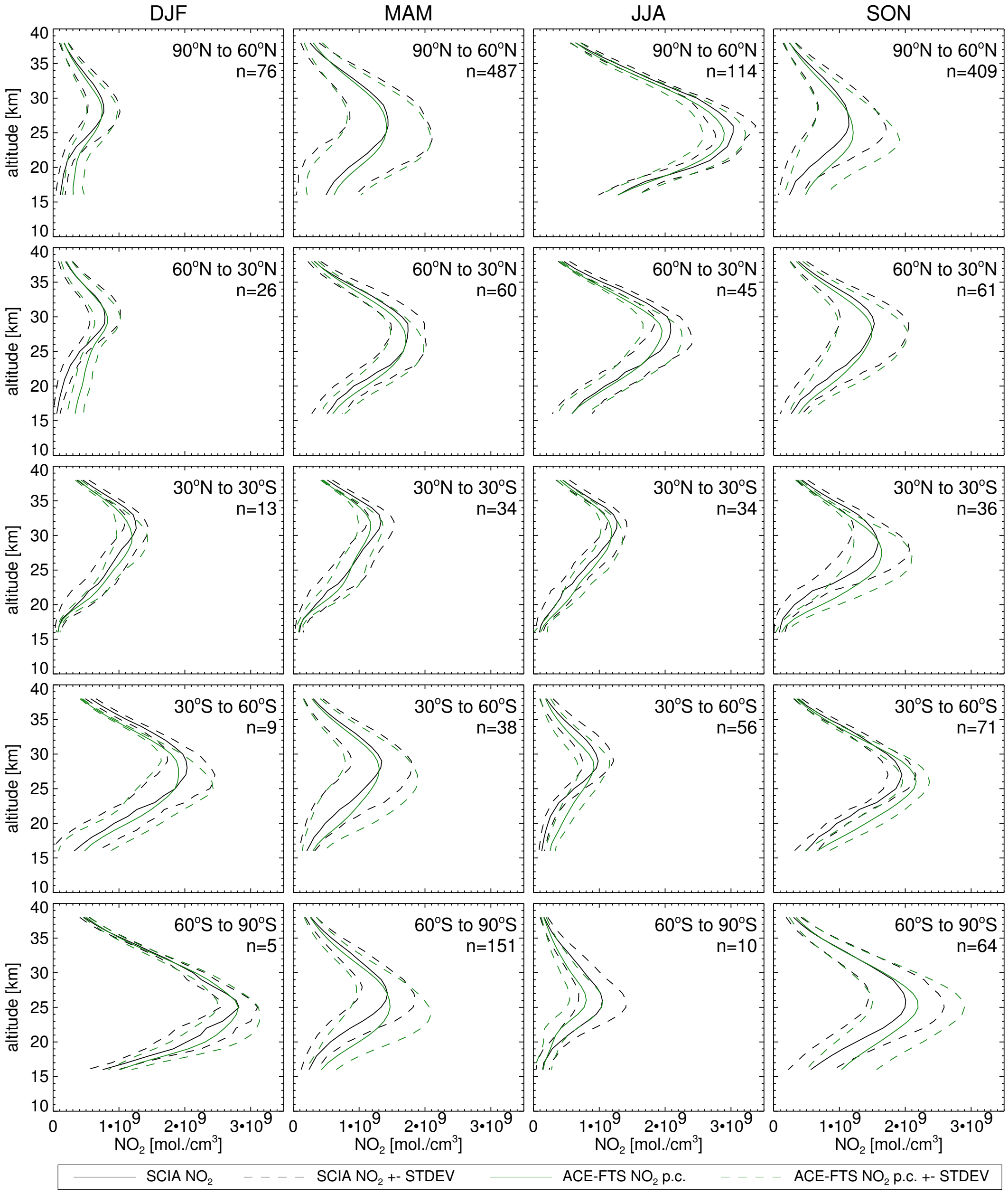

Figure 4.8: Same as Fig. 4.2, but for ACE-FTS. Instead of 2003 and 2004, datasets from 2004 and 2005 are averaged in this figure.

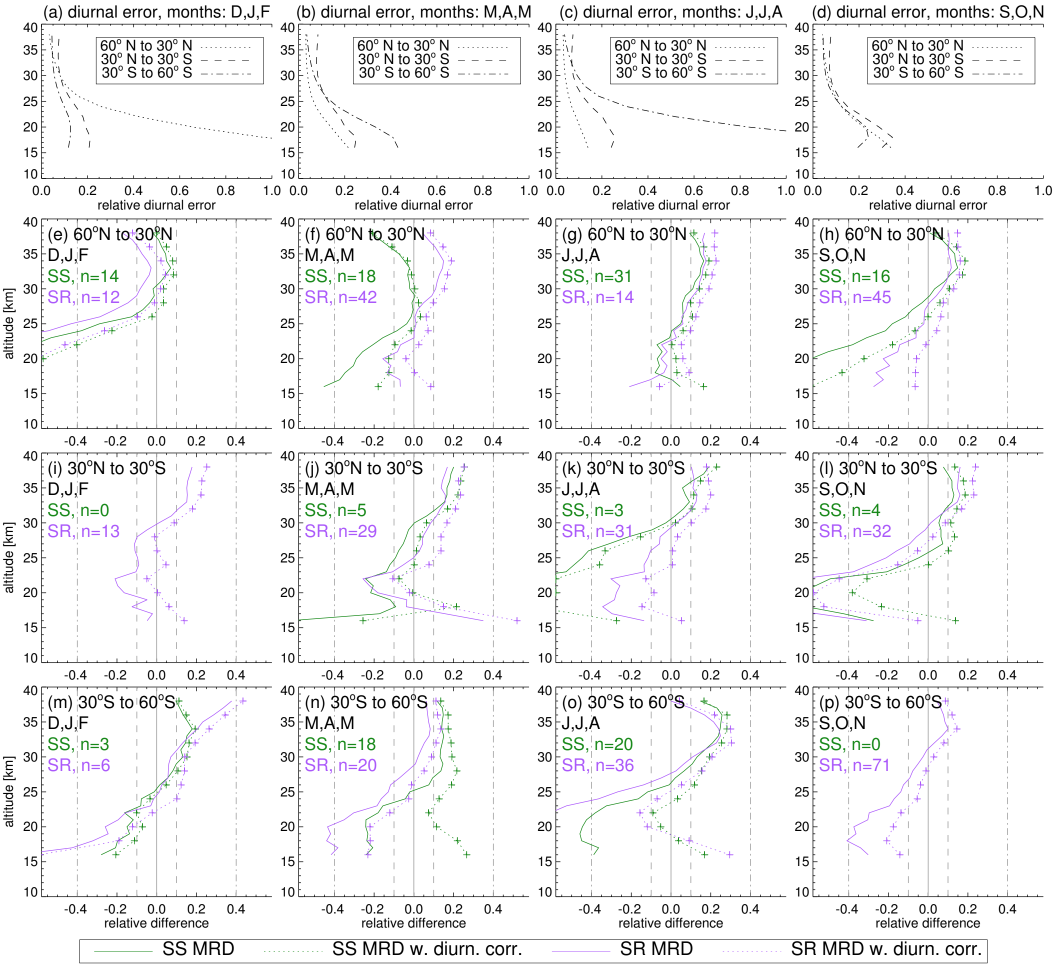

Figure 4.9: For the latitude regions and seasons investigated in Fig. 4.8, the relative diurnal error for ACE-FTS measurements is estimated and averaged in panels **(a)** to **(c)**. Panels **(d)** to **(p)** show estimates of how this error influences the MRD between photochemically corrected ACE-FTS and SCIAMACHY limb NO_2 amounts. The solid green lines shows the MRD of photochemically corrected NO_2 sunset profiles from ACE-FTS without the diurnal effect with SCIAMACHY results, and the green dashed line with the diurnal effect. The same calculations are performed for sunrise measurements, with MRD values shown as violet solid lines, and violet dashed for $MRD_{corr.}$ values with considering the diurnal effect.

Table 4.4: Same as Table 4.2, but for ACE-FTS collocations. An altitude range from 20 to 40 km is covered.

months	latitude range	SCIA SZAs	SCIA $\overline{\text{l.t.}}$ am(pm)	n SS/SR	MRD min/max/avg [%]			MRD_{corr} min/max/avg [%]	
					all	SS	SR	SS	SR
DJF	90°N - 60°N	77.7-89.8	10.9(12.7)	53/23	-51/11/-5	-32/13/-2	-90/13/-14		
	60°N - 30°N	68.0-84.7	10.3	14/12	-90/3/-20	-75/7/-14	-105/-3/-28	-57/9/-9	-61/4/-17
	30°N - 30°S	36.2-44.8	9.4	0/13	-21/18/1	n<10	-21/18/1	n<10	-5/25/11
	30°S - 60°S	44.6-47.4	8.9	3/6	n<10	n<10	n<10	n<10	n<10
	60°S - 90°S	48.9-58.0	8.2	5/0	n<10	n<10	n<10		
MAM	90°N - 60°N	44.4-89.6	11.1(15.3)	385/104	-28/6/-3	-35/5/-6	-16/11/3		
	60°N - 30°N	27.0-59.8	10.2	18/42	-12/10/2	-28/1/-9	-8/15/6	-32/3/-8	-4/19/9
	30°N - 30°S	25.1-50.2	9.5	5/29	-25/17/5	n<10	-26/17/5	n<10	-11/25/14
	30°S - 60°S	50.8-89.1	8.7	18/20	-33/10/-1	-24/15/6	-35/8/-4	0/22/14	-22/14/3
	60°S - 90°S	66.4-89.2	7.8	45/106	-48/14/-3	-17/41/16	-50/12/-6		
JJA	90°N - 60°N	39.8-87.1	10.4(20.0)	114/0	-8/7/4	-8/7/4	n<10		
	60°N - 30°N	26.7-41.8	10.0	31/14	-7/17/8	-7/16/8	-5/18/10	0/19/10	5/23/16
	30°N - 30°S	26.8-50.5	9.4	3/31	-33/13/-2	n<10	-30/13/-1	n<10	-13/20/7
	30°S - 60°S	60.7-89.0	8.8	20/36	-63/24/-3	-43/26/4	-74/25/-7	-9/28/12	-23/31/6
	60°S - 90°S	83.7-88.7	8.4	0/10	-4/46/26	n<10	-4/46/26		
SON	90°N - 60°N	55.6-88.3	11.0(12.8)	180/229	-34/11/-3	-42/11/-3	-33/12/-3		
	60°N - 30°N	40.5-81.2	10.3	16/45	-18/12/2	-50/15/-5	-15/12/3	-32/19/0	-6/16/9
	30°N - 30°S	26.6-33.6	9.2	4/32	-69/16/-7	n<10	-70/16/-7	n<10	-58/24/0
	30°S - 60°S	33.8-53.6	8.8	0/71	-30/10/-5	n<10	-30/10/-5	n<10	-18/15/0
	60°S - 90°S	51.4-86.3	8.2	8/56	-19/1/-7	n<10	-19/2/-7		

Higher NO_2 values at lower altitudes are one of the reasons for mostly smaller relative differences at high latitudes. Additionally, the SCIAMACHY measurements at high latitudes feature higher SZAs (about 70° to slightly below 90°) compared to measurements in the tropics, where a SZA of 30° is common. This means a smaller photochemical correction of the profiles. Contrary to HALOE and SAGE II, collocations with ACE-FTS allow to compare NO_2 amounts during high latitudes winter (90°N to 60°N in D,J,F), i.e., for very low NO_2 amounts with maximum values smaller than 1.0×10^9molec cm^{-3} and large SCIAMACHY SZAs (77.7° to 89.8°). In this case, the MRDs are comparably high (-51% to 11% at 20 to 40 km), see Table 4.4, which means that large SZAs do not automatically yield low MRDs.

NO_2 concentrations change rapidly at daybreak and change much less during the day at most altitudes investigated here. Still, the photochemical correction method can not be excluded as a significant error source. Also, the altitude range of the three occultation instruments varies and the number of averaged profiles is also smaller at low altitudes. For example, 572 HALOE profiles are averaged at most altitudes in the tropics. This number decreases to 563 at 18 km and further to only 492 valid profiles at 15 km. However, these numbers are still reasonably high. It is worth mentioning that the profiles were not smoothed, i.e. differences in resolution have not been accounted for. Also, estimating the change of including the diurnal effect error in photochemically corrected profiles results in improvements for sunset measurements of SAGE II and both sunset and sunrise measurements for ACE-FTS at 25 km and below, where the diurnal effect error shows the highest values.

Table 4.5 presents MRDs for all instruments (as given in Tables 4.2 to 4.4) averaged either over all seasons or over all latitude bins. In addition, the MRDs averaged over the whole globe all seasons (i.e., the complete data set) are given as a reference for 20 to 40 km and 25 to 35 km. If these values are considered, the reader is strongly recommended to take the MRDs of the individual latitude/seasonal bins into account, since negative and positive relative differences may cancel each other out. This is especially true for the MRDs in the all latitudes/all seasons scenario, which results in MRDs smaller than 20% or even 10% as a consequence of averaging. In the right column of Table 4.5, standard deviations for the relative differences of all altitudes and collocations are given for each subset. Both at 90°N to 60°N and in NH summer, standard deviations of less than 20% are seen for all instruments. In the tropics, the standard deviations can exceed 30%.

MRD values obtained after applying the diurnal scaling are denoted as $MRD_{corr.}$ in Tables 4.2 and 4.4. As the diurnal scaling only improves the agreement below 25 km (with the exception of SAGE II sunrise), the $MRD_{corr.}$ values for 20 to 40 km are not always smaller than those without the diurnal scaling.

To estimate the bias of SCIAMACHY NO_2, the MRDs at 25 to 35 km and the case of all seasons and all latitudes are investigated. It should be noted, that the bias for individual seasons and latitudes may be different. Below 25 km, diurnal effect errors and other error sources have a strong influence on the result, so the bias is difficult to determine at these altitudes. For SAGE II sunset results, an average MRD of -6% remains, i.e. photochemically corrected SAGE II NO_2 amounts are higher than SCIAMACHY NO_2 on average. In Bracher *et al.* (2005), SAGE II NO_2 values were found to be high in comparison to SCIAMACHY with MRDs of $-10\,\%$ to $-35\,\%$ between 20 and 38 km. However, these values apply only to a subset of measurements with a SZA range of 60 to 70°, only sunset measurements and only for the year 2003. If we limit the collocations for the SAGE II comparisons by applying similar restrictions, the MRD values lie between $-7\,\%$ and $-30\,\%$, on average $-17\,\%$. If the MRDs are normalized with respect to the particular SAGE II profile as in Bracher *et al.* (2005), the MRD values lie between $-8\,\%$ and $-39\,\%$, which agree very well with the known results.

For HALOE, a global comparison including all seasons at 25 to 35 km shows a small average MRD of only $-2\,\%$. In Gordley *et al.* (1996), no obvious bias was found between 25 and 40 km. If the same calculation is done for ACE-FTS (MRD globally, all seasons, 25 to 35 km), a 5% average MRD is found. For altitudes between 25 and 40 km, a negative bias of about 10% is estimated by Kerzenmacher *et al.* (2008) for ACE-FTS, which agrees qualitatively with our results. From the results of the three instruments, a low bias for SCIAMACHY NO_2 between 0 and -5% is most likely, although it is strongly recommended to not underestimate the influence of the uneven distribution of collocations in each validation set on this result.

Regarding standard deviations, these are found for all three satellites to be smaller than 20% in the global/biannual mean comparison at 20 to 40 km, and smaller than 17% between 25 and 35 km. In NH summer (June, July and August), standard deviations are less than 20% globally, which is also the case for all season subsets between

Table 4.5: Mean relative differences (MRD) for all comparisons at 20 to 40 km. Standard deviations (STDEV) are calculated for each subset of collocations in the given altitude range.

months	latitude	MRD min/max/avg [%]			STDEV
	range	all	SS	SR	[%]
SAGE II					
all	90°N - 60°N	-37/-3/-10	-37/-3/-10	n=0	14
all	60°N - 30°N	-17/8/-2	-52/-6/-21	1/18/9	29
all	30°N - 30°S	4/24/14	-46/2/-15	12/54/28	34
all	30°S - 60°S	-27/8/-5	-60/-2/-20	-13/18/4	28
all	60°S - 90°S	-8/14/5	n=0	-8/14/5	19
DJF	90°N - 90°S	-13/10/1	-60/-10/-28	-7/19/8	25
MAM	90°N - 90°S	-9/7/0	-33/-4/-13	2/23/12	26
JJA	90°N - 90°S	-22/2/-4	-36/-2/-10	1/27/14	20
SON	90°N - 90°S	-9/6/-2	-24/-1/-12	4/22/11	24
all	90°N - 90°S	-11/5/-2	-33/-4/-12	0/22/11	23
all, 25 to 35 km		-4/5/1	-10/-4/-6	3/18/9	17
HALOE					
all	90°N - 60°N	-19/12/-4	-22/8/-6	-13/17/-2	17
all	60°N - 30°N	-4/35/8	-9/34/2	-1/36/13	29
all	30°N - 30°S	3/35/15	-8/68/12	7/31/16	33
all	30°S - 60°S	-7/32/7	-11/43/3	-5/28/9	30
all	60°S - 90°S	-11/0/-5	-24/-5/-13	-10/1/-4	22
DJF	90°N - 90°S	-7/9/2	-14/14/-4	-4/14/4	27
MAM	90°N - 90°S	-6/15/2	-29/18/-3	-4/13/4	25
JJA	90°N - 90°S	-8/14/0	-12/5/-5	-4/25/5	18
SON	90°N - 90°S	-4/12/3	-7/18/1	-2/13/5	25
all	90°N - 90°S	-6/12/2	-10/12/-3	-3/13/4	24
all, 25 to 35 km		-6/6/-2	-10/1/-6	-3/8/1	17
ACE-FTS					
all	90°N - 60°N	-17/8/-1	-20/6/-1	-19/11/-1	18
all	60°N - 30°N	-15/12/3	-16/10/1	-14/13/4	17
all	30°N - 30°S	-42/15/-2	-47/16/-3	-41/15/-2	28
all	30°S - 60°S	-34/14/-2	-28/20/5	-35/12/-4	24
all	60°S - 90°S	-33/10/-3	-14/26/10	-35/8/-5	22
DJF	90°N - 90°S	-38/10/-3	-27/10/-2	-56/15/-6	27
MAM	90°N - 90°S	-20/9/-2	-27/6/-4	-18/12/1	20
JJA	90°N - 90°S	-3/12/5	-5/10/5	-27/17/3	14
SON	90°N - 90°S	-31/10/-3	-42/11/-3	-30/10/-3	21
all	90°N - 90°S	-20/10/-1	-15/8/0	-25/12/-1	20
all, 25 to 35 km		-2/10/5	3/8/6	-6/12/4	13

90°N and 60°N, while between 60°S and 90°S standard deviations are less than 22%. However, in tropics, standard deviations can exceed 30%.

4.1.2 Balloon borne measurements

The measurements considered here have already been used for validation of former versions of SCIATRAN, see Butz *et al.* (2006). More background information can be found in section 2.5.4. The balloon retrievals are already photochemically corrected by Butz *et al.* (2006), so the corrected results from these measurements are used here as well.

In Figures 4.10 and 4.11 comparisons between balloon and satellite measurements are shown. Details on the balloon borne measurements and corresponding SCIAMACHY observations are presented in Table 4.6. The yellow area marks the range with coincident air masses, as determined from air mass trajectory calculations. The grey area marks the error range for the balloon borne measurements (black), which have also been smoothed as described in section 2.5.4. Version 3.1 retrieval results are shown with blue triangles, while the modified version V3.2 results are shown in red including error bars.

Although one has to be concerned about potential problems in the tropopause region as the model used for photochemical corrections is known to be less accurate at the altitude below 15 km, the agreement in Fig. 4.10 between SCIATRAN retrievals and balloon measurements is good. The results from the improved version do not reveal a significant difference in these examples as compared to V3.1. The error bars resulting from theoretical precisions for the improved SCIATRAN retrievals are of the same order of magnitude as for the profiles retrieved from the balloon borne measurements.

The agreements for measurements shown in Fig. 4.11 are also good. However, these results are mainly useful for the stratospheric region, as the altitude range with coincident air masses starts at an altitude of 17 km in the lowermost case. It is currently not feasible to interpret the difference in NO_2 outside the altitude range with coincident air masses.

Balloon flight date, time/ UT	**Location**	**Geophysical condition**	**Available datasets**	**Satellite coincidence orbit, date, time/ UT**	**Altitude range/km**	**Time delay/h**	**Spatial distance/km**
04 Mar. 2003	Kiruna	high lat. spring	SO: LPMA	5273, 4 Mar., 11:05	20-30	-5.1	369-496
13:20-16:17	67.9° N,	SZA: 71.1°-94.1°		5285, 5 Mar., 7:17	23-24	+15.3	498-499
	21.1° E						
23 Mar. 2003	Kiruna	high lat. spring	BA: LPMA,	5545, 23 Mar., 11:07	18-28	-5.2	268-496
14:47-17:28	67.9° N,	SZA: 78.9°-94.7°	DOAS	5558, 24 Mar., 9:01	19-29	+17.4	10-495
	21.1° E		SO: LPMA,	5545, 23 Mar., 11:07	20-30	-6.2	63-458
			DOAS	5558, 24 Mar., 9:01	17-30	+16.0	256-453
9 Oct. 2003	A. s. l'Adour	mid-lat. fall	BA: DOAS	8407, 9 Oct., 9:51	17-31	-6.5	738-988
15:39-17:09	43.7° N,	SZA:72.0°-87.8°		8421, 10 Oct., 9:20	25-33	+17.2	547-977
	0.3° W						
24 Mar. 2004	Kiruna	high lat. spring	BA: DOAS	10798, 24 Mar., 10:35	12-33	-5.4	371-499
14:04-17:31	67.9° N,	SZA: 74.5°-95.3°		10812, 25 Mar., 10:04	6-16	+19.9	32-485
	21.1° E		SO: DOAS	10798, 24 Mar., 10:35	10-33	-6.9	191-436
				10812, 25 Mar., 10:04	10-20	+16.7	301-475
17 June 2005	Teresina	tropical winter	BA: DOAS	17240, 17 June, 11:53	25-30	-8.1	382-491
18:32-21:13	5.1° S,	SZA: 60.6°-95.8°		17255, 18 June, 13:02	5-33	+18.4	6-490
	42.9° W		SO: DOAS	17240, 17 June, 11:53	23-32	-9.1	519-971
				17255, 18 June, 13:02	8-33	+16.2	12-496

Table 4.6: Background information for Figures 4.10 to 4.11. This table lists LPMA/DOAS O_3 and NO_2 profile measurements and the coincident Envisat/SCIAMACHY overpasses. Balloon borne solar occultation measurements are abbreviated as SO, and balloon ascent measurements as BA. Source: Butz *et al.* (2006)

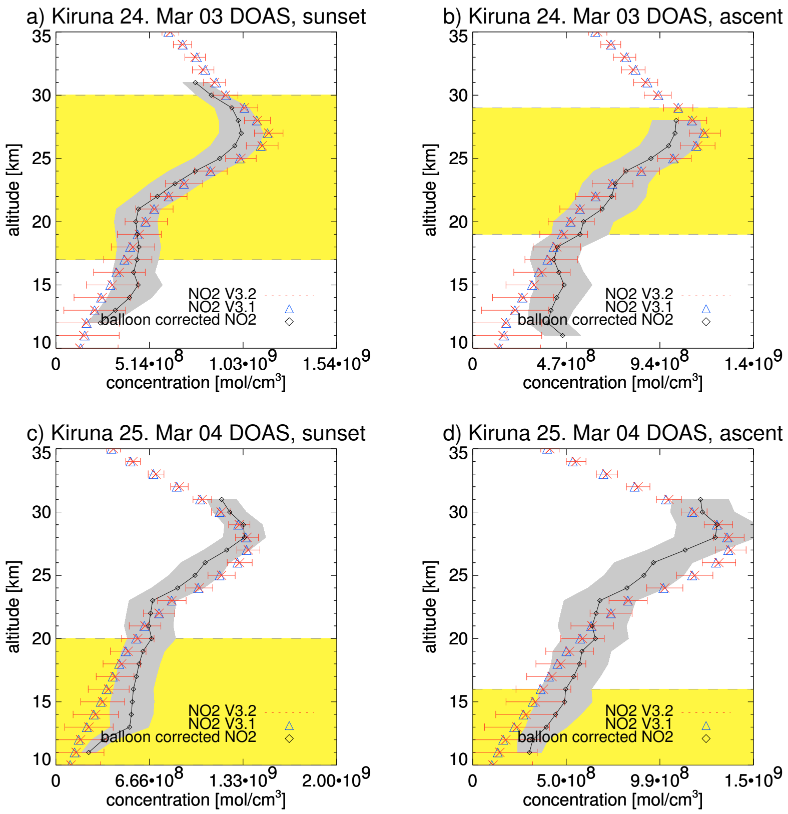

Figure 4.10: Four measurements showing a comparison of balloon borne photochemically corrected measurements with the two SCIAMACHY NO_2 profile retrievals V3.1 and V3.2, respectively. All measurements in this figure have been performed at Kiruna, 67.9° N, 21.1° E.

4.1.3 CARIBIC

As described in section 2.5.5, only longitudinal comparisons are possible with CARIBIC observations, due to the measurement setup. No vertical profiles of NO_2 are generated. The results can be seen in Fig. 4.12. Photochemically corrected NO_2 values for the CARIBIC data are provided. They are calculated with MESSy (part of the climate model EMAC, see section 2.5.6) and shown as green solid line in the graph. As cloud information is available through the SCODA algorithm (see section 2.3), all measurements, for which clouds are detected, are discarded from this comparison.

From the available measurements only those data sets are shown, which feature a significant number of coincident SCIAMACHY measurements and are also not con-

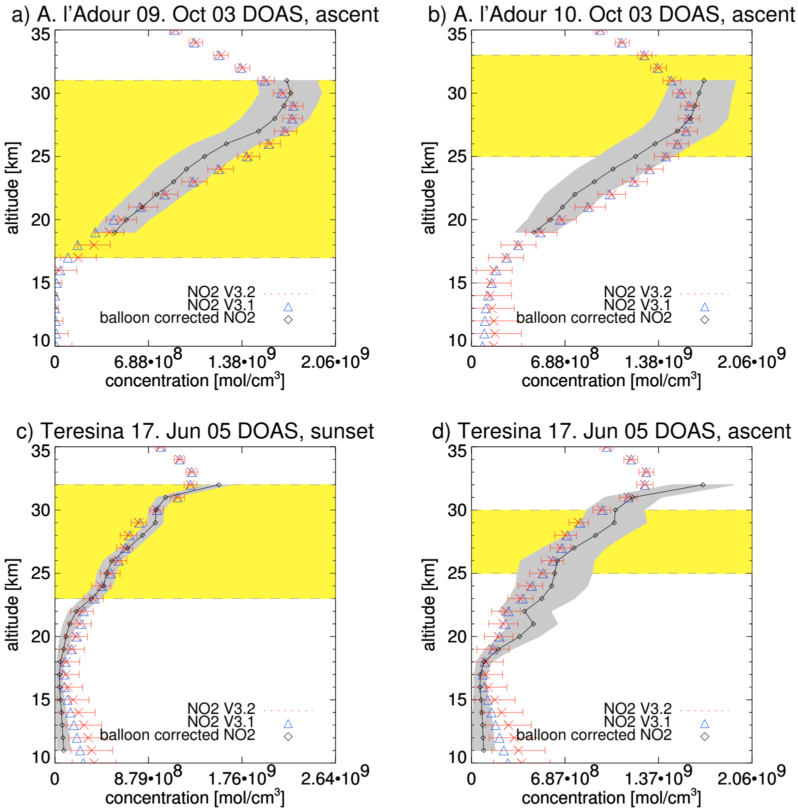

Figure 4.11: A comparison similar to Fig. 4.10 is shown. (a) and (b) are observed above Aire sur l'Adour (43.7° N, 0.3° W), while (c) and (d) show measurements from Teresina (5.1° S, 42.9° W).

taminated by clouds. Good agreement is found between the SCIATRAN NO_2 retrieval results and the CARIBIC results. The different measurement setups lead to difficulties in the comparison. While CARIBIC provides a continuous stream of NO_2 values along the flight path, only point values from the number of coincident SCIATRAN NO_2 profiles can be used for comparison. Good agreement is also found between SCIATRAN NO_2 V3.1 results and results from the improved version V3.2. In general the values from the improved version are larger in the presented cases, which leads to a better agreement in some although not in all measurements investigated here.

CARIBIC remains an important source for validation and although it is not suitable for validation of vertical NO_2 profiles, NO_2 concentrations in the UTLS altitude region can be compared to CARIBIC results.

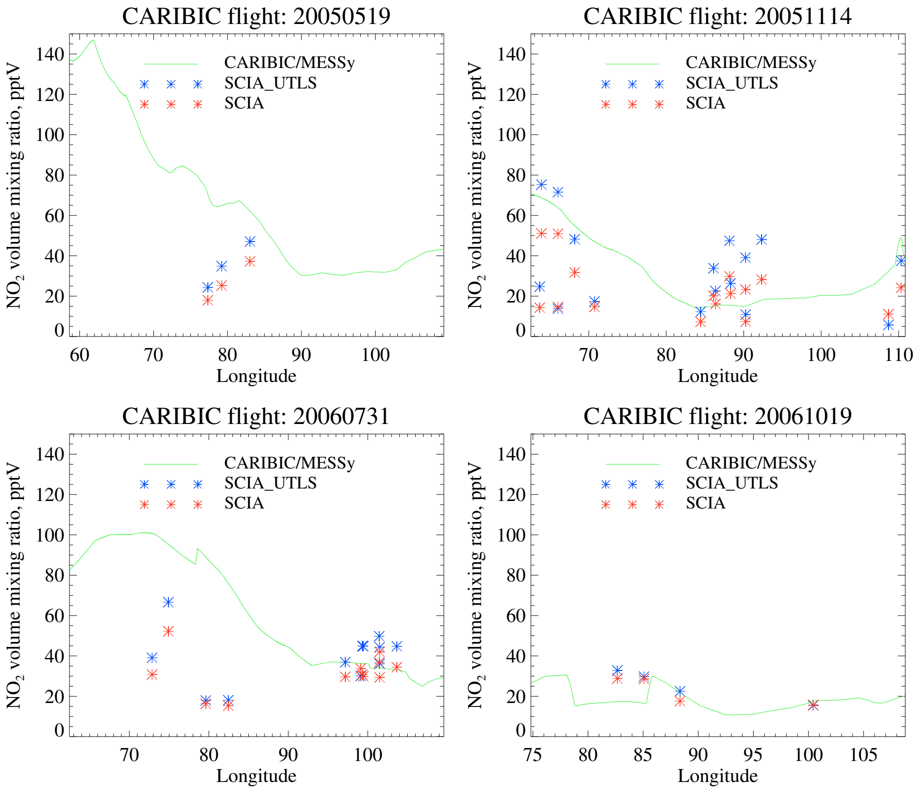

Figure 4.12: A selection of CARIBIC flights compared with results from the standard NO_2 retrieval and the improved NO_2 retrieval. The x-axis shows the NO_2 amount in pptV.

4.1.4 SPURT

As described in section 2.5.5, SPURT is an interesting validation source, although the NO_2 values have to be computed from in situ NO measurements. This is performed using the EMAC model framework (see section 2.5.6). Cloud masking has been applied in the same manner as for section 4.1.3.

Results can be seen in Fig. 4.13 and 4.14. Reasonable agreement is found between SCIATRAN V3.1 NO_2 and the NO_2 values calculated from SPURT. This is also the case for the improved version. The most significant difference between the two SCIATRAN versions is the improved precision in the version V3.2. For a correct interpretation it is important to notice, that the vertical axis in these figures is given in pressure levels, not in km.

Since the method of obtaining NO_2 values is completely different compared to the other validation sources discussed here, SPURT results are an important validation

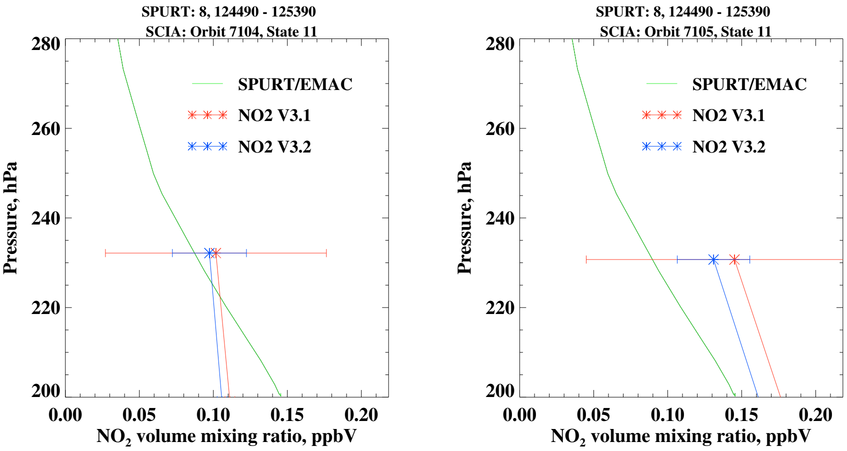

Figure 4.13: A comparison is shown between SCIATRAN V3.1 NO_2 retrievals (red), retrieval results using the improved version V3.2 (blue) and NO_2 values (green) calculated from SPURT NO with the EMAC/MESSy framework.

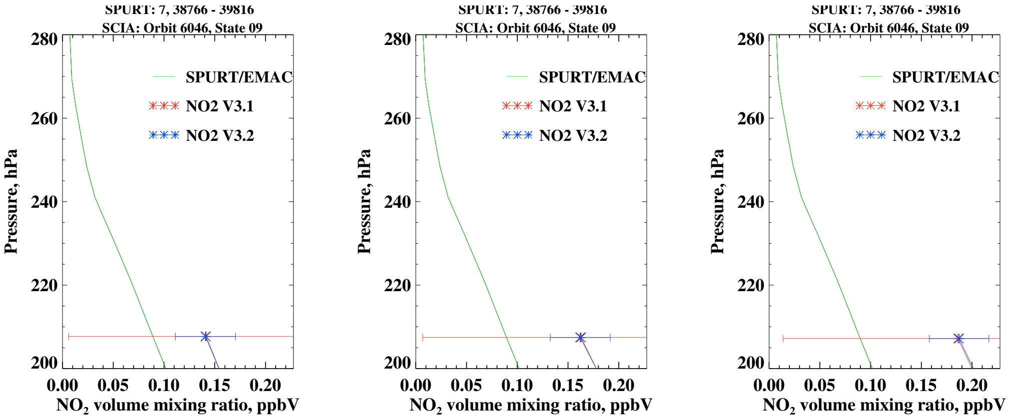

Figure 4.14: See Fig. 4.13 for a description. In this case, three of the four measurements from SCIAMACHY orbit 6046 and state id 09 are collocated with the SPURT measurement.

data source. The agreement between SCIATRAN and SPURT is rated as very promising.

4.2 Case studies: lightning events

Since the goal of this work is to improve the NO_2 retrieval sensitivity in the UTLS region, a comparison with results from a different work, following similar aims is meaningful. In Sioris *et al.* (2007) a retrieval algorithm is used, which is optimized for UTLS retrievals and described in section 2.4. The focus is to retrieve single profiles for cases with very high local NO_2 values instead of averaging a number of profiles as in the present work.

It is worth to investigate if the improved NO_2 retrieval V3.2 described in the present work is capable of detecting the reported NO_2 enhancements. Due to a relatively coarse vertical resolution of SCIAMACHY no sharp peak restricted to single altitude levels can be detected. One rather expects to obtain NO_2 values which are increased around 12 km altitude when compared to the neighboring measurements.

The obtained results are shown in Fig. 4.15. An NO_2 enhancement around 12 km can be seen in the middle plot (state 26), which is not seen for neighbouring states in the same plot (states 25 and 27, left and right panel). The grey line shows the a priori profile used for this retrieval. Results from the unmodified SCIATRAN NO_2 V3.1 retrieval are shown by black lines. The black NO_2 profile already features larger values in state 26 as compared to the neighbouring states. For the red curve, which is the modified SCIATRAN NO_2 retrieval, the result shows a peak at about 12 km to 13 km. The peak retrieved with the method described in Sioris *et al.* (2007) for the same SCIAMACHY state has a value of about $2 \pm 1.5 * 10^9$ mol./cm^3. It is also important to note, that clouds are detected for this state, but only at 8 to 9 km. As seen in section 3.1.1 clouds can lead to influences on the results even if the cloud is located outside the field of view. Judging from the cloud sensitivity studies, the retrieved NO_2 amount should be slightly smaller than the NO_2 detected in a hypothetical cloud-free scenario. If the focus is on lightning events, a cloud- free scenario is very difficult to obtain.

The satellite based lightning image sensor (LIS) provides a picture of the event from space, see Fig. 4.16. This observation verifies the detection of a lightning event at this location and time.

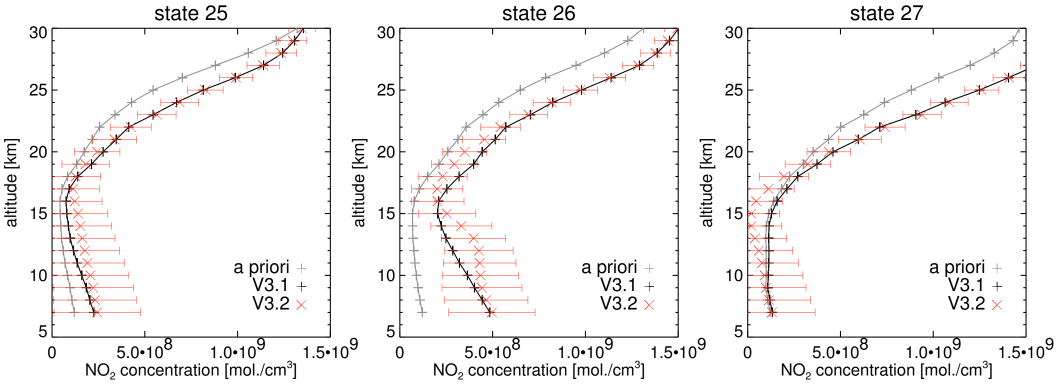

Figure 4.15: This figure shows retrieval results for a lightning event on the 15.03.2005, 26.29° South, 75.11° East, South Indian Ocean. The event is also investigated in Sioris *et al.* (2007).

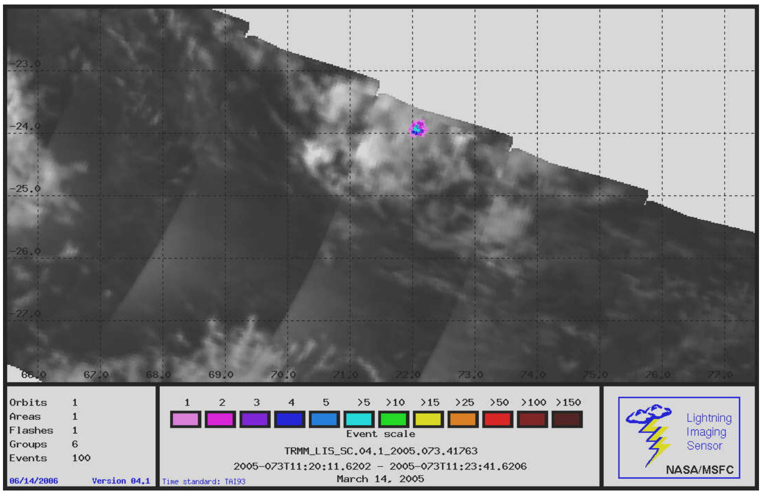

Figure 4.16: This picture has been made using the lightning image sensor (LIS) aboard the TRMM (Tropical Rainfall Mission), NASA. It shows the lightning event from Fig. 4.15.

Although the modified SCIATRAN NO_2 retrieval V3.2 is not optimized for the detection of individual strong NO_2 peaks in single profiles it is capable of detecting the local NO_2 enhancements for the same lightning event as the method described in section 2.4. Although the retrieved value is smaller, the error bars of the retrieval methods are comparably large, so the precise value is difficult to determine.

4.3 Case studies: flight corridors

One of the aims of the present work is the detection of enhanced NO_2 values in the UTLS altitude region. While lightning events, volcanic eruptions and biomass burning events with stratospheric injections are strongly localized sources, there are other emissions responsible for NO_2 enhancements, which are weaker, but more stable. A large number of profiles can be averaged to allow the investigation of enhanced NO_2 concentrations, which are more challenging to detect in single vertical profiles due to measurement errors and retrieval uncertainties.

Using the current product retrieval version of SCIATRAN V3.1 (see section 2.4), SCIAMACHY limb profiles from autumn 2002 to 2007 have been retrieved, which provides a large data source which can be used for averaging of NO_2 profiles. In the context of this work, autumn spans the months September, October and November, known as meteorological autumn. In addition, the improved limb retrieval V3.2 (see section 3.3.2) has been used to generate a data set for a limited time frame and a limited coverage, mainly over the North Atlantic region.

For the averaging approach, in most cases $5^\circ \times 5^\circ$ areas are chosen, and within the selected time frame the profiles with coordinates inside this area are used for arithmetic averaging. If the number of profiles taken into account for averaging inside a chosen area is too small, individual outlying profiles with too high values due to a very large emission source or other reasons can be misleading, especially if other areas provide far more profiles for averaging.

The program code also has the ability to perform cloud masking. Cloud detection results created with the method described in section 2.3 are already included in SCIATRAN NO_2 V3.1 product results.

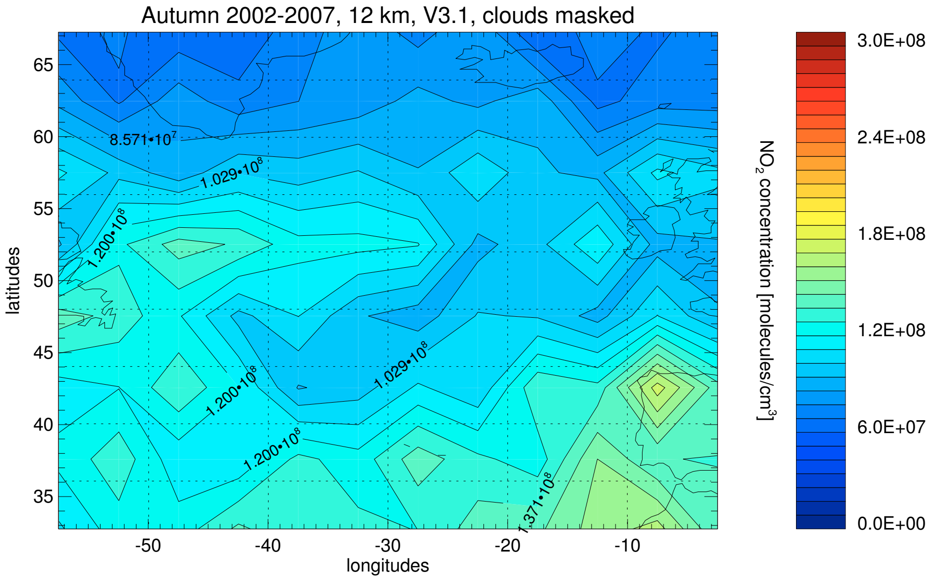

Figure 4.17: This figure shows an area over the North Atlantic Ocean. NO_2 V3.1 retrieval results are shown for an altitude of 12 km, averaged over 5° × 5° areas for meteorological autumn and 2002 to 2007.

Seasonal averages over several years

In the time frame of SCIAMACHY measurements there is no period known, when air traffic was considerably reduced. To obtain the largest possible benefit from the retrieved datasets it is therefore advantageous to average over several years for one season. Since photochemical corrections are not applied to the data set, it is necessary to treat each meteorological season individually, as NO_2 amounts can vary considerably from season to season at the respective time of day of SCIAMACHY overpass.

The results from SCIATRAN NO_2 V3.1 for a selected region over the North Atlantic are seen in Fig. 4.17 for an altitude of 12 km. Profiles for six years are averaged over 5° × 5° bins. Cloud contaminated profiles are not used, so clouds inside the field of view do not change the results, while clouds outside the field of view are not considered by this method.

There is good agreement with the North Atlantic flight corridor in Fig. 2.7, which shows flight corridors based on fuel consumption by airplanes. The area of interest is the latitude range from about 50° to 55° North. From the results of section 3.3.1 it

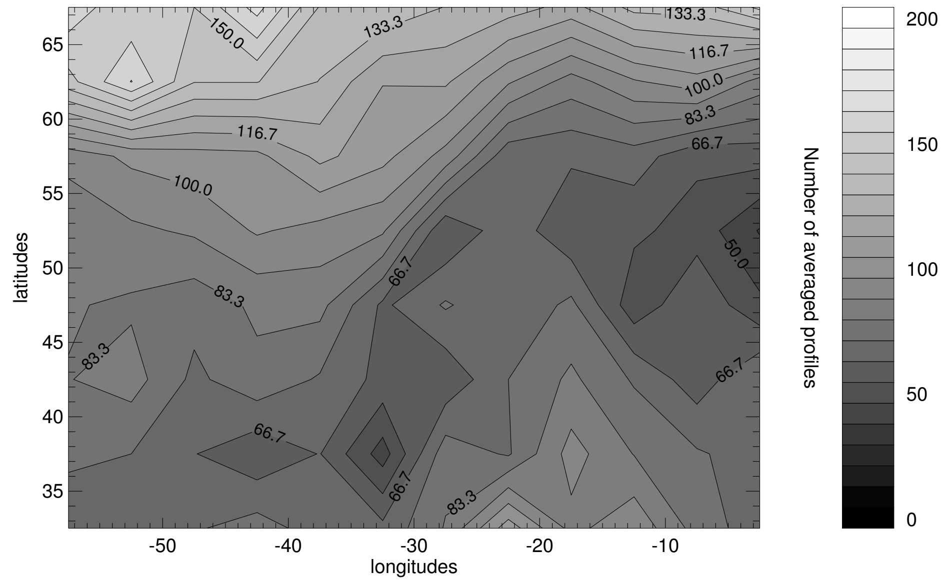

Figure 4.18: The number of averaged profiles for each 5° × 5° area used in Fig. 4.17 are shown here. The number of averaged profiles varies from about 60 to above 200. A grey scale is chosen to avoid confusion with measurement results.

can be estimated, that airplane emissions should be detected as an increase of about $1.0*10^8$ mol./cm^3. The enhancements seen in Fig. 4.17 are of the same order of magnitude.

In order to investigate if the pattern is related to the number of averaged profiles, another plot is created (see Fig. 4.18). The patterns in this contour plot and in Fig. 4.17 do not correlate, indicating that there is no such relation. The analysis of the averaged number of profiles is more important when only a monthly mean or a seasonal mean for only one year is considered.

One data source is available for comparisons. The global-coupled chemistry-transport model EMAC provides the necessary information, see section 2.5.6 for a description. Instead of performing photochemical corrections, model output was selected for the 9-12 hour time period, overlapping the ENVISAT overpass times of about 10 - 12h. Results for the North Atlantic region for the 1st September to 31st December in 2003 are shown in Fig. 4.19. There is a difference of one month as compared to the satellite data analysis, since the meteorological autumn was considered for Fig. 4.17, which includes the months from September to November, but not December.

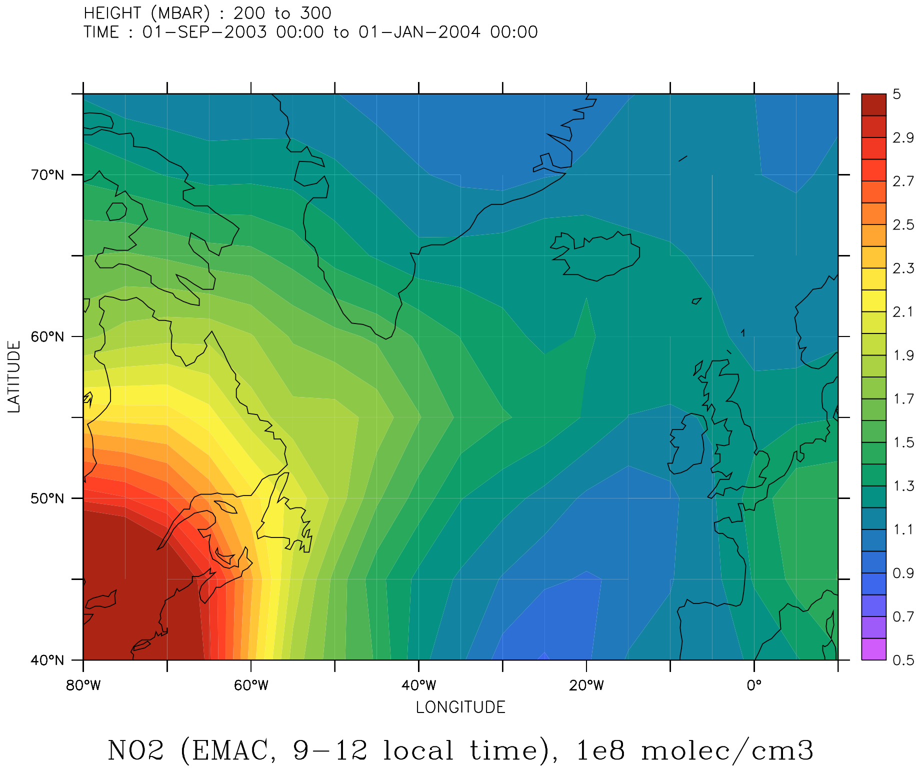

Figure 4.19: Simulated NO_2 concentrations for 2003, 1st September to 31th December, EMAC (see section 2.5.6). For comparisons with Fig. 4.17 consider the different longitudinal coverages. Figure provided by Peter Hoor, personal communication

A similar pattern as in Fig. 4.17 is seen in the model results (Figure 4.19), and also the longitudinal gradient is visible in Figure 4.19. In both cases there is a tendency for higher NO_2 values in the West. The model simulations provide the additional opportunity to investigate the contribution from airplane by emissions by using several model runs, in which the amount of airplane emissions is changed. The result is displayed in Figure 4.20.

In the model, the contribution from airplane emissions is highest in the Eastern part of the flight corridor, while different sources are responsible for the comparably high NO_2 values in the West. Another possible explanation for the longitudinal gradient can be related to flight altitudes. As seen for the CARIBIC experiment, flight altitudes change depending on the flight direction. In flights with the CARIBIC experiment the airplanes remained between 11 km and 12 km flight altitude, while flying over the North Atlantic from West to East, see Fig. 2.17. However, in flights from East

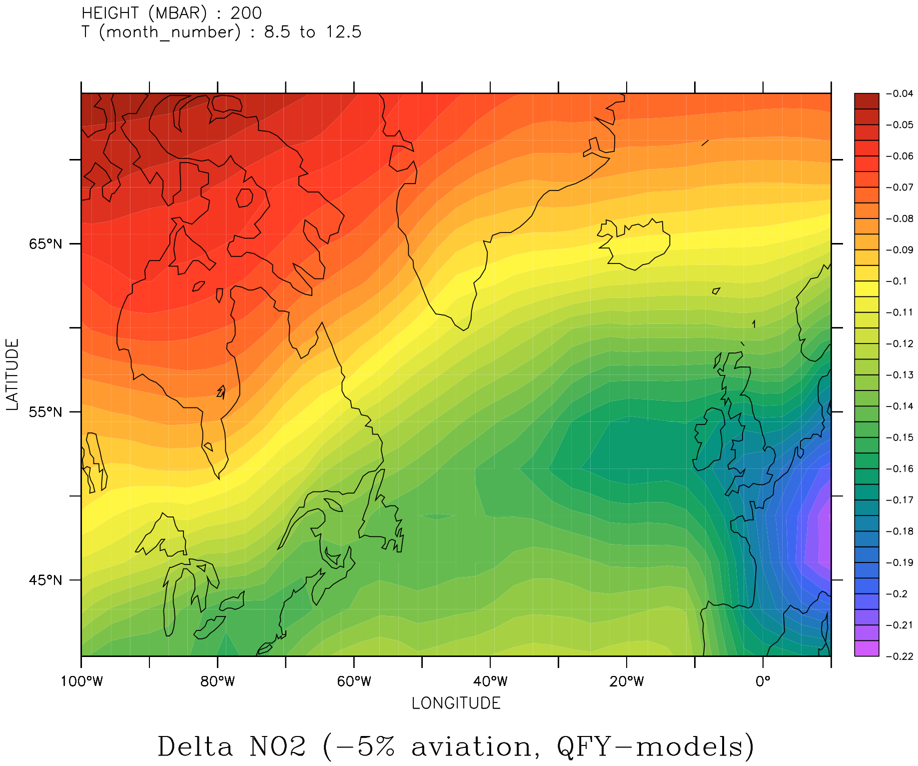

Figure 4.20: Simulated influence from aviation using the EMAC framework, see section 2.5.6. The covered area is similar to Fig. 4.19, but starts at 100° West. Two model runs were created, one with full consideration of aviation emissions and a second one where the simulated aviation emissions were reduced by 5%. This plot shows the difference between the two cases in 10^8 molec./cm^3. Figure provided by Peter Hoor, personal communication

to West, the airplanes changed their flight altitude along the flight track. Only some of them flew in this altitude range west of 40°W. Considering the model results from Fig. 4.20 this explanation might not be sufficient and other emission sources seem to be responsible for the gradient, as the contribution from airplanes is weaker in the West in the model results. In regions with high emissions for example, it is possible that emissions reach the lower stratosphere under certain conditions, as has been shown in Stohl *et al.* (2003). Still, the agreement between model results and retrieved NO_2 results is very promising.

In section 2.1, the Noxon cliff is mentioned, which can basically be seen as a very strong NO_2 gradient at latitudes around 40°N to 45°N. It is however unlikely, that the North Atlantic flight corridor is simply the Noxon cliff. Firstly, there is a steep gradient at 40°N to 45° N in figure 4.17, which might be related to the Noxon cliff, and the pattern in the North Atlantic flight corridor is seen at latitudes about 50°N to 55°N. Secondly, the Noxon cliff is most prominent the in the winter season, while here autumn conditions are discussed. And thirdly, as mentioned in Wenig *et al.* (2004), the Noxon cliff is most distinct over continents, while here measurement over the North Atlantic region are investigated here. Although the last point is arguable, as only the lower part of the stratosphere is subject to the investigation here, it is unlikely, that the enhanced NO_2 pattern between 50°N to 55°N in Figure 4.17 is resulting from the Noxon cliff.

Influence of cloud masking

From the simulations discussed in section 3.1.1, which give an estimate for the influence of clouds on the retrieval results, it is expected that clouds in the field of view lead to reduced values in the retrieved NO_2 profiles. However, some NO_2 sources such as airplanes (contrails) and lightning are linked to clouds. Therefore it is not clear, if cloud masking leads to increased NO_2 values in an averaged plot. Two averaged data sets are now compared. The only difference is the cloud masking feature, which is applied in one case, but is switched off in the second case. For simplicity, the scenario from Fig. 4.17 is chosen, as it has already been discussed. The corresponding results without cloud masking are shown in Fig. 4.21.

The general patterns and NO_2 structures do not vanish, when cloud contaminated profiles are included. The main difference between both figures are the detected NO_2 amounts. The maximum close to Spain as well as the values in the flight corridor are lower. This is consistent with the expectations from section 3.1.1, where all simulations with different cloud scenarios resulted in lower NO_2 values in the UTLS region. The difference between the two figures can be seen in Figure 4.22.

In order to investigate, if more clouds are detected in certain areas, Figures 4.18 and 4.23 are compared. More than half the available profiles are usually discarded by cloud masking, and the southern parts seem to be more affected by cloud masking.

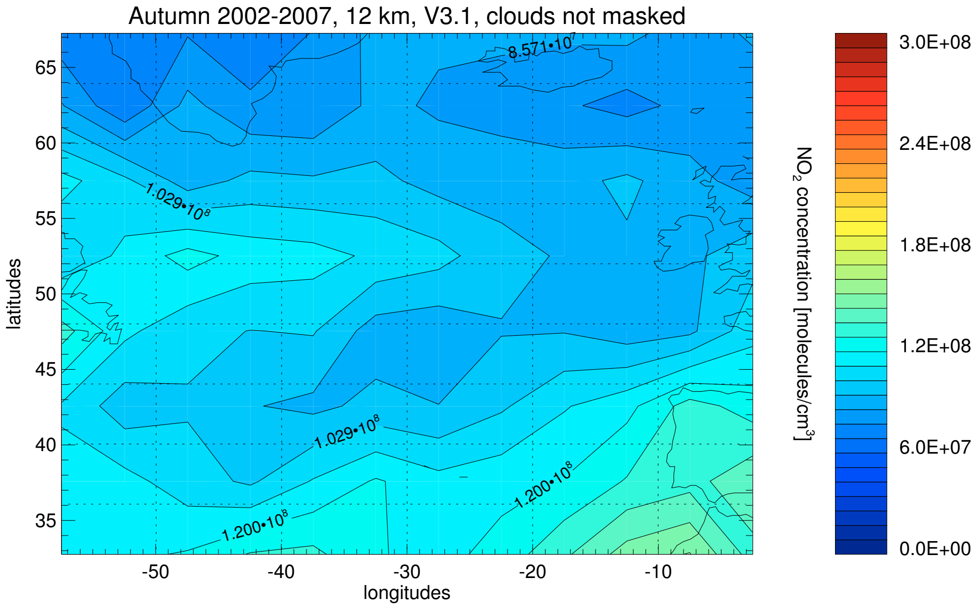

Figure 4.21: The conditions (coordinates, retrieval settings, time frame) are identical to Fig. 4.17. The only difference is the cloud masking, which has been switched off.

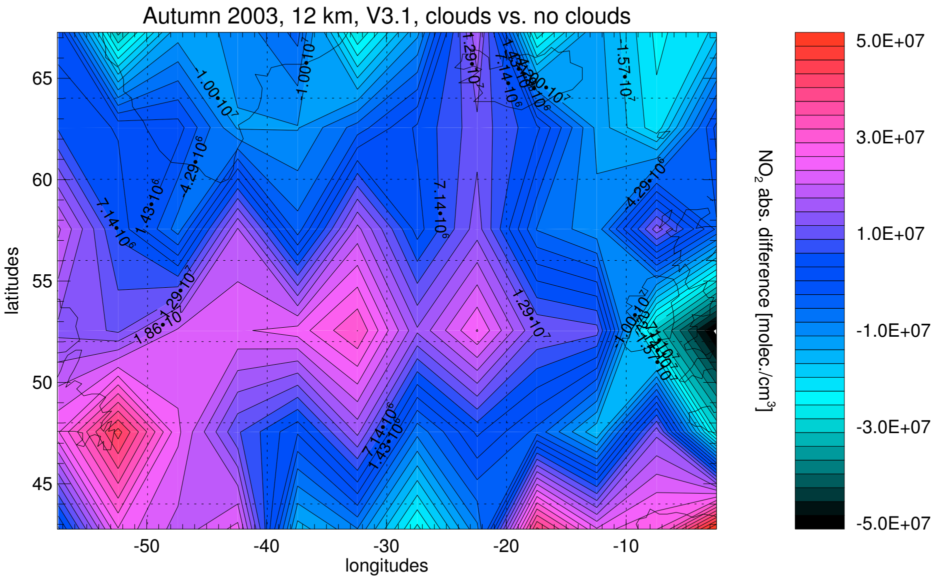

Figure 4.22: The absolute difference between NO_2 amounts from Figure 4.17 and 4.21 is plotted, i.e. averaged NO_2 profiles with cloud masking applied minus the averaged NO_2 profiles without cloud masking

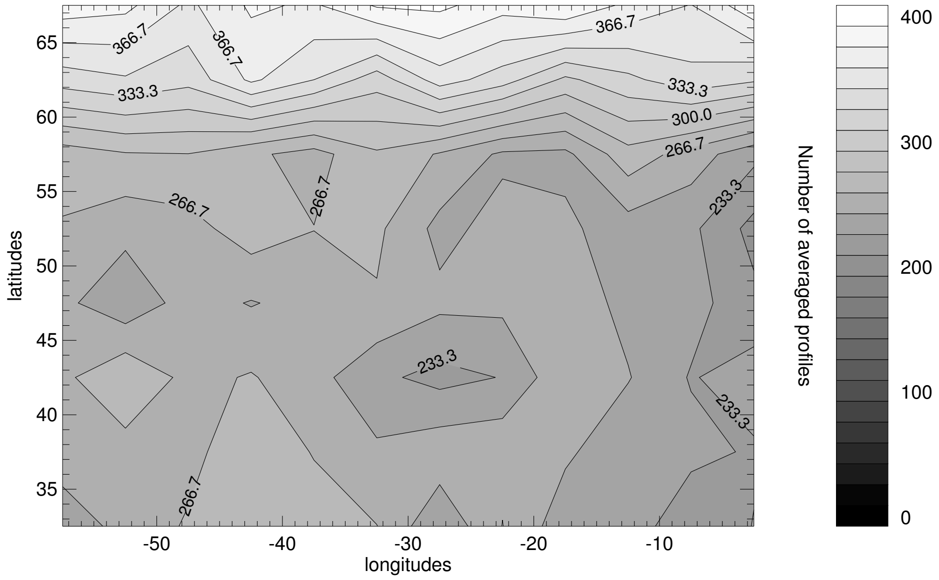

Figure 4.23: The number of averaged profiles for each 5° × 5° area in this figure are higher than those in Fig. 4.18, where cloud masking is applied. About half the profiles were discarded, so the color bar reaches up to 400 averaged profiles in this case.

Comparison of averaged plots for different seasons

Similar to Figure 4.17, an average plot for the years 2003 to 2006 for spring is presented in Figure 4.24 including the months March, April, and May. The results are considerably different compared to the autumn season. This is expected because of different photochemical conditions and other seasonal differences. Compared to Fig. 4.17, the color bar is adjusted to $9 * 10^8$ mol./cm^3 from $3 * 10^8$ mol./cm^3. For this figure 13,152 profiles were available, and 6,743 have been discarded due to cloud masking.

A very strong latitudinal gradient is revealed, which is not seen for Autumn in the same order of magnitude. To investigate this more closely, a vertical plot is created, in which the profiles for all longitudes are averaged in 5° latitudinal steps, so that the average vertical profile for a certain latitude band can be displayed, see Fig. 4.25.

The latitudinal gradient is not related to a phenomenon restricted to the the UTLS region. Values greater than $1 * 10^9$ mol./cm^3 reach down to lower altitude region at latitudes north of 60°N, with a value greater than $5 * 10^8$ mol./cm^3 at 15 km at a latitude of 65°N. Applying latitudinal cross sections to the averaged plots in Fig. 4.26, the gradient becomes visible and in addition, the NO_2 enhancement in the flight corridor

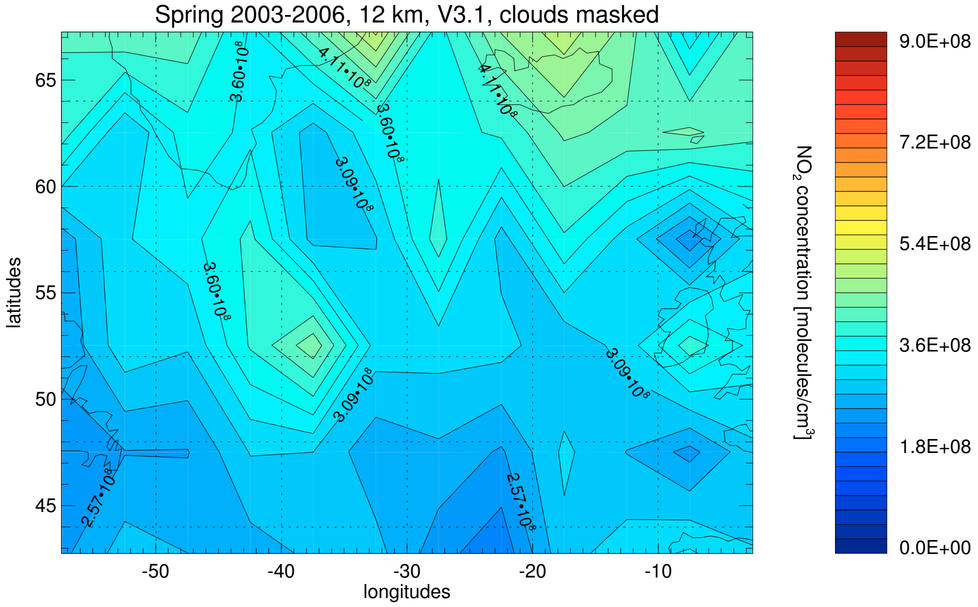

Figure 4.24: This plot shows averaged profiles for an altitude of 12 km for the years 2003 to 2006 for the months March, April and May. Cloud masking is applied, and the settings are otherwise identical to Fig. 4.18.

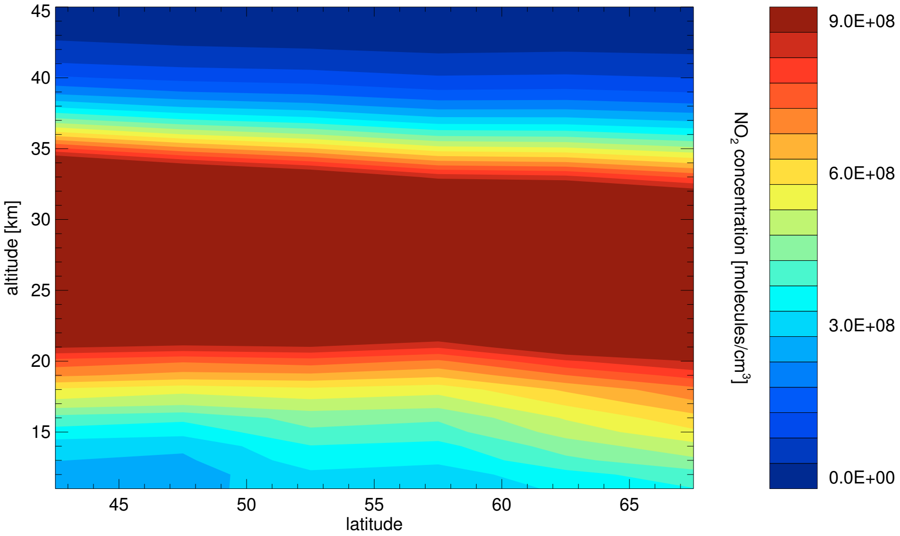

Figure 4.25: For each 5° latitude bin all profiles in the longitude range 60° West to 0° West are averaged and the vertical NO_2 profiles are plotted. All Spring seasons are included for the years 2003 to 2006.

around 50 to 55°N is also recognizable as a small peak. This peak is in the right order of magnitude, as a $1 * 10^8$ mol./cm^3 enhancement is expected from sensitivity studies.

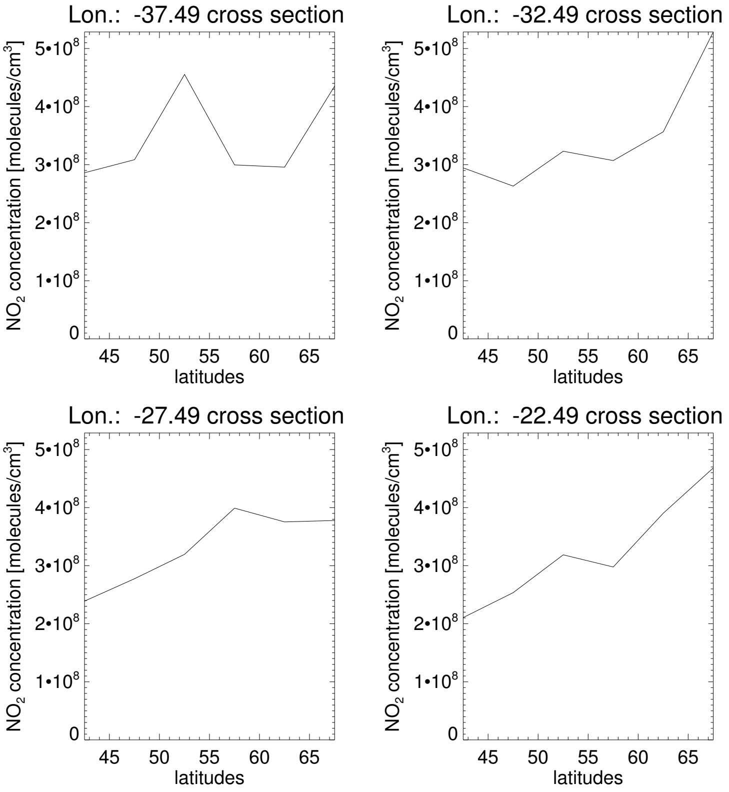

Figure 4.26: The NO_2 spring time average conditions are plotted vs. latitude for four selected longitude bins to investigate the latitudinal gradient.

In order to discuss all seasons, winter and summer also need to be investigated with the same methods. Meteorological Winter (December, January and February) averaged for the years 2002 to 2006 exhibits the lowest overall NO_2 values at 12 km, with no averaged bin having a value larger than $1 * 10^8$ mol./cm^3, as seen in Fig. 4.27. In total, 8353 out of 17768 have been discarded by cloud masking.

Low values are not only retrieved near the tropopause height, as can be seen in Fig. 4.28. The profiles are of smaller overall magnitude compared to other seasons. There is no reason to assume lower emissions from anthropogenic sources in the Winter season.

The differences from season to season are significant. As mentioned in section 2.1,

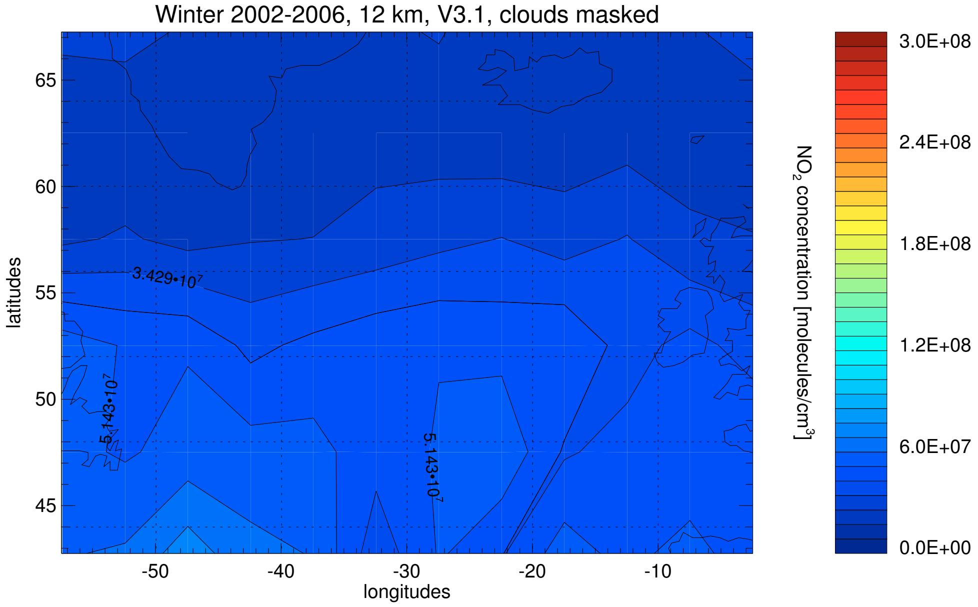

Figure 4.27: This plot shows averaged NO_2 amounts at an altitude of 12 km for the meteorological winter of the years 2002 to 2006. Cloud masking is applied, and the settings are otherwise identical to Fig. 4.17.

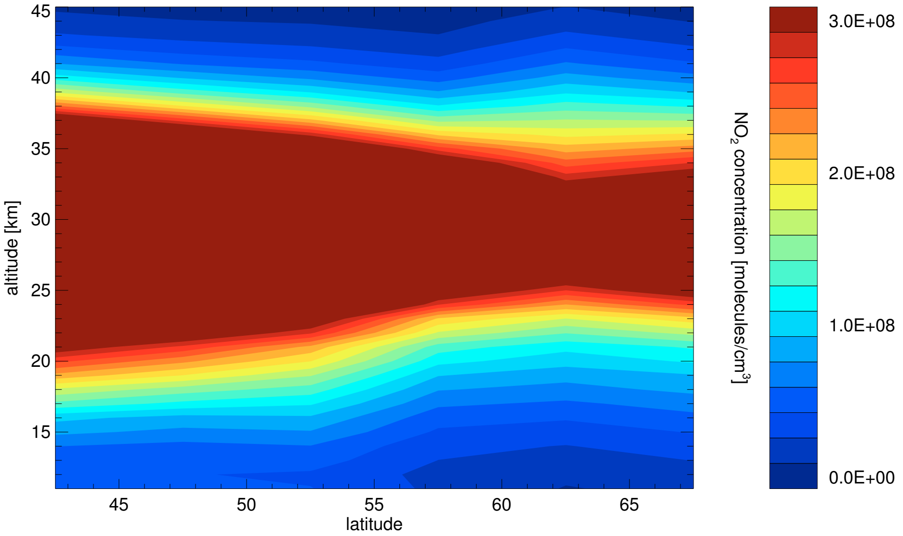

Figure 4.28: For each 5° latitude bin all profiles in the longitude range 60° W to 0° W are averaged and the vertical NO_2 profiles are plotted. All Winter seasons are covered for the years 2002 to 2006.

the chemistry and dynamics leading to this variation is basically taking place in the lower stratosphere. Enhanced NO_2 levels at higher latitudes during summer are expected, as well as very low NO_2 levels in winter.

As seen in Fig. 3.14, with a background of lower NO_2 amounts an enhancement of NO_2 from anthropogenic sources (e.g., airplanes, stratospheric injection) should be easier to detect. This is, however, not the case in the winter results (Figure 4.27). The explanation is, that this NO_2 from local anthropogenic sources is exposed to the same conditions and reactions, that lead to the small background NO_2 levels in the stratosphere. Under the conditions of short sunlight periods, long nights and low temperatures, the NO_2 is converted to reservoir species during the night (N_2O_5). NO_2 is thus more difficult to detect, because it is not accumulated as in other seasons.

There are further reasons for the low values. One aspect to consider again is the influence of clouds, as mentioned in section 3.1.1. While measurements with clouds in the field of view are sorted out, clouds below the field of view still have a significant influence and lead to reduced NO_2 amounts. This influence is dependent on the SZA, and the SZA is different for typical measurements from season to season. While in a summer scenario, e.g., an SZA of 35° is common, the SZA can be 70° for the same region and the same daytime in winter. As a consequence, clouds have more significant influence in winter.

It is not expected, that anthropogenic emissions are lower in winter season, but a tropopause height shifted downwards might also contribute to lower NO_2 values in winter. In that case, anthropogenic emissions could be outside the sensitivity range. The tropopause height can be determined from temperature profiles from ECMWF data sets (i.e., the same dataset as used in section 3.2.2). For comparison, tropopause heights from a $1.5° \times 1.5°$-grid are averaged for a selected region. For 2003 and the 3 months each of meteorological winter and autumn, the monthly averaged tropopause height is shown in Table 4.7 for the North Atlantic region covered by Fig. 4.27. Values smaller than 7 km and higher than 15 km are not considered. The average tropopause height for the winter months (December, January and February) is 10.7 km. In autumn (September, October and November) it is higher with 11.2 km. The tropopause height is variable in time and region. For many days the standard deviation for the average over the region is larger than 2 km. The tropopause height also changes with time, and the deviation for the monthly means is also significant (see Table 4.7). This seasonal

month	averaged tropopause height [km]	standard deviation [km]
December	11.0	0.4
January	10.8	0.6
February	10.4	0.5
September	11.5	0.4
October	11.4	0.4
November	10.6	0.4

Table 4.7: Averaged tropopause heights for the year 2003 and the region from 40° N to 70° N and 60° W to the Prime Meridian at 0°.

change in tropopause altitude helps to understand lower NO_2 values in winter, as NO_2 concentrations from the troposphere are less likely to reach higher altitudes.

All in all, the first explanation (denoxification) is the most important for the disappearance of the pattern of enhanced NO_2 in the flight corridor in the winter season.

In summer, the NO_2 values are highest. Although the maximum NO_2 amounts are larger than $9 * 10^8$ mol./cm^3 (Fig. 4.29), this values is used as a maximum in order to use the same scale as for spring, see Fig. 4.24. Due to the steeper latitudinal NO_2 gradient, enhanced NO_2 levels from anthropogenic emissions are difficult to detect.

The seasonal comparisons show, that a strong variation can be seen in NO_2. It is therefore difficult to compare results from different seasons and thus important to investigate the averaged NO_2 amounts for single seasons separately. This proves to be a promising field for photochemistry corrections. A sufficiently well tested algorithm suitable for the tropopause region should be used to allow a comparison of different seasons and to give a realistic estimation of the NO_x concentrations.

North Atlantic region investigated using SCIATRAN version V3.2 improved for UTLS

The Autumn season in 2003 and the North Atlantic altitude region are selected for retrievals with the improved SCIATRAN version V3.1 described in section 3.3. The profiles are averaged using the same latitude/longitude-grid as before in section 4.3. For comparison, the same area and time frame is considered for both, the improved version V3.2 and for SCIATRAN NO_2 version V3.1. Overall, 1321 of 3213 profiles

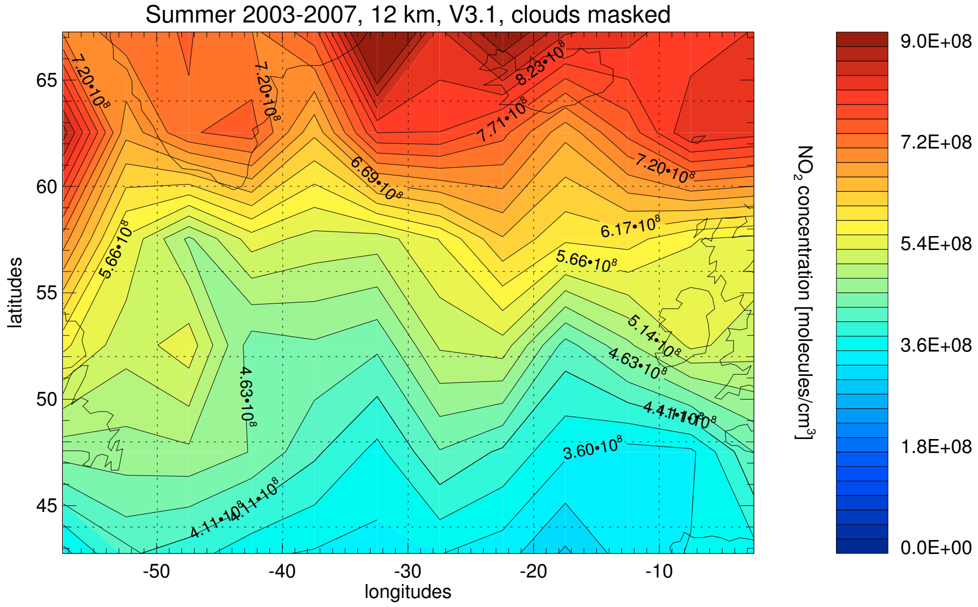

Figure 4.29: This plot shows averaged profiles for an altitude of 12 km for the summer of the years 2003 to 2007. Cloud masking is applied, and the settings are otherwise identical to Fig. 4.18.

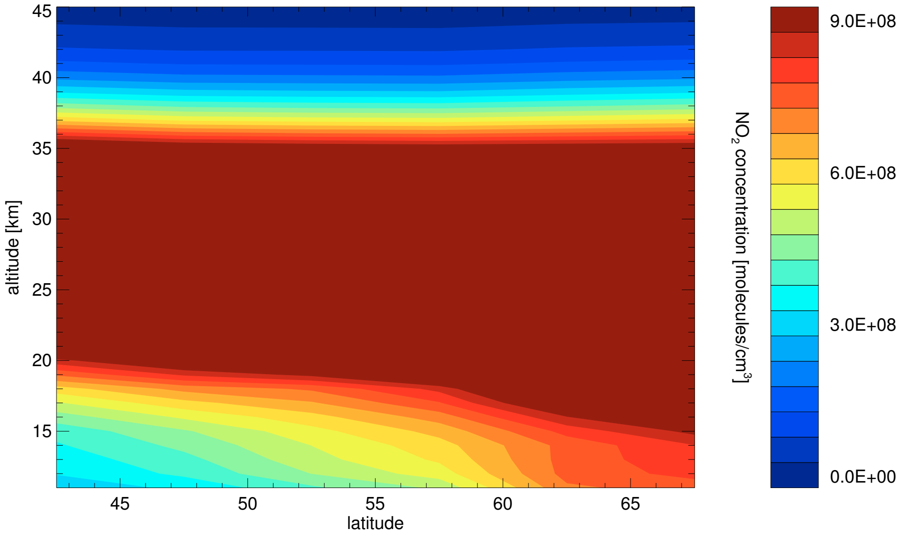

Figure 4.30: For each 5° latitude bin all profiles in the longitude range 60° West to 0° West are averaged and the vertical NO$_2$ profiles are plotted. All Summer seasons are covered for the years 2003 to 2007.

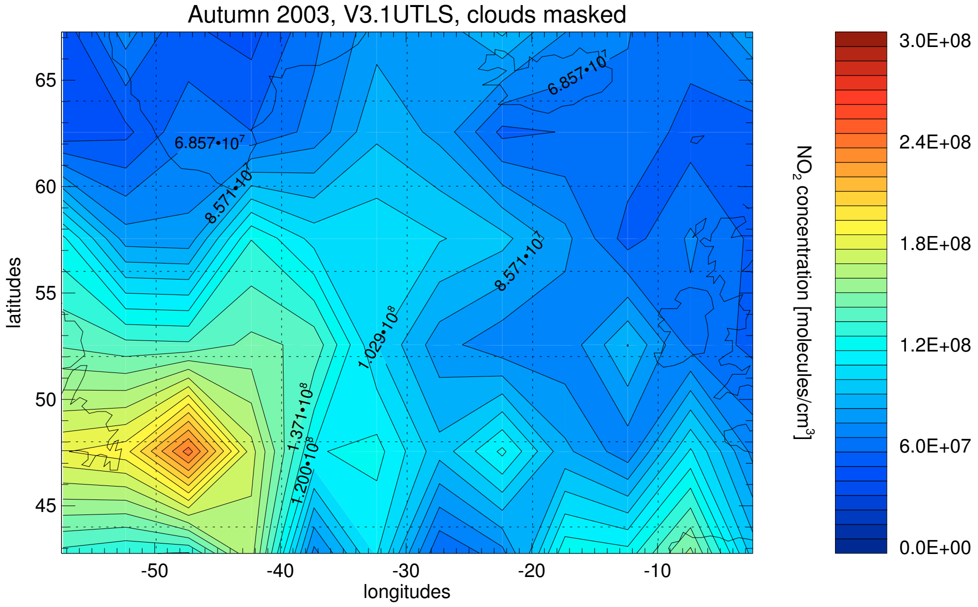

Figure 4.31: In 5° × 5° bins NO_2 profiles are averaged and the result is shown for the altitude of 12 km. Compared to Fig. 4.17 the time range is restricted. Only profiles from Autumn 2003 are considered. The NO_2 profiles are retrieved using the modified version V3.2 from section 3.3.

are discarded due to cloud contamination. The results are shown in Fig. 4.31 for the modified SCIATRAN V3.2 and in Fig. 4.32 for the standard NO_2 V3.1 retrieval.

Compared to Fig. 4.17 the resulting structures of enhanced NO_2 are quite different. The reason for this is the difference in the time frame used for averaging. For Figure 4.17, three months (meteorological autumn) for six years (2002 to 2007) are used for averaging, while the time frame is restricted to the same three months of only one year (2003) in Figures 4.31 and 4.32. Short-lived structures in NO_2 concentrations that are lost in the multi-year averages are preserved here, but NO_2 concentration changes which are present regardless of the investigated year are more difficult to detect in data of a single year than in longer-term averages.

The modified version results show higher NO_2 values in many cases, but also lower values are found occasionally. There are some differences in the spatial structures of enhanced NO_2, e.g. a new peak at about 47.5° N and 32.5° W, that is not seen in Fig. 4.32. The maximum value at about 47.5° N and 47.5° W is the maximum in both figures, but it is also linked to an area, where only nine profiles are available for

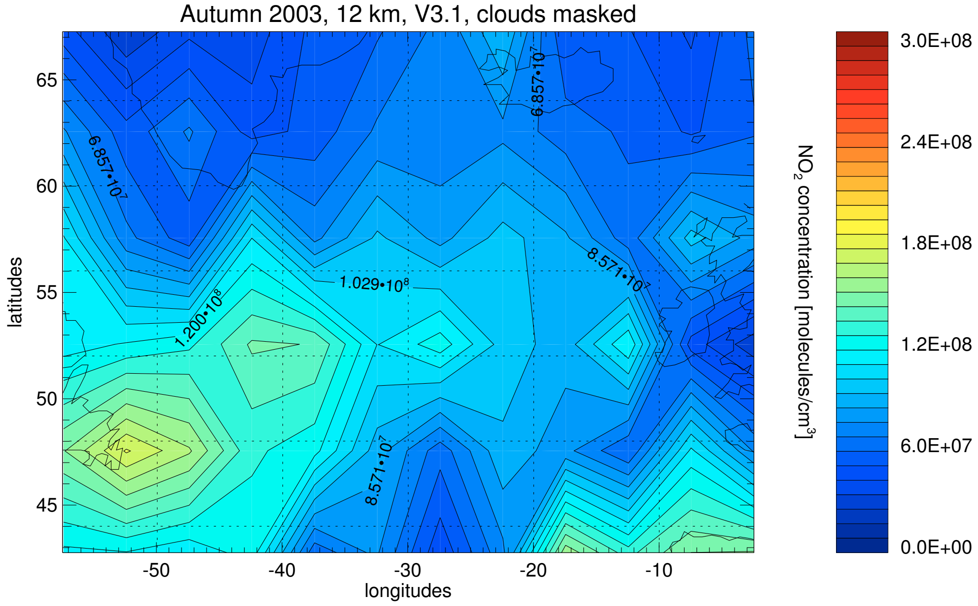

Figure 4.32: The same time frame and region is investigated as in Fig. 4.31. For this figure SCIATRAN NO_2 version 3.1 retrievals are used for averaging.

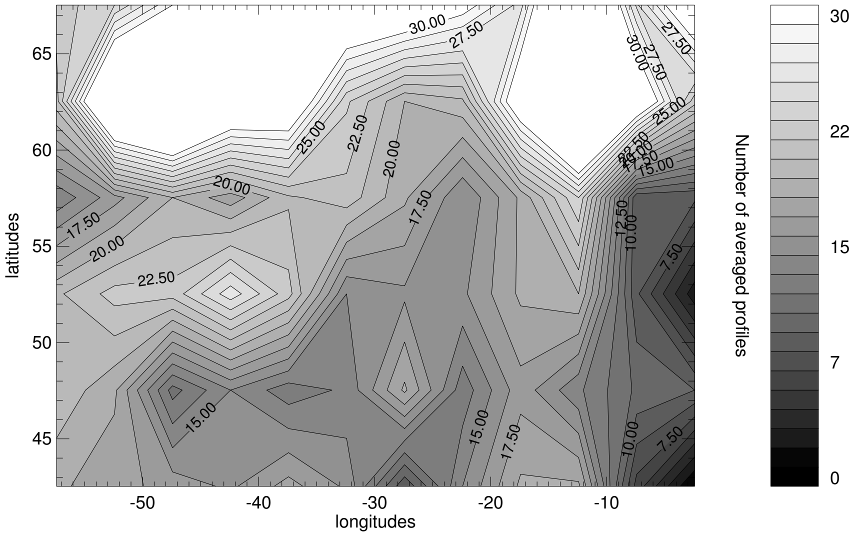

Figure 4.33: Number of averaged profiles for each 5° × 5° bin. This plot is valid for both Fig. 4.31 and Fig. 4.32.

averaging, see Fig. 4.33. One can conclude from these figures, that the local maximum is linked to a local minimum in the number of averaged profiles. Single profiles have more influence in that case. The retrieved highest single NO_2 value for the 12 km altitude of $6.1 * 10^8$ mol./cm^3 is also detected at this location.

Except for this example, the number of averaged plots is generally high enough with only one outlier of only five averaged profiles at the South-East corner of the plot. The comparison of Figures 4.31 and 4.32 shows, that the new version leads to qualitative and quantitative relevant changes, while still maintaining the general spatial pattern seen by the standard NO_2 retrieval. An investigation using a longer time frame and/or different regions is recommended. Fig. 4.31 shows a strong emphasis on the lower latitude, lower longitude quarter close to the North American continent. It is also worth to note, that the V3.1 NO_2 pattern seen here matches the modelled NO_2 amounts (Fig. 4.19) more closely, as it is the case for Figure 4.32.

5

Conclusion

In the present work numerous studies on the quality of SCIAMACHY NO_2 retrievals are performed, and methods to improve the sensitivity of NO_2 retrievals in the UTLS altitude region for limb viewing geometry are investigated and applied.

The performance of the modified retrieval approach as well as of the unmodified SCIATRAN NO_2 limb retrieval is studied in detail. Applying a photochemical correction, thousands of NO_2 profiles from three solar occultation instruments are compared with SCIATRAN NO_2 in a sophisticated validation effort. Other validation sources are investigated as well. In addition, sensitivity studies including clouds, aerosols and pointing errors are performed. Furthermore, the modification to the current SCIATRAN NO_2 limb retrieval is described, which is developed to improve the NO_2 sensitivity in the UTLS. Compared to current retrieval approaches the idea to use an additional spectral range to improve the sensitivity specifically for the UTLS region is novel. The influence of clouds in the field of view is studied by synthetic retrievals and a cloud detection algorithm is available to discard scenes with a significant cloud contamination. Case studies are performed to investigate NO_2 concentrations in the UTLS region. In the following, the individual parts of this study are summarized.

Before the validation efforts and improvements are discussed, the sensitivity of NO_2 retrievals with respect to different error sources is considered. Using synthetic retrievals, the influence of several cloud types, aerosol loadings and pointing uncertainties on the retrieved NO_2 profiles is investigated.

Regarding aerosols, the synthetic NO_2 retrievals lead to considerably reduced NO_2 amounts below 25 km in both the 'aged medium volcanic activity' and 'fresh high volcanic activity'-LOWTRAN-scenarios. It is also shown, that the estimated pointing uncertainty of ± 200 m does not lead to significant relative differences in NO_2 amounts, if the NO_2 levels are not too low.

In all investigated scenarios the existence of clouds in the field of view results in reduced NO_2 amounts in limb geometry. The altitude dependence is small, i.e., even clouds at altitudes below 10 km have an influence on the NO_2 profile at 20 km in some scenarios. The cloud influence varies and can result in a 60% reduction of the NO_2 values for some SZA and cloud thickness settings. Using these results and additional simulations for different SZAs the cloud sensitivity can be estimated and together with a sophisticated cloud retrieval algorithm, cloud correction instead of cloud-masking might be feasible. Cloud-masking includes only clouds inside the field-of-view of the instrument. As the sensitivity studies show, clouds outside the field-of-view also have a small influence on the retrieved NO_2 profiles, and those clouds can not be identified easily using the SCODA algorithm (Eichmann *et al.* (2009)).

This leads to three conclusions: The profile should be masked even if the detected cloud is several kilometres below the investigated altitude. Cloud masking cannot yield results completely free of cloud-contamination, because even clouds at lower altitudes outside the field-of-view have an influence on the NO_2 values. Assuming unchanged NO_2 values in the investigated scenario cloud-masking will lead to higher averaged values, because the cloud-contaminated NO_2 amounts are usually too low.

For the validation of retrieved NO_2 profiles an array of different data sources is used. Balloon-borne measurements and two instruments installed on aircrafts yield NO_2 profiles or NO_2 amounts in the UTLS of different quality and resolution, forming a well-defined basis for validation. Generally, the conclusion drawn from these comparisons is that the agreement with both retrieval setups is quite good in the number of comparisons are available. The main difference between the SCIAMACHY NO_2 limb retrieval and the modified retrieval algorithm is usually not the retrieved profile, but the improved theoretical precisions in many cases, indicating more reliable NO_2 profiles. For the validation effort, an algorithm was implemented, which is able to correct the differences in NO_2, that originate from the strong diurnal cycle of NO_2. The performance of this algorithm is also investigated.

The current product version of SCIAMACHY NO_2 limb was validated in detail using three solar occultation instruments, namely SAGE II, HALOE and ACE-FTS. All available collocations within two years for each instrument, are taken into account and several latitudinal regions are investigated in detail for each season. If the altitude range in the comparison is restricted to 20 to 40 km, mean relative differences between SCIAMACHY and the other solar occultation instruments are found to be within 20% to 30%. Mean partial NO_2 columns agree typically within 15% for either global seasonal means or zonal yearly means. Larger differences are seen for SAGE II, which agrees with results presented by other authors. Furthermore, the influence from the diurnal effect error is investigated, which originates from the changing SZA along the line of sight during a measurement. This effect can be corrected for several latitude regions, and the correction leads to improved agreements at lower altitudes (below 25 km) with the exception of SAGE II sunrise measurements. However, SAGE II sunrise NO_2 amounts were reported to be less reliable and show a significant bias in several validation studies. It should be noted, that cloud masking is not applied for this part of the validation, as the influence on altitudes above 20 km is considered to be low. Below 20 km, the quality of NO_2 profiles from solar occultation instruments declines and should not be used for validation. The loss of two thirds of collocation pairs would offset the gain from cloud-masking.

From the possible improvements for the retrieval process, the utilization of additional spectral region proved to be the most promising approach to enhance the sensitivity for the UTLS altitude range. For most altitudes, the optimal spectral region is in the short-wavelength part of the visible range, as the NO_2 cross section is larger. A spectral range somewhere between 420 nm and 470 nm is regarded as optimal for the retrieval of NO_2 and used in several retrieval methods (Puķīte *et al.*, 2008; Rozanov *et al.*, 2005; Sioris *et al.*, 2007). However, towards the tropopause, absorption and scattering in the atmosphere emerges as a wavelength dependent problem, i.e., longer wavelengths are generally less affected by these retrieval difficulties.

Therefore, the suggested improved retrieval setup is divided into two parts. The first step is the current SCIATRAN NO_2 limb retrieval. The results from the first step are used as a priori profiles for the modified SCIATRAN setup, which combines the retrieval on the 420 nm and 470 nm spectral region with the additional 520 nm to 560 nm region. By setting strict constraints, the good retrieval results from the standard NO_2

retrieval in the 20 to 40 km altitude region are conserved. In the UTLS region, the constraints are less strict, allowing the advantages of the two-spectral-region setup to yield results with better sensitivity. This method is helpful with respect to the problem of light-scattering, which results from the long light paths in the atmosphere for limb retrievals in lower altitudes.

Finally, the improved method and its predecessor is used for case studies. The first case study is the detection of lightning events. Lightning events exhibit large and very localized NO_2 concentrations. The detection of an enhanced NO_2 value seen as a local maximum in a single vertical profile proves to be possible. This shows the capabilities of the modified approach,as the lightning event can not be observed in the NO_2 result from the standard retrieval.

In the second case study instead of investigating isolated profiles, large numbers of profiles are averaged to generate a complete overview of the North Atlantic region. Averaging helps to improve the comparably high uncertainties of the single profiles at the UTLS region and also reduces the influence of singular events. For example, a local series of lightning events is deemphasized in a multi-year average, if these lightning events do not occur in all years or at the same position. Industrial emissions injected to the stratosphere or emissions from airplanes are present in all years investigated by SCIAMACHY and will not be smoothed out. Due to the strong seasonal variation of NO_2 the averages are performed for each season separately resulting in quantitatively different overview plots. Regarding cloud-masking, the influence of clouds meets the expectations from cloud sensitivity studies.

Enhanced NO_2 values in the North Atlantic region are seen for most seasons and the influences of different sources, mainly industrial emissions transported to the UTLS region, airplane emissions and lightning events on the NO_2 pattern are discussed. A comparison of the SCIATRAN NO_2 retrievals with model results reveals a striking similarity in NO_2 patterns.

The present study improves the understanding of NO_2 in the UTLS region and also investigates the quality of current NO_2 limb retrieval in detail. The influence of several important error sources is discussed and in a vast validation effort the comparison with thousands of solar occultation NO_2 profiles is performed. A new approach for the NO_2 retrieval is presented, which improves the retrieval process specifically for the

UTLS altitude region. In particular, large data sets are studied for the North Atlantic region, which reveal NO_2 concentration patterns very similar to results from a global chemistry model. With the help of these results, the knowledge gap between NO_2 in the troposphere and NO_2 in the stratosphere can be closed.

Glossary

AMF	air mass factors
CARIBIC	Civil Aircraft for the regular investigation of the atmosphere based on an instrumented container, see Brenninkmeijer *et al.* (2007)
DOAS	Differential optical absorption spectroscopy, see Platt (1994)
ECHAM5	5th generation European Centre Hamburg general circulation model, adapted in EMAC
ECMWF	European center for medium-range weather forcast
EMAC	ECHAM5/MESSy Atmospheric Chemistry model
ENVISAT	Environmental Satellite; Earth-observing satellite built by the European Space Agency (ESA), see section 2.2
HALOE	Halogen Occultation Experiment, instrument onboard UARS
LPMA	Limb Profile Monitor of the Atmosphere
MESSy	Modular Earth Submodel System, part of EMAC
OSIRIS	Optical Spectrograph and InfraRed Imager System: satellite instrument onboard the research satellite Odin, see Llewellyn *et al.* (2004)
PSC	polar stratospheric cloud
SCD	slant column densities

SCIAMACHY	Scanning Imaging Absorption Spectrometer for Atmospheric CHartographY; One of the ten instruments aboard ENVISAT, see section 2.2
SCIATRAN	Radiative transfer model and retrieval algorithm, see section 2.4. More information can be found in Rozanov (2012).
SCODA	SCIAMACHY Cloud Detection Algorithm from Limb Radiance Measurements, see section 2.3
SPURT	german: Spurenstofftransport in der Tropopausenregion, trace gas transport in the tropopause region, see Engel *et al.* (2006)
TH	tangent height
TRADEOFF	EU project *Aircraft emissions: contribution of different climate components to changes in radiative forcing - TRADEOFF to reduce atmospheric impact*, see Gauss *et al.* (2006)
UARS	Upper Atmosphere Reseach Satellite; Earth-observing satellite built by National Space Agency (NASA)
UTLS	Upper troposphere/ lower stratosphere altitude region

References

BACKUS, G. & GILBERT, F. (1970). Uniqueness in the inversion of inaccurate gross earth data. *Philosophical Transactions of the Royal Society of London. Series A, Mathematical and Physical Sciences*, **266**, 123–192.

BAUER, R., ROZANOV, A., MCLINDEN, C.A., GORDLEY, L.L., LOTZ, W., RUSSELL III, J.M., WALKER, K.A., ZAWODNY, J.M., LADSTÄTTER-WEISSENMAYER, A., BOVENSMANN, H. & BURROWS, J.P. (2011). Validation of SCIAMACHY limb NO_2 profiles using solar occultation measurements. *Atmospheric Measurement Techniques Discussions*, **4**, 4753–4800.

BERNATH, P.F., MCELROY, C.T., ABRAMS, M.C., BOONE, C.D., BUTLER, M., CAMY-PEYRET, C., CARLEER, M., CLERBAUX, C., COHEUR, P.F., COLIN, R., DECOLA, P., DEMAZIÈRE, M., DRUMMOND, J.R., DUFOUR, D., EVANS, W.F.J., FAST, H., FUSSEN, D., GILBERT, K., JENNINGS, D.E., LLEWELLYN, E.J., LOWE, R.P., MAHIEU, E., MCCONNELL, J.C., MCHUGH, M., MCLEOD, S.D., MICHAUD, R., MIDWINTER, C., NASSAR, R., NICHITIU, F., NOWLAN, C., RINSLAND, C.P., ROCHON, Y.J., ROWLANDS, N., SEMENIUK, K., SIMON, P., SKELTON, R., SLOAN, J.J., SOUCY, M.A., STRONG, K., TREMBLAY, P., TURNBULL, D., WALKER, K.A., WALKTY, I., WARDLE, D.A., WEHRLE, V., ZANDER, R. & ZOU, J. (2005). Atmospheric chemistry experiment (ACE): mission overview. *Geophysical Research Letters*, **32**, L15S01.

BOGUMIL, K., ORPHAL, J., HOMANN, T., VOIGT, S., SPIETZ, P., FLEISCHMANN, O.C., VOGEL, A., HARTMANN, M., KROMMINGA, H., BOVENSMANN, H. *et al.* (2003). Measurements of molecular absorption spectra with the sciamachy pre-flight model: instrument characterization and reference data for atmospheric remote-sensing in the 230–2380 nm region. *J. Photochem. Photobiol. A: Chem*, **157**, 167–184.

BOONE, C., NASSAR, R., WALKER, K., ROCHON, Y., MCLEOD, S., RINSLAND, C. & BERNATH, P. (2005). Retrievals for the atmospheric chemistry experiment fourier-transform spectrometer. *Applied optics*, **44**, 7218–7231.

BORCHI, F. & POMMEREAU, J.P. (2007). Evaluation of ozonesondes, HALOE, SAGE II and III, Odin- OSIRIS and -SMR, and ENVISAT-GOMOS, -SCIAMACHY and -MIPAS ozone profiles in the tropics from SAOZ long duration balloon measurements in 2003 and 2004. *Atmospheric Chemistry and Physics*, **7**, 2671–2690.

Bovensmann, H., Burrows, J.P., Buchwitz, M., Frerick, J., Noël, S., Rozanov, V., Chance, K. & Goede, A. (1999). SCIAMACHY: Mission objectives and measurement modes. *Journal of the Atmospheric Sciences*, **56**, 127–150.

Bracher, A., Weber, M., Bramstedt, K., Tellmann, S. & Burrows, J.P. (2004). Long-term global measurements of ozone profiles by GOME validated with SAGE II considering atmospheric dynamics. *Journal of Geophysical Research*, **109**, D20308.

Bracher, A., Sinnhuber, M., Rozanov, A. & Burrows, J. (2005). Using a photochemical model for the validation of NO_2 satellite measurements at different solar zenith angles. *Atmospheric Chemistry and Physics*, **5**, 393–408.

Brenninkmeijer, C.A. (2012). Civil Aircraft for the Regular Investigation of the atmosphere Based on an Instrumented Container. `http://www.caribic-atmospheric.com`.

Brenninkmeijer, C.A.M., Crutzen, P., Boumard, F., Dauer, T., Dix, B., Ebinghaus, R., Filippi, D., Fischer, H., Franke, H., Friess, U., Heintzenberg, J., Helleis, F., Hermann, M., Kock, H.H., Koeppel, C., Lelieveld, J., Leuenberger, M., Martinsson, B.G., Miemczyk, S., Moret, H.P., Nguyen, H.N., Nyfeler, P., Oram, D., O'Sullivan, D., Penkett, S., Platt, U., Pupek, M., Ramonet, M., Randa, B., Reichelt, M., Rhee, T.S., Rohwer, J., Rosenfeld, K., Scharffe, D., Schlager, H., Schumann, U., Slemr, F., Sprung, D., Stock, P., Thaler, R., Valentino, F., van Velthoven, P., Waibel, A., Wandel, A., Waschitschek, K., Wiedensohler, A., Xueref-Remy, I., Zahn, A., Zech, U. & Ziereis, H. (2007). Civil aircraft for the regular investigation of the atmosphere based on an instrumented container: The new CARIBIC system. *Atmospheric Chemistry and Physics*, **7**, 4953–4976.

Brohede, S., Haley, C., McLinden, C., Sioris, C., Murtagh, D., Petelina, S.V., Llewellyn, E.J., Bazureau, A., Goutail, F., Randall, C., Lumpe, J.D., Taha, G., Thomasson, L.W. & Gordley, L.L. (2007a). Validation of Odin/OSIRIS stratospheric NO_2 profiles. *Journal of Geophysical Research*, **112**, D07310.

Brohede, S., McLinden, C., Berthet, G., Haley, C., Murtagh, D. & Sioris, C. (2007b). A stratospheric NO_2 climatology from Odin/OSIRIS limb-scatter measurements. *Canadian Journal of Physics*, **85**, 1253–1274.

Burrows, J.P., Hötzle, E., Goede, A., Visser, H. & Fricke, W. (1995). SCIAMACHY - scanning imaging absorption spectrometer for atmospheric chartography. *Acta Astronautica*, **35**, 445–451.

Butz, A., Bösch, H., Camy-Peyret, C., Chipperfield, M., Dorf, M., Dufour, G., Grunow, K., Jeseck, P., Kühl, S., Payan, S., Pepin, I., Pukite, J., Rozanov, A., von Savigny, C., Sioris, C., Wagner, T., Weidner, F. & Pfeilsticker, K. (2006). Inter-comparison of stratospheric O_3 and NO_2 abundances retrieved from balloon borne direct sun observations and Envisat/SCIAMACHY limb measurements. *Atmospheric Chemistry and Physics*, **6**, 1293–1314.

CAMY-PEYRET, C. (1995). Balloon-borne infrared fourier transform spectroscopy for measurements of atmospheric trace species. *Spectrochimica Acta Part A: Molecular Spectroscopy*, **51**, 1143–1152.

CHAHINE, M. (1970). Inverse problems in radiative transfer: Determination of atmospheric parameters. *Journal of the Atmospheric Sciences*, **27**, 960–967.

CHIPPERFIELD, M.P. (2006). New version of the TOMCAT/SLIMCAT off-line chemical transport model: Intercomparison of stratospheric tracer experiments. *Quarterly Journal of the Royal Meteorological Society*, **132**, 1179–1203.

CHU, W.P., MCCORMICK, M.P., LENOBLE, J., BROGNIEZ, C. & PRUVOST, P. (1989). SAGE II inversion algorithm. *Journal of Geophysical Research*, **94**, 8339–8351.

CRUTZEN, P. (1970). The influence of nitrogen oxides on the atmospheric ozone content. *Quarterly Journal of the Royal Meteorological Society*, **96**, 320–325.

CRUTZEN, P., MOSIER, A., SMITH, K. & WINIWARTER, W. (2007). N_2O release from agrobiofuel production negates global warming reduction by replacing fossil fuels. *Atmospheric Chemistry and Physics Discussions*, **7**, 11191–11205.

CRUTZEN, P.J. (1979). The role of NO and NO_2 in the chemistry of the troposphere and stratosphere. *Annual Review of Earth and Planetary Sciences*, **7**, 443–472.

CUNNOLD, D.M., ZAWODNY, J.M., CHU, W.P., POMMEREAU, J.P., GOUTAIL, F., LENOBLE, J., MCCORMICK, M.P., VEIGA, R.E., MURCRAY, D., IWAGAMI, N. *et al.* (1991). Validation of SAGE II NO_2 measurements. *Journal of Geophysical Research*, **96**, 12913–12925.

DOICU, A., HILGERS, S., VON BARGEN, A., ROZANOV, A., EICHMANN, K.U., VON SAVIGNY, C. & BURROWS, J.P. (2007). Information operator approach and iterative regularization methods for atmospheric remote sensing. *Journal of Quantitative Spectroscopy & Readiative Transfer*, **103**, 340–350.

EICHMANN, K.U., VON SAVIGNY, C., REICHL, P., ROBERT, C., STEINWAGNER, J., BOVENSMANN, H. & BURROWS, J.P. (2009). SCODA: SCIAMACHY cloud detection algorithm from limb radiance measurements - ALGORITHM THEORETICAL BASIS DOCUMENT. Tech. rep., Institute of Environmental Physics, University of Bremen, unpublished technical document.

ENGEL, A., BÖNISCH, H., BRUNNER, D., FISCHER, H., FRANKE, H., GÜNTHER, G., GURK, C., HEGGLIN, M., HOOR, P., KÖNIGSTEDT, R., KREBSBACH, M., MASER, R., PARCHATKA, U., PETER, T., SCHELL, D., SCHILLER, C., SCHMIDT, U., SPELTEN, N., SZABO, T., WEERS,

U., WERNLI, H., WETTER, T. & WIRTH, V. (2006). Highly resolved observations of trace gases in the lowermost stratosphere and upper troposphere from the Spurt project: an overview. *Atmospheric Chemistry and Physics*, **6**, 283–301.

FAHEY, D. & HEGGLIN, M. (2011). Twenty questions and answers about the ozone layer: 2010 update. In *Scientific Assessment of Ozone Depletion: 2010, Global Ozone Research and Monitoring Project-Report No. 52*, 516pp., World Meteorological Organization, Geneva, Switzerland.

FARMAN, J.C., GARDINER, B.G. & SHANKLIN, J.D. (1985). Large losses of total ozone in antartica reveal seasonal ClO_x/NO_x interaction. *nature*, 207 – 210.

FERLEMANN, F., CAMY-PEYRET, C., FITZENBERGER, R., HARDER, H., HAWAT, T., OSTERKAMP, H., SCHNEIDER, M., PERNER, D., PLATT, U., VRADELIS, P. & PFEILSTICKER, K. (1998). Stratospheric BrO profiles measured at different latitudes and seasons: Instrument description, spectral analysis and profile retrieval. *Geophysical Research Letters*, **25**, 3847–3850.

FROMM, M., BEVILACQUA, R., SERVRANCKX, R., ROSEN, J., THAYER, J., HERMAN, J. & LARKO, D. (2005). Pyro-cumulonimbus injection of smoke to the stratosphere: Observations and impact of a super blowup in northwestern canada on 3-4 august 1998. *J. Geophys. Res*, **110**, 1–16.

GAUSS, M., ISAKSEN, I.S.A., LEE, D.S. & SØADE, O.A. (2006). Impact of aircraft NO_2 emissions on the atmosphere - tradeoffs to reduce the impact. *Atmospheric Chemistry and Physics*, **6**, 1529–1548.

GORDLEY, L.L., MARSHALL, B.T. & ALLEN CHU, D. (1994). LINEPAK: Algorithms for modeling spectral transmittance and radiance. *Journal of Quantitative Spectroscopy and Radiative Transfer*, **52**, 563–580.

GORDLEY, L.L., RUSSELL III, J.M., MICKLEY, L.J., FREDERICK, J.E., PARK, J.H., STONE, K.A., BEAVER, G.M., MCINEMEY, J.M., DEAVER, L.E., TOON, G.C. *et al.* (1996). Validation of nitric oxide and nitrogen dioxide measurements made by the Halogen Occultation Experiment for UARS platform. *Journal of Geophysical Research-Atmospheres*, **101**, 10241–10266.

GOTTWALD, M., BOVENSMANN, H., LICHTENBERG, G., NOËL, S., VON BARGEN, A., SLIJKHUIS, S., PITERS, A., HOOGEVEEN, R., VON SAVIGNY, C., BUCHWITZ, M., KOKHANOVSKY, A., RICHTER, A., ROZANOV, A.T., HOLZER-POPP, BRAMSTEDT, K., LAMBERT, J.C., SKUPIN, J., WITTROCK, F., SCHRIJVER, H. & BURROWS, J. (2006). *SCIAMACHY, Monitoring the Changing Earth's Atmosphere*. DLR, Institut für Methodik der Fernerkundung (IMF).

HALEY, C.S., BROHEDE, S.M., SIORIS, C.E., GRIFFIOEN, E., MURTAGH, D.P., MCDADE, I.C., ERIKSSON, P., LLEWELLYN, E.J., BAZUREAU, A. & GOUTAIL, F. (2004). Retrieval of stratospheric O_3 and NO_2 profiles from Odin Optical Spectrograph and Infrared Imager System (OSIRIS) limb-scattered sunlight measurements. *Journal of Geophysical Research*, **109**, D16303.

HOINKA, K. (1998). Statistics of the global tropopause pressure. *Monthly weather review*, **126**, 3303–3325.

HOOGEN, R., ROZANOV, V.V. & BURROWS, J.P. (1999). Ozone profiles from GOME satellite data: Algorithm description and first validation. *Journal of Geophysical Research*, **104**, 8263–8280.

HOUGHTON, J. (2002). *The Physics of Atmospheres*. Cambridge University Press, 3rd edn.

HOUGHTON, J.T., DING, Y., GRIGGS, D.J., NOGUER, M., VAN DER LINDEN, P.J., DAI, X., MASKELL, K. & JOHNSON, C. (2001). *Climate change 2001: the scientific basis*. Cambridge University Press Cambridge.

JÖCKEL, P. (2012). The highly structured modular earth submodel system (MESSy). `http://www.messy-interface.org/`.

JÖCKEL, P., TOST, H., POZZER, A., BRÜHL, C., BUCHHOLZ, J., GANZEVELD, L., HOOR, P., KERKWEG, A., LAWRENCE, M.G., SANDER, R., STEIL, B., STILLER, G., TANARHTE, M., TARABORRELLI, D., VAN AARDENNE, J. & LELIEVELD, J. (2006). The atmospheric chemistry general circulation model ECHAM5/MESSy1: consistent simulation of ozone from the surface to the mesosphere. *Atmospheric Chemistry and Physics*, **6**, 5067–5104.

KERZENMACHER, T., WOLFF, M.A., STRONG, K., DUPUY, E., WALKER, K.A., AMEKUDZI, L.K., BATCHELOR, R.L., BERNATH, P.F., BERTHET, G., BLUMENSTOCK, T. *et al.* (2008). Validation of NO_2 and NO from the Atmospheric Chemistry Experiment (ACE). *Atmospheric Chemistry and Physics*, **8**, 5801.

KINNERSLEY, J.S. (1996). The climatology of the stratospheric 'THIN AIR' model. *Quarterly Journal of the Royal Meteorological Society*, **122**, 219–252.

KNEIZYS, F.X., SHETTLE, E.P., ABREU, L.W., CHETWYND, J.H. & ANDERSON, G.P. (2002). Users Guide to LOWTRAN 7. Tech. rep., Defense Technical Information Center OAI-PMH Repository [http://stinet.dtic.mil/oai/oai] (United States).

KOZLOV, V. (1983). Design of experiments related to the inverse of mathematical physics. In C.M. Ermakov, ed., *Mathematical Theory of Experiment Design*, 216–246, Nauka, Moscow, (in Russian).

KÜHL, S., PUĶĪTE, J., DEUTSCHMANN, T., PLATT, U. & WAGNER, T. (2008). SCIAMACHY limb measurements of NO_2, BrO and OClO. retrieval of vertical profiles: Algorithm, first results, sensitivity and comparison studies. *Advances in Space Reearch*, **42**, 1747–1764.

LLEWELLYN, E.J., LLOYD, N.D., DEGENSTEIN, D.A., GATTINGER, R.L., PETELINA, S.V., BOURASSA, A.E., WIENSZ, J.T., IVANOV, E.V., MCDADE, I.C., SOLHEIM, B.H. *et al.* (2004). The OSIRIS instrument on the Odin spacecraft. *Canadian Journal of Physics*, **82**, 411–422.

MANAHAN, S.E. (1991). *Environmental Chemistry*. Lewis Publishers, 5th edn.

MCLINDEN, C., OLSEN, S.C., HANNEGAN, B., WILD, O., PRATHER, M.J. & SUNDET, J. (2000). Stratospheric ozone in 3-d models: A simple chemistry and the cross-tropopause flux. *Journal of Geophysical Research*, **105**, 14653–14665.

MCLINDEN, C., HALEY, C. & SIORIS, C. (2006). Diurnal effects in limb scatter observations. *Journal of Geophysical Research*, **111**, D14302.

MENKE, W. (1999). *Geophysical Data Analysis: Discrete Inversion Theory*. Academic Press.

MIE, G. (1908). Beiträge zur Optik trüber Medien, speziell kolloidaler Metallösungen. *Annalen der Physik*, **330**, 377–445.

MONTZKA, S.A., REIMANN (COORDINATINH LEAD AUTHORS), S., ENGEL, A., KRÜGER, K., O'DOHERTY, S., STURGES, W.T., BLAKE, D., DORF, M., FRASER, P., FROIDEVAUX, L., JUCKS, K., KREHER, K., KURYLO, M.J., MELLOUSKI, A., MILLER, J., NIELSEN, O.J., ORKIN, V.L., PRINN, R.G., RHEW, R., SANTEE, M.L., STOHL, A. & VERDONIK, D. (2011). Ozone-depleting substances (odss) and related chemicals. In *Scientific Assessment of Ozone Depletion: 2010, Global Ozone Research and Monitoring Project-Report No. 52*, chap. 1, 79 – 80, World Meteorological Organization, Geneva, Switzerland.

MYHRE, G., HIGHWOOD, E.J., SHINE, K.P. & STORDAL, F. (1998). New estimates of radiative forcing due to well mixed greenhouse gases. *Geophysical Research Letters*, **25**, 2715–2718.

NOXON, J.F. (1975). Nitrogen dioxide in the stratosphere and troposphere measured by ground-based absorption spectroscopy. *Science*, **189**, 547.

NOXON, J.F. (1979). Stratospheric NO_2 2: Global behavior. *Journal of Geophysical Research*, **84**, 5067–5076.

PENNER, J. (1999). *Aviation and the global atmosphere*. Cambridge Univ Press.

PLATT, U. (1994). Differential optical absorption spectroscopy (DOAS). In M. Sigrist, ed., *Air Monitoring by Spectroscopic Techniques*, 27–84, John Wiley, Hoboken, N.J.

PORTMANN, R.W., BROWN, S.S., GIERCZAK, T., TALUKDAR, R.K., BURKHOLDER, J.B. & RAVISHANKARA, A.R. (1999). Role of nitrogen oxides in the stratosphere: A reevaluation based on laboratory studies. *Geophysical Research Letters*, **26**, 2387–2390.

PRATHER, M. (1992). Catastrophic loss of stratospheric ozone in dense volcanic clouds. *Journal of Geophysical Research*, **97**, 10187.

PUĶĪTE, J., KÜHL, S., DEUTSCHMANN, W., T. WILMS-GRABE, FRIEDEBURG, C., PLATT, U. & WAGNER, T. (2006). Retrieval of stratospheric trace gases from SCIAMACHY limb measurements. In *Proceedings of the First Atmospheric Science Conference*, ESA/ESRIN, Frascati, Italy.

PUĶĪTE, J., KÜHL, S., DEUTSCHMANN, T., PLATT, U. & WAGNER, T. (2008). Accounting for the effect of horizontal gradients in limb measurements of scattered sunlight. *Atmospheric Chemistry and Physics*, **8**, 3045–3060.

RANDALL, C.E., LUMPE, J.D., BEVILACQUA, R.M., HOPPEL, K.W., SHETTLE, E.P., RUSCH, D.W., GORDLEY, L.L., KREHER, K., PFEILSTICKER, K., BOESCH, H., TOON, G., GOUTAIL, F. & POMMEREAU, J.P. (2002). Validation of POAM III NO_2 measurements. *Journal of Geophysical Research*, **107**, 4432.

RAVISHANKARA, A.R., DANIEL, J.S. & PORTMANN, R.W. (2009). Nitrous oxide (N_2O): The dominant ozone-depleting substance emitted in the 21st century. *Science*, **326**, 123.

REIS, S., PINDER, R.W., ZHANG, M., LIJIE, G. & SUTTON, M.A. (2009). Reactive nitrogen in atmospheric emission inventories. *Atmospheric Chemistry and Physics*, **9**, 7657–7677.

RICHTER, A., BURROWS, J.P., NÜSS, H., GRANIER, C. & NIEMEIER, U. (2005). Increase in tropospheric nitrogen dioxide over china observed from space. *nature*, **437**, 129–132.

RODGERS, C.D. (2000). *Inverse Methods for Atmospheric Sounding*, vol. 2 of *Series on Atmospheric, Oceanic and Planetary Physics*. World Scientific.

ROECKNER, E., BÄUML, G., BONAVENTURA, L., BROKOPF, R., ESCH, M., GIORGETTA, M., HAGEMANN, S., KIRCHNER, I., KORNBLUEH, L., MANZINI, E., RHODIN, A., SCHLESE, U., SCHULZWEIDA, U. & TOMPKINS, A. (2003). The atmospheric general circulation model ECHAM5. PART I: Model description. Tech. rep., Max Planck Institute for Meteorology.

ROECKNER, E., BROKOPF, R., ESCH, M., GIORGETTA, M., HAGEMANN, S., KORNBLUEH, L., MANZINI, E., SCHLESE, U. & SCHULZWEIDA, U. (2004). The atmospheric general circulation model ECHAM5. PART II: Sensitivity of simulated climate to horizontal and vertical resolution. Tech. rep., Max Planck Institute for Meteorology.

ROTHMAN, L., JACQUEMART, D., BARBE, A., CHRIS BENNER, D., BIRK, M., BROWN, L., CARLEER, M.R., CHACKERIAN, C. *et al.* (2005). The HITRAN 2004 molecular spectroscopic database. *Journal of Quantitative Spectroscopy and Radiative Transfer*, **96**, 139–204.

ROZANOV, A. (2001). *Modeling of radiative transfer through a spherical planetary atmosphere*. Ph.D. thesis, University of Bremen.

ROZANOV, A. (2007). *User's Guide for the Software Package SCIATRAN Version 2.2*. Institute of Remote Sensing University of Bremen, Germany.

ROZANOV, A. (2012). SCIATRAN - RADIATIVE TRANSFER MODEL AND RETRIEVAL ALGORITHM. `http://www.iup.uni-bremen.de/sciatran/`.

ROZANOV, A., BOVENSMANN, H., BRACHER, A., HRECHANYY, S., ROZANOV, V., SINNHUBER, M., STROH, F. & BURROWS, J. (2005). NO_2 and BrO vertical profile retrieval from

SCIAMACHY limb measurements: Sensitivity studies. *Advances in Space Research*, **36**, 846–854.

Rozanov, A., Kühl, S., Doicu, A., McLinden, C., Pukīte, J., Bovensmann, H., Burrows, J.P., Deutschmann, T., Dorf, M., Goutail, F., Grunow, K., Hendrick, F., von Hobe, M., Hrechanyy, S., Lichtenberg, G., Pfeilsticker, K., Pommereau, J.P., Van Roozendael, M., Stroh, F. & Wagner, T. (2011). BrO vertical distributions from SCIAMACHY limb measurements: comparison of algorithms and retrieval results. *Atmospheric Measurement Techniques*, **4**, 1319–1359.

Russel III, J.M. & Remsberg, E.E. (2012). The HALogen Occultation Experiment (HALOE). `http://haloe.gats-inc.com`.

Russell III, J.M., Gordley, L.L., Park, J.H., Drayson, S.R., Hesketh, W.D., Cicerone, R.J., Tuck, A.F., Frederick, J.E., Harries, J.E. & Crutzen, P.J. (1993). The halogen occultation experiment. *Journal of Geophysical Research-Atmospheres*, **98**, 10777–10797.

Sioris, C.E., Haley, C.S., McLinden, C.A., von Savigny, C., McDade, I.C., McConnell, J.C., Evans, W.F.J., Lloyd, N.D., Llewellyn, E.J., Chance, K.V., Kurosu, T.P., Murtagh, D., Frisk, U., Pfeilsticker, K., Bosch, H., Weidner, F., Strong, K., Stegman, J. & Megie, G. (2003). Stratospheric profiles of nitrogen dioxide observed by Optical Spectrograph and Infrared Imager System on the Odin satellite. *Journal of Geophysical Research*, **108**, 4215.

Sioris, C.E., McLinden, C.A., Martin, R.V., Sauvage, B., Haley, C.S., Lloyd, N.D., Llewellyn, E.J., Bernath, P.F., Boone, C.D., Brohede, S. & McElroy, C.T. (2007). Vertical profiles of lightning-produced NO_2 enhancements in the upper troposphere observed by OSIRIS. *Atmospheric Chemistry and Physics*, **7**, 4281–4294.

Solomon, S. (1999). Stratospheric ozone depletion: A review of concepts and history. *Rev. Geophys*, **37**, 275–316.

Sonkaew, T. (2010). *Quantification of the chemical ozone loss in the northern and southern polar vortices using SCIAMACHY limb measurements*. Ph.D. thesis, University of Bremen.

Sonkaew, T., Rozanov, V.V., von Savigny, C., Rozanov, A., Bovensmann, H. & Burrows, J.P. (2009). Cloud sensitivity studies for stratospheric and lower mesospheric ozone profile retrievals from measurements of limb-scattered solar radiation. *Atmospheric Measurement Techniques*, **2**, 653–678.

Stohl, A., Huntrieser, H., Richter, A., Beirle, S., Cooper, O.R., Eckhardt, S., Forster, C., James, P., Spichtinger, N., Wenig, M., Wagner, T., Burrows, J.P. & Platt, U. (2003). Rapid intercontinental air pollution transport associated with a meteorological bomb. *Atmospheric Chemistry and Physics*, **3**, 969–985.

SØVDE, O.A., GAUSS, M., ISAKSEN, I.S.A., PITARI, G. & MARIZY, C. (2007). Aircraft pollution - a futuristic view. *Atmospheric Chemistry and Physics*, **7**, 3621–3632.

VON SAVIGNY, C., ULASI, E.P., EICHMANN, K.U., BOVENSMANN, H. & BURROWS, J.P. (2005). Detection and mapping of polar stratospheric clouds using limb scattering observations. *Atmospheric Chemistry and Physics*, **5**, 3071–3079.

VON SAVIGNY, C., ROZANOV, A., BOVENSMANN, H., NOEL, S., GOTTWALD, M., SLIJKHUIS, S. & BURROWS, J. (2007). Studying Envisat attitude with SCIAMACHY limb-scatter measurements. In *Proceedings of the Envisat Symposium*.

VON SAVIGNY, C., BOVENSMANN, H., BRAMSTEDT, K., DIKTY, S., EBOJIE, F., JONES, A., NOËL, S., ROZANOV, A. & SINNHUBER, B.M. (2009). Indications for long-term trends and seasonal variations in the SCIAMACHY level 1 version 6.03 tangent height information. Tech. rep., Institute of Environmental Physics, University of Bremen, technical note TN-IUP-scia-pointing-2009-01 Issue 2.

WAGNER, T., BURROWS, J.P., DEUTSCHMANN, T., DIX, B., VON FRIEDEBURG, C., FRIESS, U., HENDRICK, F., HEUE, K., IRIE, H., IWABUCHI, H. *et al.* (2007). Comparison of box-air-mass-factors and radiances for multiple-axis differential optical absorption spectroscopy (MAX-DOAS) geometries calculated from different UV/visible radiative transfer models. *Atmospheric Chemistry and Physics*, **7**, 1809–1833.

WALKER, K.A., RANDALL, C.E., TREPTE, C.R., BOONE, C.D. & BERNATH, P.F. (2005). Initial validation comparisons for the Atmospheric Chemistry Experiment (ACE-FTS). *Geophysical Research Letters*, **32**, L16S04.

WENIG, M., KÜHL, S., BEIRLE, S., BUCSELA, E., JÄHNE, B., PLATT, U., GLEASON, J. & WAGNER, T. (2004). Retrieval and analysis of stratospheric NO_2 from the global ozone monitoring experiment. *Journal of geophysical research*, **109**, D04315.

WENNBERG, P.O., COHEN, R.C., STIMPFLE, R.M., KOPLOW, J.P., ANDERSON, J.G., SALAWITCH, R.J., FAHEY, D.W., WOODBRIDGE, E.L., KEIM, E.R., GAO, R.S. *et al.* (1994). Removal of stratospheric O_3 by radicals: In situ measurements of OH, HO_2, NO, NO_2, ClO, and BrO. *Science*, **266**, 398.

WETZEL, G., BRACHER, A., FUNKE, B., GOUTAIL, F., HENDRICK, F., LAMBERT, J.C., MIKUTEIT, S., PICCOLO, C., PIRRE, M., BAZUREAU, A., BELOTTI, C., BLUMENSTOCK, T., DE MAZIÈRE, M., FISCHER, H., HURET, N., IONOV, D., LÓPEZ-PUERTAS, M., MAUCHER, G., OELHAF, H., POMMEREAU, J.P., RUHNKE, R., SINNHUBER, M., STILLER, G., VAN ROOZENDAEL, M. & ZHANG, G. (2007). Validation of MIPAS-ENVISAT NO_2 operational data. *Atmospheric Chemistry and Physics*, **7**, 3261–3284.

WIETERS, N., WINKLER, H., SINNHUBER, B.M. & NOTHOLT, J. (2009). Modeled impact of atmospheric ionisation by solar protons and magnetospheric electrons on upper stratospheric constituents compared with mipas measurements. 2nd International High Energy Particle Precipitation in the Atmosphere (HEPPA) Workshop.

WMO (WORLD METEOROLOGICAL ORGANIZATION) (2011). Scientific Assessment of Ozone Depletion: 2010, Global Ozone Research and Monitoring Project-Report No. 52.

Acknowledgements

I would like to thank the following people and institutions for their help and contributions throughout this project.

First of all, I would like to thank Professor John P. Burrows for giving me the opportunity to work in his work group at the IUP (Institute of Environmental Physics in Bremen) on this interesting and challenging subject. Without his continuous support and effort, this work would not have been possible.

I would also like to thank my supervisor Alexei Rozanov, for his expertise and support. His and Vladimir Rozanov's work on SCIATRAN serves as a great foundation to do fascinating research. He was always ready to discuss new developments and proofed to be an experienced guide in the fascinating world of satellite retrievals.

Furthermore, I would like to thank my project leader, Heinrich Bovensmann, for his constant support and motivation.

Additional thanks go to Miriam and Björn-Martin Sinnhuber, who were always helpful in the field of photochemical corrections and chemistry models.

Special thanks go to Chris A. McLinden, working at Environmental Canada, who has provided very helpful model results and also provided data to elaborate on the diurnal effect error.

I'm grateful to Kaley A. Walker, and everybody else who is involved, for the possibility to work with data from the Atmospheric Chemistry Experiment (ACE), also known as SCISAT, a Canadian-led mission mainly supported by the Canadian Space Agency and the Natural Sciences and Engineering Research Council of Canada. My gratitude also goes to James

Russell III, Larry L. Gordley, and the HALOE science and data processing teams for providing the profiles used in this study. I also wish to thank Joseph M. Zawodny, the NASA Langley Research Center (NASA-LaRC) and the NASA Langley Radiation and Aerosols Branch for making it possible for us to work with SAGE II data sets.

For help on validation efforts, I would like to thank Thiranan Sonkaew, who provided a method to calculate potential vorticities, and to Felix Ebojie, from whom I received tropopause height information.

I would also like to thank the SPURT and CARIBIC work groups for highly interesting airplane based measurement results, especially Carl Brenninkmeijer for CARIBIC and Peter Hoor, who provided me with data for Spurt. I am also grateful to the latter for extremely interesting model results, especially of the North Atlantic region.

Additional thanks go to Annette Ladstätter-Weißenmayer, for her help with the text and her motivation.

Furthermore, I am very grateful to Kai-Uwe Eichmann, who provided extremely useful cloud height information and was always a helpful and great colleague.

I am thankful to ECMWF for providing pressure and temperature information (ECMWF Special Project SPDECDIO) for this study. Some data shown here were calculated on German HLRN (High-Performance Computer Center North). This work is partly funded by the EU-project QUANTIFY, FP6.

Almost finally, I was very happy to work with all the interesting people at the IUP institute. However, my special thanks go to Oliver Schneising, Max Reuter, Sebastian Mieruch, Sebastian Dikty, Thomas Frings, Florian Ernst, Anja Schönhardt and everybody on the 4th floor of our building.

Ich danke nicht zuletzt meinen Eltern, dass sie mir mein Studium ermöglicht haben und immer für mich da waren und sind.

Corrections

Page 1

line 9: ~~NO and NO_2~~
line 15: ~~Many~~
line 18: UV ⟶ UV-B

Page 2

line 30: measurements ⟶ profiles

Page 4

described ⟶ explained (line 6), introduced (line 9), presented (line 11)

Erklärung

Hiermit erkläre ich, dass ich die Arbeit ohne unerlaubte fremde Hilfe angefertigt habe, dass ich weiterhin keine anderen als die angegebenen Quellen und Hilfsmittel benutzt und die den benutzten Werken wörtlich oder inhaltlich entnommenen Stellen als solche kenntlich gemacht habe.

Bremen, der 13. März 2012

Ralf Bauer